

Multimedia Contents



# Flying Robot

## 26. Flying Robots

Stefan Leutenegger, Christoph Hürzeler, Amanda K. Stowers, Kostas Alexis, Markus W. Achtelik, David Lentink, Paul Y. Oh, Roland Siegwart

Part B | 26

Unmanned aircraft systems (UASs) have drawn increasing attention recently, owing to advancements in related research, technology, and applications. While having been deployed successfully in military scenarios for decades, civil use cases have lately been tackled by the robotics research community.

This chapter overviews the core elements of this highly interdisciplinary field; the reader is guided through the design process of aerial robots for various applications starting with a qualitative characterization of different types of UAS. Design and modeling are closely related, forming a typically iterative process of drafting and analyzing the related properties. Therefore, we overview aerodynamics and dynamics, as well as their application to fixed-wing, rotary-wing, and flapping-wing UAS, including related analytical tools and practical guidelines. Respecting use-case-specific requirements and core autonomous robot demands, we finally provide guidelines to related system integration challenges.

26.1	<b>Background and History</b> .....	624
26.1.1	A Glimpse of History .....	624
26.2	<b>Characteristics of Aerial Robotics</b> .....	625
26.2.1	Aerial Robots Classification .....	625
26.2.2	The Effect of Scale .....	626
26.3	<b>Basics of Aerodynamics and Flight Mechanics</b> .....	629
26.3.1	Properties of the Atmosphere .....	630
26.3.2	General Fluid Dynamics and 2-D Flow around Airfoils .....	630
26.3.3	Wing Aerodynamics .....	633
26.3.4	Performance of Rotors and Propellers .....	635
26.3.5	Drag .....	637
26.3.6	Aircraft Dynamics and Flight Performance Analysis .....	638
26.4	<b>Airplane Modeling and Design</b> .....	641
26.4.1	Forces and Moments .....	641
26.4.2	Static Stability .....	642
26.4.3	Dynamic Model .....	643
26.4.4	Design Guidelines .....	644
26.4.5	A Simple Autopilot.....	646
26.5	<b>Rotorcraft Modeling and Design</b> .....	647
26.5.1	Mechanical Design of Rotors and Propellers .....	648
26.5.2	Rotorcraft Dynamics.....	648
26.5.3	Simplified Aerodynamics.....	649
26.5.4	Nonuniform Inflow.....	651
26.5.5	Flapping Dynamics .....	651
26.5.6	Flight Dynamics Assessment .....	652
26.6	<b>Flapping Wing Modeling and Design</b> ....	653
26.6.1	Aerodynamic Mechanisms .....	653
26.6.2	Sizing New Flappers.....	655
26.7	<b>System Integration and Realization</b> .....	659
26.7.1	Challenges for Autonomous UAS .....	659
26.7.2	Levels of Autonomy .....	659
26.7.3	UAS Components .....	660
26.8	<b>Applications of Aerial Robots</b> .....	662
26.8.1	Demonstrated Applications of UAS .....	662
26.8.2	Current Applications and Missions .....	664
26.8.3	Aerial Robots: Emerging Categories .....	664
26.8.4	Open Issues .....	665
26.9	<b>Conclusions and Further Reading</b> .....	666
	<b>Video-References</b> .....	666
	<b>References</b> .....	667

## 26.1 Background and History

The field of *aerial robotics* encompasses a very broad class of flying machines that nowadays often possess the perception capabilities and decisional autonomy to accomplish complex tasks without the need for any direct human intervention. Historically and within the aerospace jargon, robotic flying machines are commonly referred to as *unmanned aerial vehicles* (UAVs), while the entire infrastructures, systems and human-machine interfaces required for autonomous operation are often called *unmanned aerial systems* (UAS). Aerial robotic technologies are currently on the cutting edge of aerospace and robotic research. Breakthrough contributions take place in various fields such as design, estimation [26.1], perception [26.2], control [26.3], and planning [26.4], paving the way for a historical change on how flying systems are operated and what application challenges they fulfill.

As a class of systems, aerial robots have their roots in the first guided missiles; however, nowadays they refer to a wide variety of advanced intelligent systems. According to the American Institute of Aeronautics and Astronautics (AIAA) [26.5], a UAV is defined as

*an aircraft which is designed or modified, not to carry a human pilot and is operated through electronic input initiated by the flight controller or by an onboard autonomous flight management control system that does not require flight controller intervention.*

As is generally the case in robotics, aerial robots tend to become more and more complex systems as a result of the effort to achieve advanced decision making and planning capabilities based on its on-board perception of the environment and a set of relatively abstract mission goals.

Aerial robots possess the unique capability to gently fly over terrain that other robots struggle to roll or crawl over. The price to be paid is related with the advanced challenges in terms of system design, propulsion, perception, control, and navigation. Autonomous flight requires handling of all six degrees of freedom and advanced cognition capabilities within challenging environments. In that sense, perception and navigation complexity drastically increase, while payload and available power consumption for processing tends to be limited, especially as scale decreases. Essentially, the design of aerial robots requires increased attention and thorough selection, or even combination, of one or more existing or new flying concepts, electronic components and algorithms. The design engineer has to assess specific optimization challenges and trade-offs

as important desired goals like decreased weight and modularity typically contradict each other.

### 26.1.1 A Glimpse of History

Aerial robotics is a field of active research and promising perspectives, yet it already accumulates more than a century of developments. Figure 26.1 depicts some historical as well as recent examples of UAVs in the military and civilian sector. Starting as conceptual designs in the context of the human efforts to develop flying machines, aerial robots soon proved their extensive potential and have already created their own legacy. As was also the case for manned aviation, aerial robotic technologies accelerated within the framework of the 20th century world conflicts. Within World War I, Hewitt–Sperry developed an automatic plane that acted as a flying torpedo, carrying onboard intelligence to autonomously sustain flight over long periods of time. This page-turning success was achieved through the integration of (Sperry's self-made) gyroscopes which were then mechanically connected to the control surfaces and therefore established the necessary feedback control loop. During World War II, the German armed forces deployed one of the first successful cruise missiles, the V-1. Despite the fact that V-1 had limited success rate it did incorporate most of the elementary components, estimation algorithms and control loops that can allow autonomous navigation and reference tracking. Military applications kept being, and still are, the main driving force of aerial robotics research and the newest developments in the area change and shape the modern warfare. With the introduction of global positioning systems (GPSs), aerial robots managed to achieve the first completely autonomous surveillance missions. As information and intelligence gathering became one of the most important aspects of the world's open or silent conflicts, military research around the 1970s led to systems equipped with cameras and other sensory systems, giving birth to the UAV prototype the way we know it today. However, civil applications are currently emerging at a very fast pace and the majority of market predictions converge to the conclusion that this area will take dominant characteristics, and most importantly, will become an equally important – if not more – innovation drive.

Within this framework, the advancements in the field of microprocessors, miniaturized sensing, as well as actuator efficiency and downscaling greatly accelerated the field of aerial robots and paved the way for the great achievements we observe today. Aerial robots have advanced to a state in which sophisticated sensor



**Fig. 26.1** A glimpse on the UAS history through some examples starting from the Hewitt–Sperry Automatic Airplane (1917), the V-1 flying bomb (1944), and the Lockheed D-21 (1962) until the recent examples of military (Predator, Robocopter, nEuron) and civilian (AtlantikSolar, Firefly, Apid 60) aerial robots

modules for onboard state estimation and environmental perception, powerful embedded processors running sophisticated navigation algorithms, potentially several

communication interfaces, as well as high-end-mission-oriented payloads that enable the execution of challenging tasks, can be tightly integrated.

## 26.2 Characteristics of Aerial Robotics

This section aims to provide an overview of the key characteristic features and properties of different aerial robotic configurations as well as a classification based on the key advantages and limitations of some of the most common flying concepts found in unmanned aviation.

### 26.2.1 Aerial Robots Classification

Compared to the categorization of manned aviation, aerial robots classification is more complex, as the term currently refers to a very wide variety of systems of different scale, mechanical configuration, and actuation principles. In their vast majority, aerial robots correspond, in one way or another, to miniaturized versions of manned aircraft designs. Relatively classical fixed-wing unmanned aerial systems (FW-UAS) de-

signs and rotary-wing unmanned aerial systems (RW-UAS) such as those shown in Fig. 26.2 are common vehicle configurations one may encounter in most applications, including those of surveillance, monitoring, inspection, mapping, or payload transportation. However, even within these relatively traditional concepts, several design aspects differ from those chosen for manned systems. This reflects the fact that for different scales, the variation of the physical properties behavior, along with the search for optimized designs, will naturally lead to modified and novel design considerations. This is further triggered by the fact that the absence of a pilot on-board unlocks a wide set of engineering choices, typically out of question or even forbidden in manned aviation. As expected for a multitude of engineering reasons, large UAS tend to follow design concepts closer to – while at smaller scale to classi-

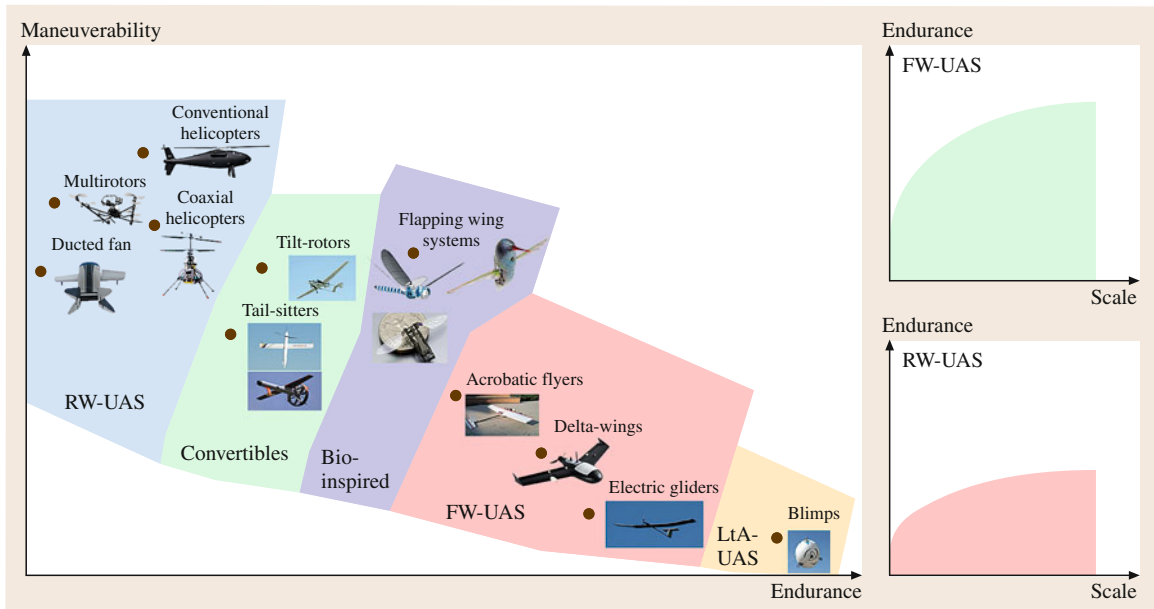


**Fig. 26.2** Classification of aerial robotics based on their endurance and maneuverability properties. Also note the significant effect of scale which highlights that comparisons should be done on similar scales

cal designs while as scale decreases innovation – at the level of the flying principle – becomes more and more intense.

Apart from *lighter-than-air* systems (LtA-UAS), FW-UAS tend to be the most power efficient flying principle, while RW-UAS are tailored to increased maneuverability as well as the ability of stationary vertical flight (*hovering*). This general classification (also valid for manned aviation) is then further complicated with the relatively large class of convertible designs (such as tilt-rotors or cruise-flight-enabled ducted fans). This first attempt for aerial robots classification has then to be further augmented to account for the biologically inspired concepts, and especially the emerging field of flapping-wing UAS (FI-UAS). Figure 26.2 provides an abstract – yet incomplete – overview of the vehicle classes one may encounter in most of the application fields. As shown, a large diversity is observed as a result of the engineering efforts to propose designs with optimized endurance, agility, controllability, or even simplicity in a very wide scale range. In the following subsections, a brief overview on how the main aerodynamic forces and effects depend on the design scale of an aerial vehicle are provided.

### 26.2.2 The Effect of Scale

The understanding of how aerial vehicles manage to remain airborne, provides a useful insight into the effect of scale, and how different dimensioning has

a huge impact on the efficiency of every flying machine. Table 26.1 provides an overview of the formulas expressing the lift force, as well as the drag forces that govern the flight of the most common UAS configurations. More detailed definitions on the aerodynamic forces can be found on the subsequent sections.

Within these equations,  $\rho$  is the density of the air while the remaining parameters are specific to the vehicle configuration. For FW-UAS,  $c_L$  and  $c_D$  represent the wing lift and drag coefficients, respectively,  $A$  is the wing area, and  $V_t$  denotes the airspeed. For the case of RW-UAS,  $c_T$  and  $c_Q$  denote the rotor thrust and drag coefficients,  $(\pi R^2)$  is the rotor disk area,  $\Omega$  is the angular velocity of the rotor, and  $R$  is the rotor disk radius. Finally, for LtA-UAS,  $V^{LtA}$  is the volume of the blimp,  $c_D^{LtA}$  is the drag coefficient depending on the blimp shape,  $V_t$  is the blimp's airspeed,  $A^{LtA}$  is the blimp surface in the direction of motion and  $\rho_{gas}$  is the filling gas density. Figure 26.3 illustrates

**Table 26.1** Formulas of the main aerodynamic forces and moments for common UAS configurations. FW stands for *fixed-wing* UAS, RW for *rotary-wing*, and LtA for *lighter-than-air*

UAS	Lift/Thrust	Drag force/Moment
FW	$L = \frac{1}{2} c_L \rho A V_t^2$	$D = \frac{1}{2} c_D \rho A V_t^2$
RW	$T = c_T \rho (\pi R^2) (R \Omega)^2$	$Q = c_Q \rho (\pi R^2) (R \Omega)^2 R$
LtA	$L_s = -g V^{LtA} (\rho_{gas} - \rho)$	$D = \frac{1}{2} c_D^{LtA} \rho A^{LtA} V_t^2$

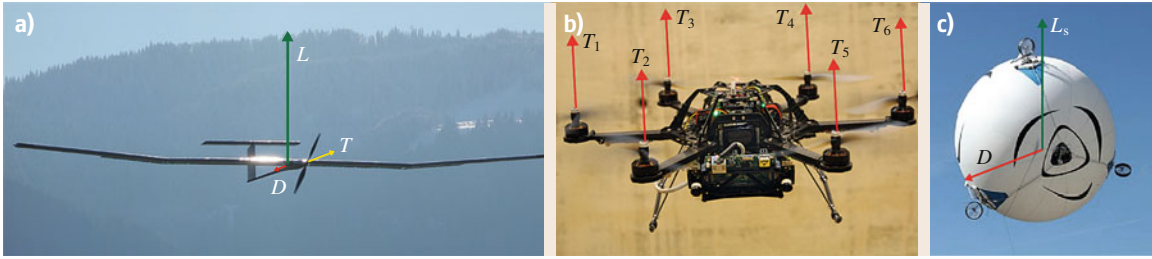


**Fig. 26.3a–c** Main aerodynamic forces applied on (a) fixed-wing, (b) rotary-wing, and (c) lighter-than-air systems. (a) AtlantikSolar is a solar-powered FW-UAS developed by the Autonomous Systems Lab at ETH Zurich, (b) Firefly is developed by Ascending Technologies GMBH, while (c) Skye is developed by students of ETH Zurich

these forces on the body of the relevant aerial vehicle configurations.

Derivation of *scaling laws* starts with the observation of the lift and drag forces and how these are functions of scale-dependent parameters such as the area of the wing or the rotor radius. Proper dimensioning is essentially a very complex procedure where a multitude of factors has to be taken into account. Among others, one has to account for the issues of aerodynamics efficiency, availability of propulsion systems at a given scale, the technologies they employ (e.g., electric motors, jet engines) as well as the simplicity and robustness of the corresponding mechanical configuration. In the following, scaling laws and relevant design guidelines for fixed-wing, rotary-wing, and lighter-than-air systems are provided. Only a brief overview is provided for the case of flapping-wing systems, as the effect of scale on such UAS configurations is separately discussed within Sect. 26.6.

#### FW-UAS

Scaling laws express the dominant role of size and scale for a given vehicle configuration. In the case of fixed-wing systems, the wing loading, defined as the ratio of the weight ( $W$ ) versus the wing area  $A$ , is the key parameter one has to focus to get some first insight on the role of scale. The Tennekes diagram shown in Fig. 26.4 provides a visual interpretation of this fact [26.6]. Working around the point that the lift force exactly counteracts the weight, the indicated trend line was derived using the following formulas [26.7]

$$\begin{aligned} \frac{W}{A} &= \sqrt[3]{W}47, \\ \frac{W}{A} &= \frac{1}{2}c_L\rho V_t^2, \\ A &= b_w c_w, \end{aligned} \quad (26.1)$$

where  $V_t$  is the airspeed,  $W$  is the weight,  $A$  is the wing area,  $b_w$  is the wing span, and  $c_w$  is the wing chord. These equations express the role of the lifting properties

of the airfoil and airspeed against the ratio of the weight of the flying body and its wing area. For this analysis, a fixed aspect ratio ( $\Lambda = b_w/c_w$ ) is assumed for all sizes of aircraft. Although such a simple analysis does not account for the details of the fluid dynamics environment between the different aircraft sizes, it is known that smaller aircrafts are typically built with lower aspect ratios, and that the difference in aspect ratio over existing aircraft within the size range of interest is significant.

#### RW-UAS

For the case of rotorcraft configurations, similar scaling laws regarding the vehicle efficiency may be derived. It is important to highlight however that especially for rotorcrafts, working with scaling laws demands that one has to simultaneously focus on both efficiency and dynamic response in order to avoid undesired effects in the vehicle flight dynamics such as unstable oscillations. Regarding the power efficiency, let power loading (PL) be defined as  $T/P$ , where  $P$  corresponds to the ideal power. As the induced ideal power to hover is given by  $P = T v_h$ , the *ideal power loading* will be inversely proportional to the induced velocity at the rotor disk  $v_i$

$$v_h = v_i \Rightarrow \sqrt{\frac{T}{2\rho(\pi R^2)}} = \frac{P}{T} = (PL)^{-1}. \quad (26.2)$$

Observing Fig. 26.5, it is shown that the ratio  $T/P$  decreases quickly with increasing disk loading. Therefore, configurations with proportionally smaller rotors against their mass will tend to be less efficient in hovering flight; that is, the rotor will require proportionally more power to generate the required amount of thrust. It is also to be noted, however, that calculation of the actual power loading and rotor efficiency requires the consideration of viscous losses.

From the above brief analysis, we concluded that in general the tendency to increase the rotor dimension favors efficiency. However, this is not the only scaling law one has to consider. Rotorcrafts are particularly com-



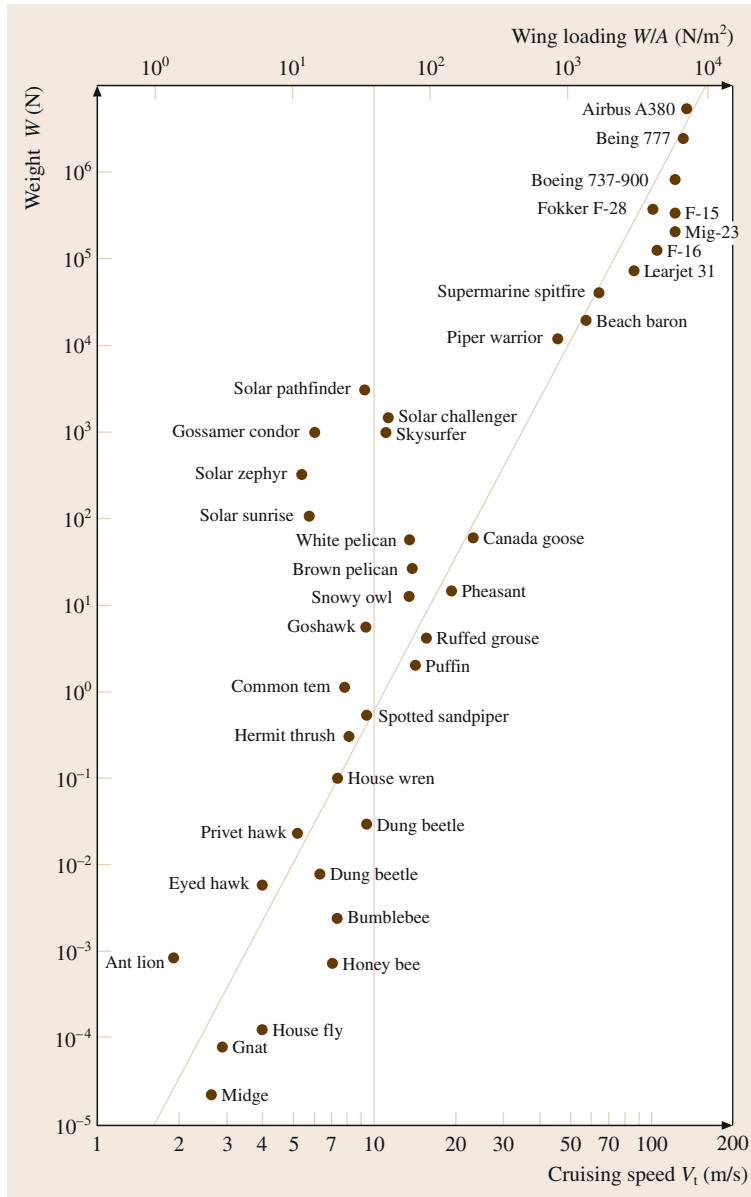


**Fig. 26.4** Tennekes size trend relating wing loading and cruise speed to weight for insects, birds, and manned aircraft

plex dynamic systems and scaling considerations also have to focus on dynamic aspects of their flight. A more concrete analysis may take place using Froude or Mach scaling models. Let  $N$  denote the length scale between two vehicles,  $R_m$  the rotor radius of the model vehicle, and  $R_p$  the rotor radius of the prototype vehicle: thus, a scale factor  $N$  denotes a helicopter  $1/N$  times the size of its prototype. Table 26.2 summarizes the Froude and Mach scaling laws that account for the role of scale in a set of significant parameters namely the length of the model and the prototype  $L_m$ ,  $L_p$ , the dominant time constants  $t_m$ ,  $t_p$  of the inner-loop characteristic response,

the characteristic velocities  $V_m$ ,  $V_p$ , the weight values  $W_m$ ,  $W_p$ , the expected moments of inertia  $I_m$ ,  $I_p$ , and the response-dominant frequencies  $\omega_m$ ,  $\omega_p$ .

These, slightly more advanced scaling laws, further provide the opportunity to assess the aspects of main rotor performance, and more specifically the expected thrust margin. Traditional manned helicopters have small thrust margins in hover, typically 5–10% while miniaturized vehicles often present very high values. Mach models predict in general faster rotor speeds as compared to Froude scaled models, which consequently leads to a lower expected thrust coefficient. The

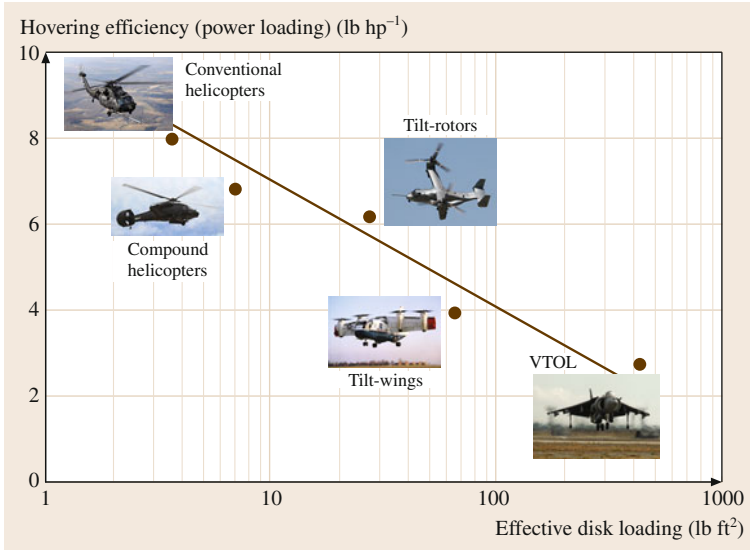


**Fig. 26.5** Hovering efficiency versus disk loading for a range of vertical lift aircraft

**Table 26.2** Scaling laws for conventional helicopters

Dimension	Froude	Mach
Length	$L_m = L_p/N$	$L_m = L_p/N$
Time constant	$t_m = t_p/\sqrt{N}$	$t_m = t_p/N$
Speed	$V_m = V_p/\sqrt{N}$	$V_m = V_p$
Weight	$W_m = W_p/N^3$	$W_m = W_p/N^3$
Inertia mat.	$I_m = I_p/N^5$	$I_m = I_p/N^5$
Frequency	$\omega_m = \omega_p\sqrt{N}$	$\omega_m = \omega_p N$

thrust coefficient reflects the lift loading of the rotor. For a given, single rotor configuration, the maximum thrust is provided by the following expression

$$T_{\max} = (c_T/\sigma)_{\max} \rho (\pi R^2) (\Omega R)^2, \quad (26.3)$$

where  $\sigma$  represents the blade solidity (Sect. 26.3.4). This relation gives a maximum thrust that scales as  $T_{\max} \propto 1/N^3$  for a Froude model and as  $T_{\max} \propto 1/N^2$  for a Mach model. Once divided by the vehicle weight which scales as  $W \propto 1/N^3$ , it is deduced that Froude models present a similar thrust-to-weight ratio. On the contrary, for a Mach model, there is an increasing expected maximum thrust-to-weight:  $(T/W)_{\max} \propto N$ . Using these formulas, researchers in [26.8] calculated

the scaling parameters for several conventional helicopters that provide intuitive insight on how scaling laws work.

**LtA-UAS**

For the case of lighter-than-air vehicles simple scaling laws regarding the efficiency of the system hold. Considering the example of a spherical blimp, it is directly deduced that the lift force scales with the cubic power of the radius. On the other hand, its mass, which depends on the surface, scales with the square power of the radius and also does the drag force. This essentially indicates that larger blimps will tend to have a higher maximum lift to weight and lift-against-drag force ratios.

**FI-UAS**

Analysis of the scaling laws for flapping wing systems requires a different treatment, as the flight modality changes while the robot operates in *hover* mode or navigates in *forward flight*. Furthermore, the lift and drag coefficients are dependent on the airfoil characteristics of the wing and also on the flapping frequency, a fact that further increases the complexity of the analysis on the effect of scale. Section 26.6 provides insight on how to deal with this challenging issue so that proper flapping wing systems design is achieved.

## 26.3 Basics of Aerodynamics and Flight Mechanics

Assembling an analytic representation of a UAS involves the derivation of approximative expressions for the aerodynamic forces, accounting for the actuator dy-

namics and appending the resulting effect to the vehicle body equations of motion. The goal of this section is to provide the necessary insight and understanding of

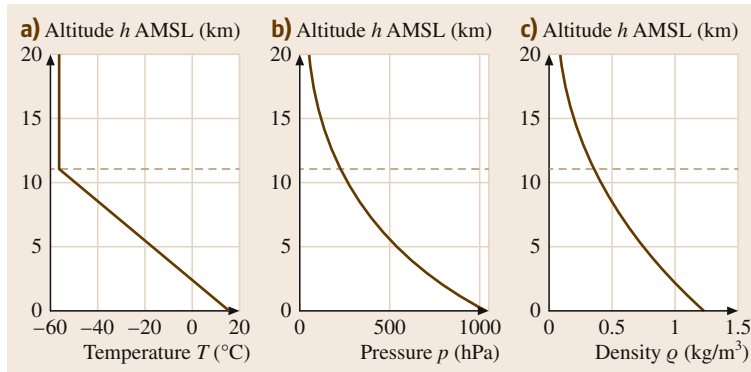


**Fig. 26.6** Variation of (a) air temperature, (b) pressure, and (c) density with altitude in the lower part of the International Standard Atmosphere. The tropopause, above which the temperature is not further decreasing, corresponds to the red dashed line. It constitutes the upper limit of common weather phenomena

the underlying mechanisms and physical phenomena along with the derivation of the formulae for the most dominant effects one has to account for with any UAS configuration.

### 26.3.1 Properties of the Atmosphere

Assessing flow properties forms the basis for any further qualitative or quantitative aerodynamic analysis relevant for aircraft design, modeling and control. The international standard atmosphere (ISA) [26.9] provides a reference for the average main air characteristics as a function of altitude. Figure 26.6 shows the evolution of air temperature  $T_{\text{air}}$ , pressure  $p$ , and density  $\rho$ . These parameters largely affect the Reynolds number  $Re$ , which can be interpreted as the influence of inertial forces as compared to viscous forces of a flow, as well as the Mach number  $Ma$  representing the ratio of airspeed versus speed of sound.

It is noteworthy that the above parameters may be brought into relationship by the ideal gas law

$$p = \rho RT_{\text{air}}, \quad (26.4)$$

with  $R = 286.97 \text{ m}^2/\text{s}^2/^\circ\text{K}$  denoting the ideal gas constant of air.

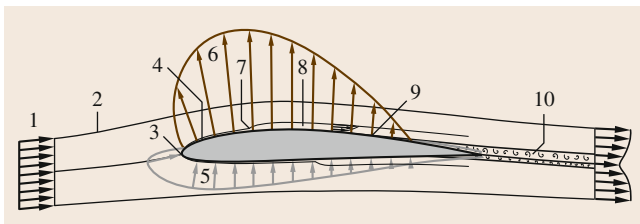


**Fig. 26.7** Characteristics of a 2-D flow around an airfoil 1 – Free stream velocity field, 2 – Streamline, 3 – Stagnation point, 4 – yLaminar boundary layer, 5 – Overpressure, 6 – ySuction, 7 – Transition point, 8 – Turbulent boundary layer, 9 – Separation point, 10 – Separated flow

In contrast to *aerodynamics*, where forces, first and foremost lift, is generated by motion of an object through the air, the *aerostatic* lift force is formed solely by static properties of an object. It forms the basis of operation for a balloon or blimp.

According to Archimedes' principle, the aerostatic lift  $L_{\text{stat}}$  pointing upward, amounts to

$$L_{\text{stat}} = \rho Vg - mg, \quad (26.5)$$

where  $g$  stands for the Earth gravitational acceleration,  $V$  for the volume of the object, and  $m$  for its mass. To state an example, consider a helium balloon of spherical shape with a diameter amounting to 1 m in the lower atmosphere. Neglecting its hull weight (thus with  $m = \rho_{\text{helium}}V$ ), it will generate an aerostatic lift force of 5.4 N, representing an upper bound for any kind of total design mass including payload. Increasing the diameter of said sphere to 1.5 m has the huge effect of increasing lift to 18.1 N.

### 26.3.2 General Fluid Dynamics and 2-D Flow around Airfoils

A general airflow around an aircraft is three-dimensional, unsteady, and may be turbulent, even interacting with a nonrigid structure. In this setting, computations are almost intractable. We will thus rely on certain simplifications in order to allow simpler calculations and notably enhancing the understanding of a flow field together with resulting forces and moments. In both airplane and rotorcraft aerodynamics, the assumption of a locally two-dimensional (2-D) flow can be very helpful to serve as a starting point for more advanced computation.

Before diving into a formal treatment, the example in Fig. 26.7 depicts some characteristic elements of 2-D flow around an airfoil.

Notice that the pressure distribution on the airfoil contour is induced by the flow field, making the most



significant contribution to the aerodynamic force and moment. However, also viscous effects yield a typically unwanted share in the overall force (and moment) in the form of shear stress transmitted to the surface. The elements overviewed in Fig. 26.7 will now be explained in the following paragraphs.

### Finite Control Volume Analysis: Mass and Momentum Conservation

Consider a finite control volume  $B$  bounded by the surface  $S$  with normal  $\mathbf{n}$ , which may contain a body or airfoil, depending on the context. For convenience, parts of the boundaries are often chosen to be streamlines (in 2-D) or stream surfaces (in 3-D). For this volume, the *conservation of mass* must be fulfilled

$$\iint_S \rho \mathbf{v} \cdot \mathbf{n} dS, \quad (26.6)$$

where  $\mathbf{n}$  denotes the fluid velocity vector.

From classical Newtonian mechanics, we can furthermore postulate the applicability of *conservation of linear and angular momentum*

$$\begin{aligned} \mathbf{F}_{\text{tot}} = & \iint_S \rho \mathbf{v} (\mathbf{v} \cdot \mathbf{n}) dS + \iint_S p \mathbf{n} dS \\ & + \frac{\partial}{\partial t} \iiint_B \rho \mathbf{v} dB, \end{aligned} \quad (26.7)$$

$$\begin{aligned} \mathbf{M}_{\text{tot}} = & \iint_S \rho (\mathbf{v} \times \mathbf{r}) (\mathbf{v} \cdot \mathbf{n}) dS \\ & + \frac{\partial}{\partial t} \iiint_B \rho (\mathbf{v} \times \mathbf{r}) dB, \end{aligned} \quad (26.8)$$

where  $\mathbf{r}$  denotes the position vector.

### Differential Volume Analysis: Euler and Bernoulli Equations

When applied to a differential volume and assuming inviscid flow, (26.7) can be used to derive *Euler's equation*

$$\rho \left( \frac{\partial}{\partial t} + \mathbf{v} \cdot \nabla \right) \mathbf{v} + \nabla p = \mathbf{0}. \quad (26.9)$$

This equation forms the basis of many finite-element-based numerical tools neglecting viscous effects outside the boundary layer. Such methods employ potential flow theory along with some boundary layer analysis module; free example tools are JavaFoil [26.10]

and xfoil [26.11] for 2-D flow computation as well as XFLR [26.12] allowing also 3-D flow extensions.

When applying (26.9) along a streamline and under the assumption that the flow is incompressible (a fair assumption for low-speed aerodynamics up to  $\text{Ma} = 0.3$ ), *Bernoulli's equation* relating speed ( $V_t$ ) and pressure can be formulated

$$\rho \frac{V_t^2}{2} + \rho gh + p = \text{const}, \quad (26.10)$$

where  $g$  denotes gravitational acceleration and  $h$  the elevation – the aerostatic pressure component  $\rho gh$  can often be neglected due to small elevation changes along a streamline.

### Viscous Effects and the Boundary Layer

While it is often a valid approximation to neglect viscous effects far enough from the body surfaces, they have to be considered within the boundary layer, where the fluid is slowed down to meet the speed of the surface. The friction shear stress  $\tau_w$  transmitted to the surface is characterized by the gradient of the flow speed perpendicular to the surface

$$\tau_w = \mu \frac{dU}{dn}, \quad (26.11)$$

where  $\mu$  denotes the dynamic viscosity of the fluid,  $U$  stands for the airspeed parallel to the surface, and  $n$  for the coordinate along the surface normal  $\mathbf{n}$ . This tangential fluid velocity gradient in the boundary layer is visualized qualitatively in Fig. 26.7.

The boundary layer will be laminar around the nose, with the fluid moving parallel to the surface. At some point (at a critical local Reynolds number), however, influenced by disturbances such as surface roughness, a transition to a turbulent boundary layer will occur: it is characterized by stochastic fluctuations, significantly thicker and producing substantially more friction than before the transition.

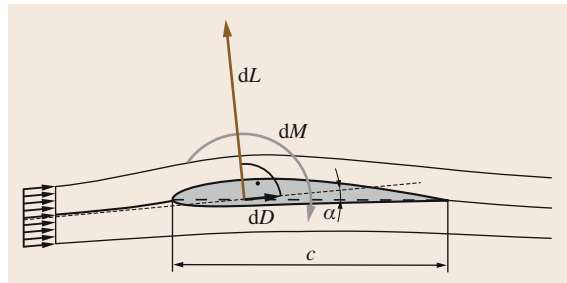


**Fig. 26.8** Decomposition of the aerodynamic force by a 2-D flow around an airfoil: the section lift  $dL$  denotes the component perpendicular to the far-field inflow, and drag  $dD$  the one parallel to it

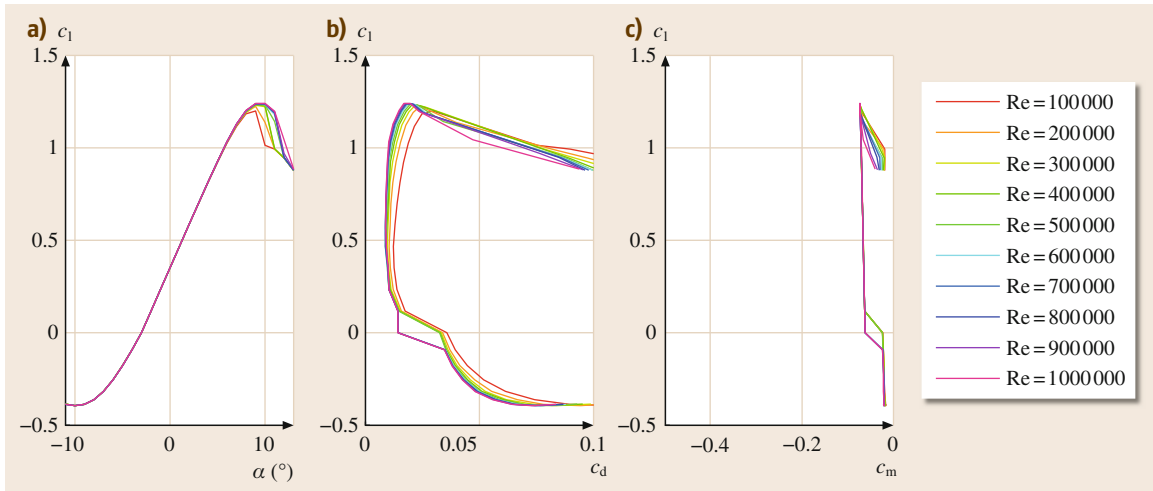


**Fig. 26.9a–c** SA7036 low-speed airfoil lift (a), drag (b), and moment (c) polars for various Reynolds numbers calculated by Javafoil

### Section Lift, Drag, and Moment Representation with Dimensionless Coefficients

Historically and for practical reasons, the aerodynamic force is split into a component perpendicular to the inflow direction called *lift*, and a second one parallel to the inflow called *drag*. We write 2-D lift, drag, and moment as infinitesimal quantities  $dL$ ,  $dD$ , and  $dM$ , respectively, as opposed to  $L$ ,  $D$ , and  $M$  designating physical forces of a whole airplane. Figure 26.8 visualizes these quantities. Furthermore, we define the angle of attack  $\alpha$  as the angle between inflow direction and the chord line of length  $c$  connecting airfoil leading edge and trailing edge. Note that force and moment are reduced to the point at  $0.25c$ , i. e., one quarter of the chord behind the leading edge.

Dimension analysis suggests the formulation of aerodynamic forces and moments in terms of section lift, drag, and moment coefficients  $c_l$ ,  $c_d$ , and  $c_m$

$$dL = \frac{1}{2} \rho V_t^2 c_l c dy, \quad (26.12)$$

$$dD = \frac{1}{2} \rho V_t^2 c_d c dy, \quad (26.13)$$

$$dM = \frac{1}{2} \rho V_t^2 c_m c^2 dy, \quad (26.14)$$

where  $V_t$  stands for the inflow speed and  $dy$  denotes an infinitesimal length element perpendicular to the 2-D flow (which can be interpreted as a length element into span-wise direction of an infinitely long wing).

These coefficients largely depend on the angle of attack  $\alpha$ ; but furthermore, the Reynolds and Mach num-

bers significantly influence them as well. The angle of attack dependences are typically given in the form of section lift, drag and moment polars, an example of which is provided in Fig. 26.9. Note that the drag component is originating both from viscous skin friction as well as form drag, caused by an asymmetric pressure distribution due to boundary layer development and separation. The lift curve shows its characteristic linear increase with increasing  $\alpha$  for small angles of attack. The maximum and minimum lift values beyond which stall is entered are clearly visible in the lift polar. Note that the aerodynamic performance  $c_l/c_d$  of the airfoil generally decreases with smaller Reynolds numbers as expected. The choice of reference point at  $0.25c$  typically leads to a mostly constant moment coefficient when varying  $\alpha$ ,  $c_l$ , respectively, as can be seen in Fig. 26.9 as well.

### Separation and Stall

At the upper side of the airfoil, the fluid is moving from the under-pressure region toward a higher pressure at the trailing edge; the slower moving fluid in the boundary layer will at some point not be able to follow this adverse pressure gradient, leading to flow separation. As the angle of attack is increased, the separation point suddenly moves far toward the leading edge: this condition is referred to as stall, with the catastrophic consequence of significant loss of lift and increase of drag. Figure 26.10 illustrates the changes in the flow and pressure distribution when varying the angle of attack. Note that the maximum lift and stall conditions are highly influenced by the choice of airfoil, Reynolds number, and Mach number.

### 26.3.3 Wing Aerodynamics

So far the 2-D flow characteristics around airfoils were treated. This will form the basis for the understanding and computation of lift and thrust forces generated on any type of aircraft; the following treatment of a finite wing serves as an important example of how to include three-dimensional (3-D) flow effects.

Recording lift and drag polars for a finite wing rather than just for its airfoil reveals less lift increase per angle of attack increase, less maximum lift, and higher drag at raised angles of attack. These observations are related to the concept of *induced flow* to be treated in the following.

#### Vortex System of a Wing

As a direct consequence of lift, we observe a downward flow deflection across an airfoil. This is intuitively explained with conservation of linear momentum as stated in (26.7). Assuming an inviscid and incompressible fluid, the flow may be modeled with potential field theory [26.13], where the velocity vector field is defined as the gradient of a scalar function. This concept allows for the insertion of singularities into a free stream, such as sources, sinks, and vortices. Figure 26.11 shows a first approximation using a single vortex – conceptually illustrating the flow characteristics around a simplified wing. The vortex system consists of the bound vortex and tip vortices; note that the vortex will in theory have to be closed to a ring by a starting vortex. In practice, i. e., in the presence of friction, the vortices will of course decay over time. Figure 26.12 illustrates the existence of tip vortices trailing an airplane wing.

The vortices induce a downwash area behind the wing; nevertheless, the trailing vortices will also induce some downward flow at the wing.

#### Induced Drag

With the simplified concept of the vortices around a wing in mind, we conclude that the wing lift induces downward flow, thus reducing the effective angle of attack when looking at the 2-D-flow of a wing cross-section. Figure 26.13 illustrates this reduction of the angle of attack from  $\alpha_f$  (free stream) to  $\alpha_e$  (effective) by the induced angle  $\alpha_i$  that is caused by the induced flow component  $w_i$ . Note that this reduction of angle of attack is typically resulting in a smaller lift. Furthermore, when decomposing the lift into components parallel and perpendicular to the free stream velocity, it becomes apparent that a part  $dD_i$  of the lift results parallel to the effective inflow, thus will contribute to the overall drag of the wing. The integral of these components is referred to as induced drag. The actual amount of induced drag largely depends on the wing geometry; a variety of

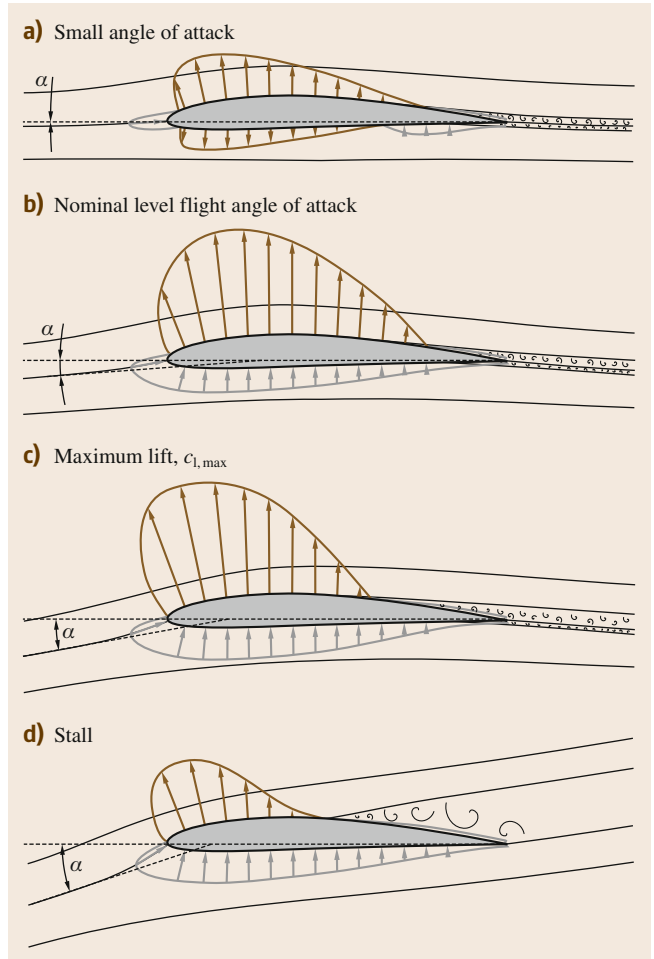


**Fig.26.10a–d** Changes in the flow characteristics with increasing angle of attack  $\alpha$ . For a small  $\alpha$  (a) the example nonsymmetric airfoil will generate some lift. (b) depicts nominal operation. At some  $\alpha$ , the maximum lift  $c_{l,max}$  is reached (c). Beyond that angle of attack, stall occurs (d)

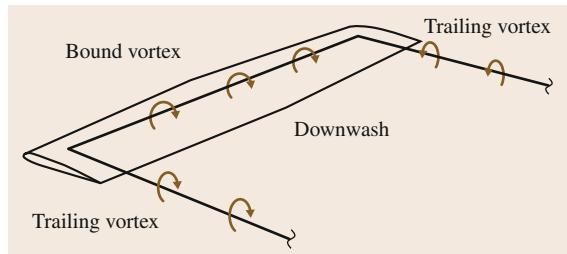


**Fig. 26.11** Simplified representation of the wing vortex system: as a consequence of lift, a bound vortex is formed along with trailing wingtip vortices inducing downwash

approaches have been employed in order to minimize induced drag, the most popular of which are winglets.



**Fig. 26.12** Wake vortex study by NASA at Wallops Island: the tip vortices are visualized using colored smoke rising from the ground

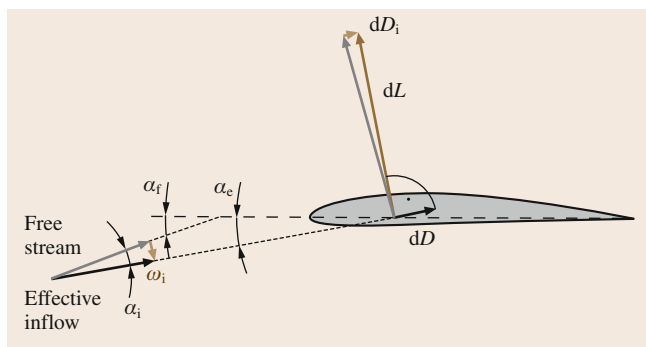


**Fig. 26.13** Induced drag on a finite wing cross section: the induced downwash  $w_i$  causes a reduced effective angle of attack. As a consequence, the lift  $dL$  contains a component  $dD_i$  parallel to the free stream velocity vector

For an approximately elliptical lift distribution, the induced drag coefficient can be roughly calculated as

$$c_{D,i} = \frac{C_L^2}{\pi e \Lambda}, \quad (26.15)$$

with the aspect ratio  $\Lambda$  and the Oswald efficiency  $e$  (deviation from the truly elliptic distribution) amounting from 0.7 to 0.85 for typical configuration.

### Lifting Line Method

In the following, we present one example of how to numerically approximate the lift and drag distribution of a wing including induced drag. The lifting line method is a 2.5-D (two-and-a-half-dimensional) approach in which the induced flow is viewed as generated by several discrete horseshoe vortices rather

than just one as introduced qualitatively earlier. Figure 26.14 depicts the geometry and variables involved. Note that the method only provides reliable results, if the assumption holds that spanwise flow is negligible; in particular, spanwise variation of parameters such as chord length and twist is supposed to be rather small. The Kutta–Joukowski theorem relates circulation and lift; applied to a discrete wing segment, we obtain

$$\Gamma_k = \frac{1}{2} c_k c_{l,k}(\alpha_{\text{eff}}) V_t, \quad (26.16)$$

with the segment (index  $k$ ) circulation  $\Gamma_k$ , the local chord length  $c_k$ , and the local airfoil lift coefficient  $c_{l,k}$ . The lift coefficient depends on the effective angle of attack:  $\alpha_e = \alpha_f - \alpha_i$ . The induced downwash at position  $\mathbf{m}_k$  is obtained by adding the induced speeds of all the individual vortices according to Biot–Savart

$$w_{i,k} = \sum_{j=1}^{n+1} \frac{\Gamma_j \mathbf{e}_V}{4\pi \|(\mathbf{p}_j - \mathbf{m}_k) \times \mathbf{e}_V\|} \times \left( 1 + \frac{(\mathbf{p}_j - \mathbf{m}_k) \cdot \mathbf{e}_V}{\|(\mathbf{p}_j - \mathbf{m}_k)\|} \right), \quad (26.17)$$

where  $\mathbf{e}_V$  stands for the (unit) direction of flight. At  $\mathbf{m}_k$ , the induced angle of attack is calculated as

$$\alpha_{i,k} = \arctan \frac{w_{i,k}}{V_t} \approx \frac{w_{i,k}}{V_t}. \quad (26.18)$$

Together with the respective 2-D polar data, the above relations allow calculating the lift, drag, and moment distribution (with respect to the free inflow direction  $\mathbf{e}_V$ ) from a known circulation distribution, and can be summed and reduced to, e.g., the center of mass of a whole airplane. Note that the section lift coefficient is often approximated linearly as  $c_l(\alpha) \approx c_{l,0} + c_{l,\alpha} \alpha$ , which allows for a direct solution when applying (26.16) and (26.17). More accurate results, in particular in the domain near maximum lift, however, are obtained by using the nonlinear lift polar. In this case, a standard iterative numeric solver may be used. Furthermore, airfoil data with deflected control surfaces can be included, allowing to calculate control moments (and forces).

Note that the above method is just one example of numerically solving for the wing characteristics knowing the 2-D airfoil properties (polars) – well-suited for low-speed medium to high aspect ratio wings. For an overview on alternatives, the reader is referred to, e.g., [26.13].

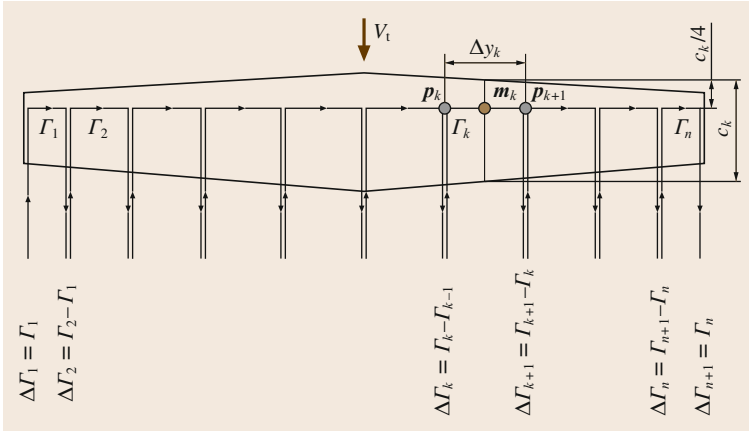


**Fig. 26.14**  $k$  horse shoe vortices with circulation  $\Gamma_k$  placed on the wing to model the induced flow. The lifting line is imagined through the quarter-chord ( $c_k/4$ ) locations. Vortex threads with strength  $\Delta\Gamma_k$  are leaving the wing at the points  $p_k$  along the inflow and induce downwash at the locations  $m_k$

### 26.3.4 Performance of Rotors and Propellers

The propulsion mechanism found on many robotic aerial vehicles is commonly a specific configuration of propellers or rotors. In the case of a robotic airplane, forward facing propellers produce thrust forces compensating drag in forward flight. In case of a tail sitter or multicopter UAV, the propellers may be facing up (or down) and produce the main lift component compensating the vehicle’s weight allowing it to hover in the air. Similarly, the more classic helicopter-type configurations (single rotor with tail rotor, coaxial rotor, tandem rotor, etc.), use rotors to generate the required thrust force to fly.

In order to decide on a suitable rotor or propeller geometry and to define requirements for the UAV motor drives, models must be available which allow for an assessment of the thrust and torque characteristics of a particular rotor or propeller. For this purpose, the blade element momentum theory (BEMT) has found widespread use, as it often provides a prediction accuracy which is acceptable for the UAV design process (despite its simplicity).

#### Blade Element Momentum Theory

One of the basic difficulties in aerodynamic rotor and propeller studies is the prediction of the induced inflow velocities discussed in Sect. 26.3.3. BEMT addresses this problem by combining two simple modeling approaches, namely momentum theory (MT) and blade element theory (BET) which individually cannot directly resolve this issue in an accurate manner [26.14].

The basic idea of momentum theory is to consider the revolving propeller or rotor as a propulsion disk which produces a thrust force by accelerating the surrounding (incompressible) air mass passing through it. A boundary volume is defined encapsulating the

propulsion disc. Subsequently, the laws of mass, momentum and power conservation are formulated across the boundaries of the defined control volume. The concept of this propulsion disk as well as the corresponding control volume are visualized in Fig. 26.15.

From this simplistic model, two main conclusions may be drawn. First and foremost, it is possible to establish a relation between the induced velocity  $v_i$  at the propulsion disk and the produced thrust force  $T$ . In normalized form, it can be expressed as

$$c_T = 2\lambda_i(\lambda_i + \lambda_\infty) \tag{26.19}$$

To simplify notation, the external airflow velocity  $v_\infty$  as well as the induced velocity  $v_i$  have been normalized with the rotor or propeller tip speed  $\Omega R$

$$\lambda_i = \frac{v_i}{\Omega R}, \quad \lambda_\infty = \frac{v_\infty}{\Omega R}, \tag{26.20}$$

and the nondimensional thrust coefficient  $c_T$  is defined as

$$c_T = \frac{T}{\rho(\pi R^2)(\Omega R)^2} \tag{26.21}$$

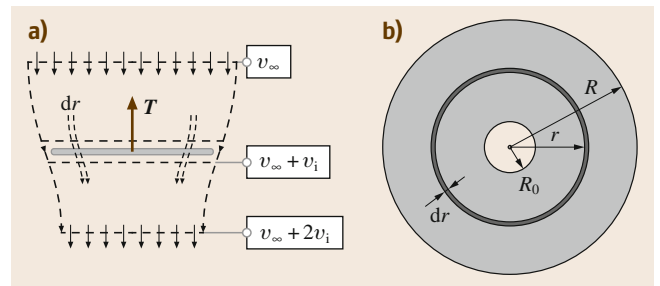


**Fig. 26.15** (a) Side view on the slipstream control volume encompassing the MT propulsion disc. (b) Top view on MT propulsion disk with incremental annular section and root cutout



The parameter  $\rho$  corresponds to the density of air,  $R$  to the rotor or propeller radius, and  $\Omega$  to the rotor or propeller angular speed.

In case of a robotic airplane, the velocity  $v_\infty$  at the start of the control volume corresponds to the body forward flight velocity  $V_1$  and in case of a rotorcraft configuration to the body climb respectively descent rate  $w$ .

Similarly, an incremental expression for the thrust coefficient may be found from MT by evaluating the mass, moment, and power conservation laws over an annular ring of the defined control volume only. The corresponding expression can be found as

$$dC_T^{\text{MT}} = 4\lambda_i(\lambda_i + \lambda_\infty)\bar{r}d\bar{r}, \quad (26.22)$$

where  $\bar{r} = \frac{r}{R}$  and  $d\bar{r} = \frac{dr}{R}$  are the normalized radial location and the radial increment of the propulsion disk annulus.

Another relevant conclusion that may be drawn from MT is that ideally, the induced component  $v_i$  of the slipstream velocity at the propulsion disk will accelerate to two times its initial value before leaving the control volume. In consequence to this acceleration of the flow field, the radial slipstream boundary will (in the ideal case) contract to half the propulsion disk area at the end of the control volume.

For the BET approach, the modeling process starts by investigating the aerodynamic lift and drag forces  $dL$  and  $dD$  on an individual rotor or propeller blade revolving around its shaft. These lift and drag forces produced by each airfoil segment depicted in Fig. 26.16, contribute to the total thrust and torque increments  $dT$  and

$dQ$  of the respective rotor or propeller annular section. The corresponding relation can be established as

$$dT = N_b(dL - \Phi dD) \approx N_b dL, \quad (26.23)$$

$$dQ = N_b r(dD + \Phi dL). \quad (26.24)$$

In this context,  $N_b$  represents the number of rotor or propeller blades and  $\Phi$  corresponds to the local inflow angle which is assumed to remain small. Under this assumption, the inflow angle  $\Phi$  can be directly derived as the ratio between the local perpendicular inflow velocity  $U_P \approx v_i + v_\infty$  and the tangential velocity  $U_T \approx \Omega r$  visualized in Fig. 26.16b. Additionally, the assumption introduced in (26.23) is justified by the fact that at low angles of attack  $\alpha$ , the drag forces  $dD$  are at least one order of magnitude smaller than the corresponding lift forces  $dL$ .

Based on (26.23) and the definition of the lift increment (26.12), the local thrust coefficient at each radial blade station  $r$  may be derived as

$$dC_T^{\text{BET}} = \frac{1}{2} \sigma c_l \bar{r}^2 d\bar{r}, \quad \text{with} \quad \sigma = \frac{N_b c}{\pi R}. \quad (26.25)$$

The parameter  $c$  corresponds to the local blade chord and  $\sigma$  is the so-called rotor or propeller *solidity*. The solidity is a rough metric representing how much of a propulsion disk is covered by rotor or propeller blades. The aerodynamic parameter  $c_l = c_l(\alpha, \text{Re}, \text{Ma})$  corresponds to the airfoil lift coefficient in function of the local angle of attack  $\alpha$  and the local Reynolds and Mach numbers  $\text{Re}$  and  $\text{Ma}$ .

Accordingly, as established in (26.25), the thrust produced by a rotor or propeller strongly depends on the angle of attack  $\alpha$ , which itself is a function of the local airfoil pitch angle  $\theta$  and the inflow angle  $\Phi$

$$\alpha = \theta - \Phi \approx \theta - \frac{U_P}{U_T}. \quad (26.26)$$

In conclusion, MT as well as BET are capable of establishing a meaningful relation between the induced velocities  $v_i$  and the resulting thrust force  $T$ . However, none of the two theories are capable of accurately predicting rotor or propeller performance as either the radial distribution of the induced velocity or the radial distribution of the thrust coefficient must be known to compute the other.

The basic idea behind BEMT is to combine the thrust expression (26.22) resulting from MT with the thrust expression (26.25) from BET to compute the induced inflow velocity independently of the thrust force. Different BEMT implementations are possible depending on how willing one may be to introduce further assumptions for the section lift coefficient  $c_l$ .

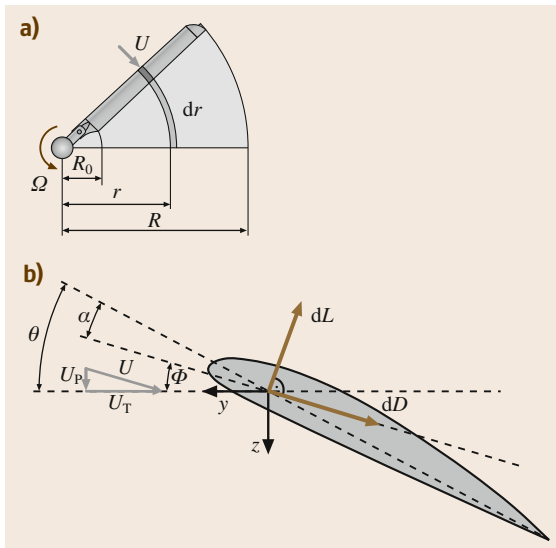


**Fig. 26.16** (a) Rotor blade revolving around its shaft. (b) Blade element of a revolving rotor blade

Reference [26.14] presents a straightforward approach tailored toward helicopter rotors operating below stall by introducing a linear model for  $c_l$  in function of the angle of attack

$$c_l = c_{l1}\alpha + c_{l0}. \quad (26.27)$$

The parameters  $c_{l0}$  and  $c_{l1}$  can be computed from the lift polars of a particular airfoil geometry for a given range of angles of attack, Reynolds, and Mach numbers. This linear approximation may have limited validity for very low Reynolds numbers and strongly cambered airfoils but is in general acceptable for many typical airfoil geometries found on UAV rotors and propellers. Assembling (26.22) and (26.25) under the assumption (26.27), an algebraic expression of the radial induced inflow distribution can be derived as

$$\lambda_i(r, \lambda_\infty) = \sqrt{A^2 + B - \bar{A}}, \quad (26.28)$$

$$A = \frac{\sigma c_{l1}}{16} - \frac{\lambda_\infty}{2},$$

$$\bar{A} = \frac{\sigma c_{l1}}{16} + \frac{\lambda_\infty}{2},$$

$$B = \frac{\sigma c_{l1}}{8} \theta' \bar{r}.$$

Note that the lift-curve offset  $c_{l0}$  has been absorbed in the virtual pitch angle

$$\theta' = \theta + \frac{c_{l0}}{c_{l1}}, \quad (26.29)$$

to simplify the notation.

Once the approximate radial distribution of inflow velocities has been found, the local rotor or propeller thrust increments (26.25) can be computed. Similarly, the rotor or propeller torque increments derived from BET as

$$dc_{Q_i}^{\text{BET}} = dc_{Q_i} + dc_{Q_0}, \quad (26.30)$$

$$dc_{Q_i} = \frac{1}{2} \sigma c_l (\lambda_i + \lambda_\infty) \bar{r}^3 d\bar{r}, \quad (26.31)$$

$$dc_{Q_0} = \frac{1}{2} \sigma c_d \bar{r}^3 d\bar{r}, \quad (26.32)$$

can be evaluated based on the inflow distribution given in (26.28). For clarity, the total torque coefficient increment has been separated into its induced component  $dc_{Q_i}$  originating from the lift forces and its profile component  $dc_{Q_0}$  due the drag forces. The aerodynamic drag coefficient  $c_d = c_d(\alpha, \text{Re}, \text{Ma})$  can be approximated using a quadratic function in dependency of the angle of attack [26.14]

$$c_d = c_{d2}\alpha^2 + c_{d1}\alpha + c_{d0}. \quad (26.33)$$

The parameters  $c_{d0}$ ,  $c_{d1}$ , and  $c_{d2}$  can be computed from the drag polars of the modeled airfoil.

Consequently, the thrust and torque increments may be integrated along the radial direction of the rotor or propeller disk to compute the total thrust and torque coefficients

$$c_T = \int_0^R dc_T^{\text{BET}}, \quad (26.34)$$

$$c_Q = \int_0^R dc_Q^{\text{BET}}. \quad (26.35)$$

These thrust and torque integrals are usually evaluated numerically, as the blade pitch  $\theta = \theta(r)$  as well as the blade chord  $c = c(r)$  may be nonlinear functions of the radial direction  $r$  (blade *twist* and *taper*).

Finally, note that the presented theory may be extended to provide performance estimates under lateral inflow velocities such as in case of a rotorcraft in forward flight and may also be used to assess other types of rotor or propeller configurations such as, e.g., the coaxial rotor. Also note that the prediction accuracy of BEMT tools can be further improved by accounting for tip-loss effects and the nonlift producing rotor or propeller hub, e.g., using the Prandtl tip-loss function also presented in [26.14] and incorporating a root cutout radius  $R_0$ .

The resulting predictions are generally in good agreement with experimental data – nevertheless, an experimental verification is strongly recommended.

### 26.3.5 Drag

The sources of drag on aircraft are manifold: historically, the distinction between the lift-dependent *induced drag* and *parasite drag* is made. The latter is further subdivided into *skin friction drag* due to viscous shear stress at the surface, and *form drag*, generated by pressure loss along bodies (i.e., due to boundary layer development or even flow separation). Both these components contribute to the airfoil *profile drag*, i.e., the section drag coefficient  $c_d$  introduced before.

On a whole aircraft, many more drag sources are distinguished. For an exhaustive overview, the interested reader is referred to [26.13]. In the following, we will present an overview of drag generated by different typical shapes; note that when simply summing drag of different shapes associated with aircraft parts, the result may be a helpful initial estimate, but can be inaccurate, because of neglecting the interaction of flows resulting in *interference drag*. Depending on the stage of the design process or the desired modeling accuracy, 2.5-D

computations or even full 3-D computational fluid dynamics (CFD) simulations might be necessary to satisfy the needs of aerodynamics calculations.

**Skin Friction**

The simple but important example of a flat plate of length  $l$  in parallel flow is well studied. As introduced in the airfoil theory Sect. 26.3.2, the boundary that develops will be laminar near the leading edge and transitions into a turbulent one, generating more drag, at some point downstream. The friction coefficient is defined as

$$c_f = \frac{2D_f}{\rho V_t^2 S_w}, \tag{26.36}$$

with the wetted surface  $S_w$  and the friction drag force  $D_f$ . According to [26.13], the coefficients can be approximated by

Laminar :  $c_f = 1.328 \text{Re}_l^{-0.5}, \tag{26.37}$



















Turbulent :  $c_f = 0.455 (\log_{10} \text{Re}_l)^{-2.58}. \tag{26.38}$

Note that the point of transition is depending on the local Reynolds number  $\text{Re}_x = \rho V_t x / \mu$ , where  $x$  denotes the coordinate along the flow from the leading edge of the plate. Depending on the surface roughness and ambient turbulence, the critical (transition) Reynolds number varies; as an average guess for a flat plate, it will be in the order of  $\text{Re}_{x,\text{crit}} = 3 \times 10^5$ .

**Drag Coefficients for Selected Bodies**

In the following, drag coefficients for a selection of 2-D and 3-D bodies of rotation are given, obtained

**Table 26.3** Bodies the drag coefficients of which are largely Reynolds number independent

	$c_D$ (2-D)		$c_D$ (3-D)	
		1.98		1.18
		2.0		1.0–1.2
		1.3		0.7
		2.0		1.1
		2.2		1.7
		1.4		0.4

from [26.13]. Table 26.3 overviews a category of bodies, the drag coefficients of which are largely indifferent to the Reynolds number, owing to their geometrically defined (sharp edge) flow separation point.

Rounder bodies, most prominently the cylinder in cross-flow or the sphere, however, show a distinctively different behavior quantified in Table 26.4: below a critical Reynolds number  $\text{Re}_{\text{crit}} \approx 4 \times 10^5$ , the drag coefficient is significantly higher, where separation occurs before boundary layer transition. In contrast, above the critical Reynolds number, the turbulent, more energetic boundary layer separates only further downstream, reducing the wake and thus the amount of form drag.




A third important object category is formed by streamlined and fuselage-like bodies: due to their comparably high skin friction part, the fineness ratio largely influences the drag coefficient (along with the Reynolds number). The fineness is defined as body length divided by body diameter. We introduce a volumetric drag coefficient as  $c_{Dm} = 2D / (\rho V_t^2 V_m^{2/3})$  with the body volume  $V_m$ . Interestingly, this is minimal and approximately constant at fineness ratios between 4 and 10, which provides a range for optimal sizing of such a body when a certain volume needs to be fitted. The values are given in Table 26.5.

**26.3.6 Aircraft Dynamics and Flight Performance Analysis**

Sections 26.3.1–26.3.5 shortly presented the basic theory of wings, rotors, and propellers as well as a few tools to assess their respective aerodynamic performance. To develop fully functional UAV platforms, merely evaluating the individual flight mechanisms is a good starting point but generally not sufficient.

Designing high-performance aircraft systems requires a fundamental understanding of how the respective design parameters affect the full flight dynamic response and application-specific capabilities. In order to comprehend how design changes affect an aerial

**Table 26.4** Sphere and cylinder drag coefficients

	$c_D$ (2-D)	$c_D$ (3-D)
		
$\text{Re} < \text{Re}_{\text{crit}}$	1.1	0.4
$\text{Re} > \text{Re}_{\text{crit}}$	0.27	0.15

**Table 26.5** Volumetric drag coefficients for fineness 4–10 (largely turbulent boundary layer)

Fuselages and nacelles	$c_{Dm} \approx 0.027$
Streamlined bodies	$c_{Dm} \approx 0.024$

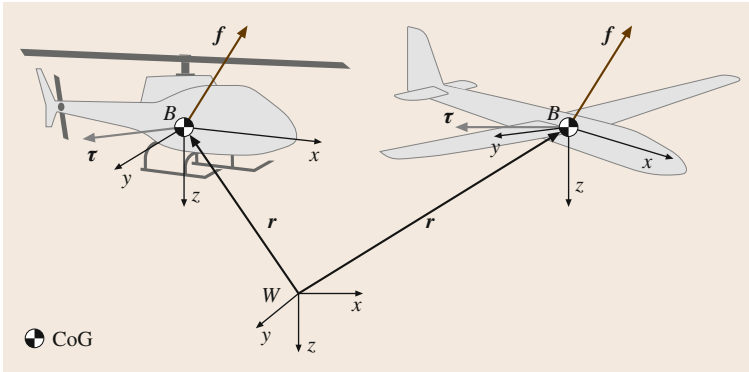


**Fig. 26.17** Coordinate frames with external forces and moments of rotorcraft and fixed-wing UAVs

robotic system, representative models of its flight dynamics are required. Such models must be capable of capturing the dominant system dynamics within the relevant part of the flight envelope. Furthermore, especially in an interdisciplinary field such as robotics, these models must be accessible to the nonaerodynamic expert (the roboticist) and thus need to be simple enough to provide the required insight for the aircraft design process.

As many other types of robots, robotic flight platforms may be treated as a multibody system where a set of interlinked bodies exchanges kinetic and potential energy under the influence of external forces and moments. For aircraft systems it is common to treat the entire aircraft as a single rigid body first, with related body coordinate frame attached, as visualized in Fig. 26.17. Additional dynamics such as for example rotor flapping (as in case of a helicopter system) may be appended to these body dynamics in a subsequent step.

The modeling process thus starts by treating the aircraft system as a rigid body affected by external forces  $\mathbf{F}$  and external moments  $\boldsymbol{\tau}$ . Using the Newton–Euler formalism to derive the aircraft body dynamics, one can directly write down the linear and angular momentum balance for a single rigid body

$$\begin{aligned} m({}^B\dot{\mathbf{v}} + {}^B\boldsymbol{\omega} \times {}^B\mathbf{v}) &= {}^B\mathbf{F}, \\ {}^B\mathbf{I}^B\dot{\boldsymbol{\omega}} + {}^B\boldsymbol{\omega} \times ({}^B\mathbf{I}^B\boldsymbol{\omega}) &= {}^B\boldsymbol{\tau}. \end{aligned} \quad (26.39)$$

For simplicity's sake, (26.39) is usually expressed with respect to a body fixed frame  $B$  located in the center of gravity of the aircraft. The velocity vectors  ${}^B\mathbf{v} = (u, v, w)^T$  and  ${}^B\boldsymbol{\omega} = (p, q, r)^T$  thus represent the aircraft linear and angular velocities with respect to  $B$ . The inertial properties of the above body dynamics are defined by the aircraft's total mass  $m$  and its second mass moment of inertia  ${}^B\mathbf{I}$  also expressed with respect to  $B$  and its origin.

The most relevant contribution to the forces  ${}^B\mathbf{F}$  and the moments  ${}^B\boldsymbol{\tau}$  originates from the aerodynamic flight components such as wings, propellers and rotors. By integrating (26.39) over time one may compute a prediction of the aircraft's dynamic response to these external forces and moments and thus the evolution of its absolute pose. This pose is commonly represented by the position of the vehicle's center of gravity  ${}^W\mathbf{r}_B = (x, y, z)^T$  as well as the vehicle's orientation relative to an earth fixed world frame  $W$  which is considered inertial. The aircraft orientation is commonly represented using rotation matrices or quaternions. In the case of the rotation matrix representation, the aircraft orientation may be parameterized in three dimensional space by three consecutive rotations with the roll, pitch, and yaw angles  $\varphi \in [-\pi, \pi]$ ,  $\theta \in [-\pi/2, \pi/2]$  and  $\psi \in [-\pi, \pi]$  as

$${}^W\mathbf{R}_B = \mathbf{R}_Z(\psi)\mathbf{R}_Y(\theta)\mathbf{R}_X(\varphi). \quad (26.40)$$

In this case, relations between the body frame velocities  ${}^B\mathbf{v}$  and  ${}^B\boldsymbol{\omega}$  and the world frame pose can be expressed as

$$\begin{aligned} {}^W\dot{\mathbf{r}} &= {}^W\mathbf{R}_B {}^B\mathbf{v}, \\ {}^W\dot{\mathbf{R}}_B &= {}^W\mathbf{R}_B [{}^B\boldsymbol{\omega}]^\times, \end{aligned} \quad (26.41)$$

where  $[{}^B\boldsymbol{\omega}]^\times$  corresponds to the skew-symmetric matrix of the vector  ${}^B\boldsymbol{\omega}$ .

In a minimal form, the orientation dynamics can be expressed in terms of roll, pitch, and yaw angles

$$\begin{pmatrix} \dot{\varphi} \\ \dot{\theta} \\ \dot{\psi} \end{pmatrix} = \underbrace{\begin{pmatrix} 1 & \sin \varphi \tan \theta & \cos \varphi \tan \theta \\ 0 & \cos \varphi & -\sin \varphi \\ 0 & \sin \varphi / \cos \theta & \cos \varphi / \cos \theta \end{pmatrix}}_{\mathbf{J}_r} {}^B\boldsymbol{\omega}. \quad (26.42)$$

Note that the Jacobian  $\mathbf{J}_r$  becomes singular at the boundaries of  $\theta = \pm\pi/2$ .

As a singularity-free, but still compact representation of orientation, quaternions may be used. Using the representation  ${}^W\mathbf{q}_B = (q_w, q_x, q_y, q_z)^T$  with real part  $q_w$ , the rotational kinematics become

$${}^W\dot{\mathbf{q}}_B = \frac{1}{2}\boldsymbol{\Omega}({}^B\boldsymbol{\omega}){}^W\mathbf{q}_B, \quad (26.43)$$

with the matrix  $\boldsymbol{\Omega}$  defined as

$$\boldsymbol{\Omega}({}^B\boldsymbol{\omega}) = \begin{pmatrix} 0 & {}^B\boldsymbol{\omega}^T \\ -{}^B\boldsymbol{\omega} & [{}^B\boldsymbol{\omega}]^\times \end{pmatrix}. \quad (26.44)$$

In summary (using quaternions), we thus have the equations of motion

$$\begin{aligned} {}^W\dot{\mathbf{r}} &= {}^W\mathbf{R}_B {}^B\mathbf{v}, \\ {}^W\dot{\mathbf{q}}_B &= \frac{1}{2}\boldsymbol{\Omega}({}^B\boldsymbol{\omega}){}^W\mathbf{q}_B, \\ {}^B\dot{\mathbf{v}} &= \frac{1}{m}{}^B\mathbf{F} - {}^B\boldsymbol{\omega} \times {}^B\mathbf{v}, \\ {}^B\dot{\boldsymbol{\omega}} &= {}^B\mathbf{I}^{-1} [{}^B\boldsymbol{\tau} - {}^B\boldsymbol{\omega} \times ({}^B\mathbf{I}^B\boldsymbol{\omega})]. \end{aligned} \quad (26.45)$$

Note that the external forces and moments are related to the system's actuator inputs  $\mathbf{u}$ , the vehicle's orientation with respect to  $W$  and they typically are also functions of the linear and angular body motion as well as additional dynamics terms, represented here by the vector  $\boldsymbol{\varepsilon}_r$

$${}^B\mathbf{F} = {}^B\mathbf{F}({}^W\mathbf{r}, {}^W\mathbf{q}_B, {}^B\mathbf{v}, {}^B\boldsymbol{\omega}, \boldsymbol{\varepsilon}_r, \mathbf{u}), \quad (26.46)$$

$${}^B\boldsymbol{\tau} = {}^B\boldsymbol{\tau}({}^W\mathbf{r}, {}^W\mathbf{q}_B, {}^B\mathbf{v}, {}^B\boldsymbol{\omega}, \boldsymbol{\varepsilon}_r, \mathbf{u}). \quad (26.47)$$

The additional dynamics  $\boldsymbol{\varepsilon}_r$  may account for structural dynamics such as rotor flapping in case of a robotic helicopter or relevant actuator dynamics.

The resulting nonlinear system dynamics can usually be cast into state-space form and represented as

$$\begin{aligned} \dot{\mathbf{x}} &= \mathbf{f}(\mathbf{x}, \mathbf{u}), \\ \mathbf{x} &= (\mathbf{x}_b, \mathbf{x}_r)^T, \\ \mathbf{u} &= (u_1, \dots, u_N)^T, \end{aligned} \quad (26.48)$$

where the nonlinear functions  $\mathbf{f}$  define the rate of change of the aircraft body states  $\mathbf{x}_b$  as well as the additional states  $\mathbf{x}_r$  affected by the set of  $N$  actuator inputs  $u_1$  to  $u_N$ .

In order to gain a deeper understanding of how (26.48) is affected by changes of the flight system's geometric, structural, inertial, and aerodynamic parameters, three main problems are commonly of relevance [26.15]:

- The *trim problem* deals with the computation of the set of actuator inputs  $\mathbf{u} = \mathbf{u}_0$  under which the nonlinear dynamic system presented in (26.48) remains in a desired trim point  $\mathbf{x} = \mathbf{x}_0$  and thus  $\mathbf{f}(\mathbf{x}_0, \mathbf{u}_0) = \mathbf{0}$ . The most simple example of such a trim point  $\mathbf{x}_0$  is the hover condition for a rotorcraft system where one may want to find the required rotor speed  $\Omega_0$  to hover or the steady forward flight condition for a fixed-wing UAV at a forward velocity  $V_t$ .
- The topic of *stability* deals with the question of how easily the system (26.48) will deteriorate from a specific trim condition  $(\mathbf{x}_0, \mathbf{u}_0)$  under the influence of small disturbances  $\Delta\mathbf{x}$  and  $\Delta\mathbf{u}$ . This investigation commonly involves the linearization of (26.48) according to

$$\begin{aligned} \mathbf{A} &= \left( \frac{\partial \mathbf{f}}{\partial \mathbf{x}} \right)_{\mathbf{x}=\mathbf{x}_0, \mathbf{u}=\mathbf{u}_0}, \\ \mathbf{B} &= \left( \frac{\partial \mathbf{f}}{\partial \mathbf{u}} \right)_{\mathbf{x}=\mathbf{x}_0, \mathbf{u}=\mathbf{u}_0}, \\ \Delta\dot{\mathbf{x}} &= \mathbf{A}\Delta\mathbf{x} + \mathbf{B}\Delta\mathbf{u}, \end{aligned} \quad (26.49)$$

where the eigenvalues and vectors of  $\mathbf{A}$  will provide deeper insight into the motion characteristics and stability properties of an aircraft.

- Analyzing the *System Response*

$$\mathbf{x}(t) = \mathbf{x}(0) + \int_0^t \dot{\mathbf{x}} dt \quad (26.50)$$

to characteristic inputs such as steps, pulses or specific input frequencies will provide additional information about the flight characteristics of a specific aircraft configuration.

These modeling and analysis concepts commonly find wide applicability for various types of robotic flight configurations and will be discussed in more detail for the specific UAV types presented hereafter.

### Actuator Dynamics

Deriving the aerodynamic forces is combined with the dynamic equations of motion in order to assemble a complete model of the flying vehicle. However, as the employed actuators are of naturally limited bandwidth, accurate modeling furthermore requires the integration of the relevant motor or servo dynamics.

Nowadays, motors utilized in small size unmanned systems often belong to the category of brushless direct-current (DC) electric motors (BLDC). BLDCs are synchronous motors powered by a DC electric source via an integrated switching power supply. The equations of motion for a such a system are essentially nonlinear and



rather complex. However, working with small UAS, we may solely focus on the input–output dynamics which can be described with the following transfer function

$$\frac{\Delta\omega(s)}{\Delta Q_m(s)} = \frac{-K_m(1 + \tau_\alpha s)}{(1 + \tau_m s)(1 + \tau_\alpha s) + K_m K_\alpha (K i_{e0})^2}, \quad (26.51)$$

where  $\Delta\omega(s)$ ,  $\Delta Q_m(s)$  correspond to the Laplace expressions of the linearized angular velocity and input torque,  $K_m$  is the mechanical gain,  $\tau_m$  represents the mechanical time constant,  $K_\alpha$  is the rotor gain,  $\tau_\alpha$  is the rotor time constant,  $K$  depends on electromagnetic properties of the motor and  $i_{e0}$  denotes the stator current linearization point [26.16]. Often, a satisfactory speed controller and BLDC dynamics description is obtained as the relation between a reference angular velocity

and the actual output taking the even simpler first-order form

$$\frac{\Delta\omega(s)}{\Delta\omega^r(s)} = \frac{1}{1 + \tau_{mc}s}, \quad (26.52)$$

with the time constant  $\tau_{mc}$  of the controlled motor.

Accounting for motor dynamics is essential for high-bandwidth control of agile vehicles that highly depend on such actuators (i. e., multirotors). However, in several other UAS configurations such as fixed-wing vehicles or conventional helicopters may, if needed, rather account for servo dynamics acting on control surfaces or a swashplate. Again, the relevant servo angle dynamics can be captured by an identified first-order transfer function of the form  $1/(1 + \tau_s s)$ , with the servo time constant  $\tau_s$ .

## 26.4 Airplane Modeling and Design

Ever since the beginning of aviation, a broad spectrum of airplanes has been built and operated successfully: size, speed, and maneuverability vary widely and as a function of application. Since design and modeling are strongly related, we want to first give an overview of the physical principles common to all such configurations, and provide analysis tools for characterizing static and dynamic properties of an airplane. The design problem somewhat constitutes the inverse problem: for specified target characteristics, the engineer needs to find a suitable configuration; we therefore provide a summary of design guidelines aimed at fast convergence to a suitable design. Finally, a simple and classical autopilot scheme is presented underlining the need for models also at that stage.

### 26.4.1 Forces and Moments

Consider Fig. 26.18 for the introduction of airplane geometry definitions and main forces. Forces and moments are reduced to the airplane center of gravity (COG). Note that the angle of attack (AOA)  $\alpha$  is defined as the angle between the  $x$ -axis and the true airspeed vector  $v_t$  projected into the  $x$ - $z$ -plane,  $\beta$  denotes the sideslip angle, causing a typically unwanted sideslip force  $Y$ ,  $L$  and  $D$  denote lift and drag,  $W$  stands for the weight and  $T$  for thrust, which may act into a direction different from  $x$  (at a thrust angle  $\epsilon_T$ ). We furthermore write the aerodynamic moment vector as  ${}^B\tau_A = [L_A, M_A, N_A]^T$ . Also note the introduction of the main control surfaces that are designed to mainly influence the aerodynamic moment: with ailerons, elevator,

and rudder, the roll ( $L_A$ ), pitch ( $M_A$ ), and yaw ( $N_A$ ) moments are controlled. The indicated flaps, if available, are used for increasing lift for take-off and landing, in order to achieve a slower minimum speed.

### Aerodynamic Forces and Moments

The aerodynamic forces and moments can be modeled to various accuracy using full 3-D CFD or with 2.5-D tools: Sect. 26.3.3 overviews such an approach which can be used to model the aerodynamic surfaces in incompressible flow. For enhanced accuracy, fuselages may be

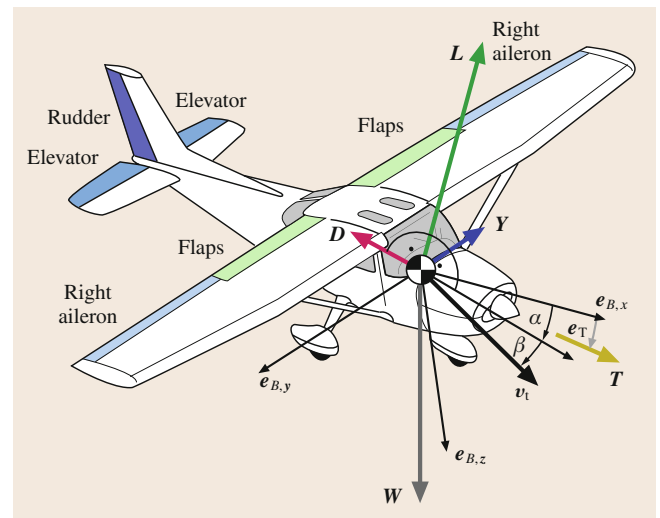


**Fig. 26.18** Geometric definitions and main forces acting on the airplane (general case, not in equilibrium)

considered using again a combination of potential flow (placing singularities) and boundary layer theory. Respective ready-to-use software such as AVL [26.17] and XFLR [26.12] is available for free.

The forces and moments may again be written with dimensionless coefficients as

$$L = \frac{1}{2} \rho V_t^2 c_L A, \quad (26.53)$$

$$D = \frac{1}{2} \rho V_t^2 c_D A, \quad (26.54)$$

$$M_A = \frac{1}{2} \rho V_t^2 c_M \bar{c} A, \quad (26.55)$$

with the wing area  $A$ , the mean chord length  $\bar{c}$ , and the true airspeed  $V_t = \|\mathbf{v}_t\|$ . The moments  $L_A$  and  $N_A$  are made dimension-less with the wingspan  $b$  rather than the chord length.

### Static Performance Considerations

Having characterized lift and drag of an airplane, three operating points are of particular interest.

First, stall is occurring at  $c_{L,\max}$ . This condition can be directly translated into constant-speed level-flight stall speed by applying the lift balance  $L = mg$ .

Second, the maximum  $c_L/c_D$  ratio, or the *glide ratio* characterizes the maximum aerodynamic efficiency, i. e., the operating point for maximum range (assuming constant propulsive efficiency).

Finally, the maximum  $c_L^3/c_D^2$  ratio, or the *climb factor* describes the condition at which power consumption is minimized, thus maximizing flight time (again assuming constant propulsion unit efficiency).

The latter two conditions have direct interpretation in gliding (or propulsion shut-off), in terms of maximum distance reached per altitude lost and minimum sink rate, respectively. Again, corresponding velocities can be found using the lift balance.

### Thrust

For detailed insight into the variety of propulsion systems and respective models, the interested reader is referred to [26.13, 18]. As an approximation for the important case of a propeller, the BEMT method as described in Sect. 26.3.4 is suggested. For many applications, choosing the propeller speed as the system input and neglecting motor dynamics is sufficient.

## 26.4.2 Static Stability

Various forms of stability constitute central characteristics of an airplane related to whether or not it can be flown by a human pilot or flight controller. Simple stability criteria can be derived by requiring reaction

forces and moments to be opposing a disturbance. We assume stationary conditions in the sense of constant linear and angular speeds: the respective force and moment balance is typically straightforward to apply in order to determine the starting point of the stability analysis.

### Longitudinal Static Stability

We will take a close look at the example of longitudinal static stability playing a central role in airplane analysis and design. Leaving aside possible influence of the propulsion unit, the respective directional stability criterion is stated as

$$\frac{\partial c_M}{\partial \alpha} < 0, \quad (26.56)$$

at the equilibrium condition  $c_M = 0$ . Figure 26.19 illustrates an exemplary moment coefficient as a function of AOA. Note that elevator actuation will move this curve up and down, and with it the equilibrium point (2) toward higher or lower angles of attack (i. e., lower or higher trimmed speeds). Figure 26.20 illustrates the forces and moments in the stable equilibrium

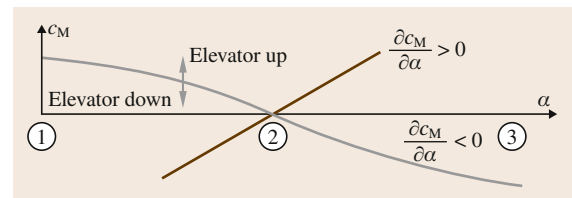


**Fig. 26.19** Moment coefficient  $c_M$  as a function of AOA  $\alpha$  the equilibrium point (2) is stable for  $\partial c_M / \partial \alpha < 0$  (brown curve)

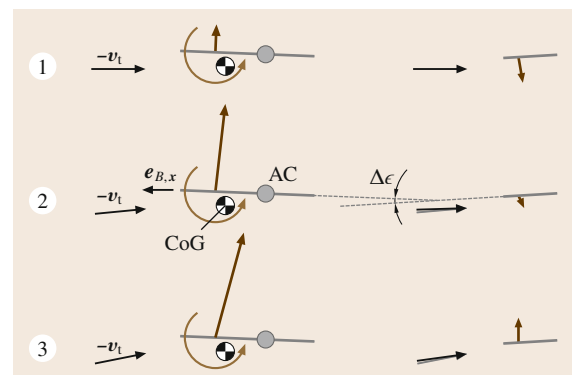


**Fig. 26.20** Forces and moments at the main wing and tail for zero lift (1), the stable equilibrium AOA (2), and for high lift (3). The forces and moments are drawn into the individual surfaces' aerodynamic centers. Note the tilted inflow at the tail due to downwash. The green filled circle denotes the overall airplane aerodynamic center (AC)

with a simplified airplane side-view as compared to the points (1) and (3), i. e., zero-lift ( $\alpha = 0$ ) and high-lift, respectively. The stability criterion can be equivalently stated as: the airplane COG needs to be *in front* of the airplane aerodynamic center. Note the main parameters that influence the stability are tail lever arm, tail area, the *longitudinal dihedral*  $\Delta\epsilon$  (Fig. 26.20 for its geometric definition), and the COG location along the  $x$ -axis.

### 26.4.3 Dynamic Model

While some core characteristics such as static stability and performance measures may already be established using aerodynamics coefficients only, we now turn to analyze the dynamics, since they provides a much richer insight into airplane characteristics.

For application of the 6-D (six-dimensional) rigid body dynamics (26.45), the forces and moments from the various sources need to be assembled and represented in the body frame

$${}^B\mathbf{F} = \begin{pmatrix} L \sin \alpha - D \cos \alpha + T \cos \epsilon_T \\ Y \\ -L \cos \alpha - D \sin \alpha + T \sin \epsilon_T \end{pmatrix} + {}^B\mathbf{W}, \quad (26.57)$$

$${}^B\boldsymbol{\tau} = \begin{pmatrix} L_A + L_T \\ M_A + M_T \\ N_A + N_T \end{pmatrix}, \quad (26.58)$$

with the weight in body coordinates  ${}^B\mathbf{W} = {}^B\mathbf{R}_W[0, 0, -mg]^T$ , and where the T-subscript indicates (possible) moment components from thrust. Note that the system inputs  $\mathbf{u}$  are hidden inside these forces and moments. Also be aware of  $\alpha$  and  $\beta$  containing parts of the state vector

$$\alpha = \arctan2(u_t, u_i), \quad (26.59)$$

$$\beta = \arcsin(v_t/V_t), \quad (26.60)$$

where the true airspeed components are used

$${}^B\mathbf{v}_t := \begin{cases} u_t \\ v_t \\ w_t \end{cases} = {}^B\mathbf{v} - {}^B\mathbf{R}_W^W \mathbf{w}, \quad (26.61)$$

with the wind vector  ${}^W\mathbf{w}$ .

Furthermore, due to the airplane symmetry plane, the inertia matrix becomes

$${}^B\mathbf{I} = \begin{pmatrix} I_{xx} & 0 & I_{xz} \\ 0 & I_{yy} & 0 \\ I_{xz} & 0 & I_{zz} \end{pmatrix}. \quad (26.62)$$

### Parametric Force and Moment Models

Let us consider the example of a simple airplane configuration with ailerons, a rudder and an elevator plus a propeller, driven by an electric motor at rotation speed  $\omega_p$ .

We define the system input vector  $\mathbf{u} = [\delta_a, \delta_c, \delta_r, \delta_T]$  as normalized aileron, rudder, and elevator action,  $\delta_a, \delta_c, \delta_r \in [-1, 1]$  as well as (normalized) thrust  $\delta_T \in [0, 1]$ .

The fully parametric nonlinear model provided below largely follows [26.19]. We approximate the lift, drag as well as sideslip coefficients with polynomials in  $\alpha$  and  $\beta$

$$\begin{aligned} c_L &\approx c_{L,0} + c_{L,\alpha}\alpha + c_{L,\alpha^2}\alpha^2 + c_{L,\alpha^3}\alpha^3, \\ c_D &\approx c_{D,0} + c_{D,\alpha}\alpha + c_{D,\alpha^2}\alpha^2 + c_{D,\beta^2}\beta^2, \\ c_Y &\approx c_{Y,\beta}\beta. \end{aligned} \quad (26.63)$$

For many applications except slow flying airplanes, the second-order and third-order term of  $c_L$  can be omitted.

As far as the torques are concerned, we introduce also dependencies on normalized angular rates

$${}^B\boldsymbol{\omega}_n = (p_n, q_n, r_n)^T = \left( \frac{pb}{2V_t}, \frac{qc}{2V_t}, \frac{rb}{2V_t} \right)^T. \quad (26.64)$$

A suitable approximation of the moment coefficients is now made as

$$\begin{aligned} c_L &\approx c_{L,0} + c_{L,\delta_a}\delta_a + c_{L,\beta}\beta + c_{L,p_n}p_n + c_{L,r_n}r_n, \\ c_M &\approx c_{M,0} + c_{M,\delta_c}\delta_c + c_{M,\alpha}\alpha + c_{M,q_n}q_n, \\ c_N &\approx c_{N,0} + c_{N,\delta_r}\delta_r + c_{N,\beta}\beta + c_{N,r_n}r_n. \end{aligned} \quad (26.65)$$

Finally, the propeller thrust force needs to be modeled. Using the advance ratio  $J = \frac{2\pi V_t}{\omega_p d}$ , with propeller diameter  $d$ , we can approximate the thrust coefficient

$$c_T \approx c_{T,0} + c_{T,J}J + c_{T,J^2}J^2. \quad (26.66)$$

The thrust is then obtained as

$$T = \rho \left( \frac{\omega_p}{2\pi} \right)^2 d^4 c_T. \quad (26.67)$$

### Linearized Dynamics

As common throughout literature, the linearized airplane dynamics are written using Euler angles, which is why we will follow the same approach. But conceptually, they could be written in a singularity-free form using a minimal quaternion perturbation.

Typically, a separation into *longitudinal* and *lateral* dynamics is made, in order to assess related characteristics separately. Furthermore, the state is transformed to contain  $\alpha$ ,  $\beta$ , and  $V_t$  rather than  ${}^B\mathbf{v}$ .

The linear dynamics around a reference state  $\mathbf{x}_0$  and input  $\mathbf{u}_0$  vector takes the form

$$\Delta \dot{\mathbf{x}}_{\text{lon}} = \mathbf{A}_{\text{lon}} \Delta \mathbf{x}_{\text{lon}} + \mathbf{B}_{\text{lon}} \Delta \mathbf{u}_{\text{lon}}$$

and

$$\Delta \dot{\mathbf{x}}_{\text{lat}} = \mathbf{A}_{\text{lat}} \Delta \mathbf{x}_{\text{lat}} + \mathbf{B}_{\text{lat}} \Delta \mathbf{u}_{\text{lat}}.$$

The following formulation follows [26.19] to a large extent.

Figure 26.21 describes the separation in terms of inputs  $\Delta \mathbf{u}$  and states  $\Delta \mathbf{x}$  for the linearized system.

The longitudinal nonlinear equations are given as

$$\begin{aligned} \dot{q} &= \frac{1}{I_{yy}} [M_A + M_T - (I_{xx} - I_{zz})pr + I_{xz}(p^2 - r^2)], \\ \dot{V}_t &= \frac{1}{m} [-D \cos \beta + Y \sin \beta \\ &\quad + T \cos(\alpha - \epsilon_T) \cos \beta + mg_1], \\ \dot{\alpha} &= \frac{1}{\cos \beta} \left[ \frac{1}{mV_t} (-L - T \sin(\alpha - \epsilon_T) + mg_3) + q_A \right], \\ \dot{\theta} &= q \cos \varphi - r \sin \varphi, \end{aligned} \quad (26.68)$$

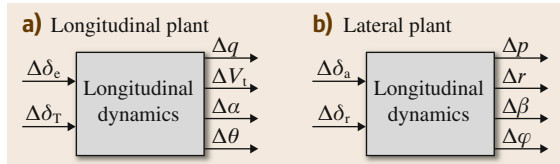


**Fig. 26.21a,b** Linearized (a) longitudinal, and (b) lateral plants for inputs  $\Delta \mathbf{u}$  (around  $\mathbf{u}_0$ ) of the local states  $\Delta \mathbf{x}$  (around  $\mathbf{x}_0$ )

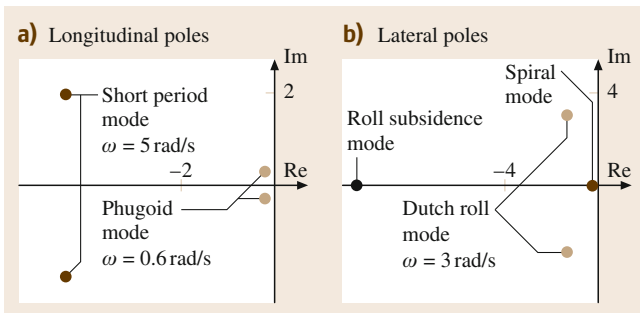


**Fig. 26.22** (a) Longitudinal, and (b) lateral poles of an example aerobatic RC airplane

and the lateral nonlinear equations amount to

$$\begin{aligned} \dot{p} &= \frac{I_{zz}(L_A + L_T - T_p)}{I_{xx}I_{zz} - I_{xz}^2} - \frac{I_{xz}(N_A + N_T - T_r)}{I_{xx}I_{zz} - I_{xz}^2}, \\ \dot{r} &= \frac{I_{xz}(L_A + L_T - T_p)}{I_{xx}I_{zz} - I_{xz}^2} + \frac{I_{zz}(N_A + N_T - T_r)}{I_{xx}I_{zz} - I_{xz}^2}, \\ \dot{\beta} &= -r_A + \frac{1}{mV_t} [Y \cos \beta + D \sin \beta \\ &\quad - T \cos(\alpha - \epsilon_t) \sin \beta + mg_2], \\ \dot{\varphi} &= p + q \sin \varphi \tan \theta + r \cos \varphi \tan \theta, \end{aligned} \quad (26.69)$$

where the following terms were used

$$\begin{aligned} g_1 &= g(-\cos \alpha \cos \beta \sin \theta + \sin \beta \sin \varphi \cos \theta \\ &\quad + \sin \alpha \cos \beta \cos \varphi \cos \theta), \\ g_2 &= g(\cos \alpha \sin \beta \sin \theta + \cos \beta \sin \varphi \cos \theta \\ &\quad - \sin \alpha \sin \beta \cos \varphi \cos \theta), \\ g_3 &= g(\sin \alpha \sin \theta + \cos \alpha \cos \varphi \cos \theta), \\ q_A &= q \cos \beta - p \sin \beta \cos \alpha - r \sin \alpha \sin \beta, \\ r_A &= r \cos \alpha - p \sin \alpha, \\ T_p &= (I_{zz} - I_{yy})qr + I_{xz}pq, \\ T_r &= (I_{yy} - I_{xx})qp - I_{xz}qr. \end{aligned} \quad (26.70)$$

The linearizations of (26.68) and (26.69) are straightforward to obtain and not provided here due to space constraints. For a specific operating point, typically stationary ( $\varphi_0 = 0$ ,  $\theta_0 = \alpha_0$ , and  ${}^B\boldsymbol{\omega} = \mathbf{0}$ ), the standard tools of linear systems analysis can be employed. Most importantly, the *pole* locations in the imaginary plane will tell the characteristic modes and their dynamic stability. Figure 26.22 shows a pole location plot for an example RC airplane and introduces the related mode names.

In the case of a real pole  $\pi_i$ , it has the time constant  $\tau_i = -1/\text{Re}(\pi_i)$ . In the case of a complex conjugate pole pair, it is associated with a damping ratio  $\zeta_i = -\text{Re}(\pi_i)/\sqrt{\text{Im}(\pi_i)^2 + \text{Re}(\pi_i)^2}$  and with an eigenfrequency  $\omega_i = \sqrt{\text{Im}(\pi_i)^2 + \text{Re}(\pi_i)^2}$ .

Figure 26.23 illustrates and characterizes the main modes.

#### 26.4.4 Design Guidelines

Airplane design typically consists of the three stages *conceptual* design, *preliminary* design, and *detail* design. Here, we focus on the first two phases; due to space constraints, details of airplane structural design

and analysis are not covered here. The reader is referred to respective literature, e.g., [26.20], or [26.21], the latter covering RC-type aircraft. In the following, we provide a quick overview of practical guidelines for the typically iterative design process related to achieving characteristics as described above. The guidelines follow largely [26.22] and [26.18], with focus on slow-flying small-scale UAS.

### Sizing and Geometry of Main Components

In the following, we provide some rules of thumb as initial guess for the design process in terms of sizing the wing, tail, control surfaces, and the propulsion unit. As a first and very general advice, the engineer is encouraged to minimize wetted area and cross section, as well as any kind of nacelles for increased aerodynamic efficiency.

**Wing.** First, an existing airfoil shall be chosen with characteristics meeting the requirements in the target flow regime (Re and Ma). When it comes to determining the overall wing size, a first estimate of design weight including structure, avionics, payload, propulsion unit, and energy storage is of crucial importance (26.2). With the target speed  $V_r$  and design lift coefficient  $c_l$ , a rough guess can be made for the wing area

$$A = 2mg / (\rho V_r^2 c_l) .$$

Concerning wing shape, clearly highest efficiency is reached with high aspect ratios (plus no multiple

lifting surfaces), and, at low Ma, no sweep-back – as long as still implementable with a structural concept and staying at reasonably high Re numbers. For high efficiency, it is advisable to achieve an elliptic lift distribution to some extent by geometry. For benign stalling characteristics, it is furthermore highly advisable to twist the wing leading edge downward with increased spanwise distance (which also influences the lift distribution).

Finally, some dihedral should be considered for roll stability.

**Tail.** Various types of tails and even *exotic* configurations like the canard have been suggested; here, we want to simply point out the importance of the so-called *tail volume coefficient*,  $c_{VT}$  and  $c_{HT}$  concerning vertical and horizontal tail, respectively,

$$c_{VT} = l_{VT} A_{VT} / (bA) , \quad (26.71)$$

$$c_{HT} = l_{HT} A_{HT} / (\bar{c}A) , \quad (26.72)$$

with the wing to vertical tail lever arm  $l_{VT}$  and the wing to horizontal tail  $l_{HT}$  (these are referenced to the individual mean 1/4-chord points). Typical values for small-size slow airplanes are  $c_{VT}=0.02-0.04$  and  $c_{HT} = 0.5-0.7$ . Furthermore, care should be taken that control surfaces are not completely blanketed in the case of stall (for stall/spin recovery).

**Control Surfaces.** Ailerons typically extend from around 50% in span direction to 90%; in this setting, 20–30% of wing chord is suggested as aileron depth. Tail control surface depth is typically chosen around 40% of the respective chord.

**Propulsion.** Finally, some advice is given concerning the propulsion unit. Some UAVs are required to be handlaunched: note that this imposes limits on the overall maximum take-off mass and minimum/stall airspeed. Experience shows that reasonable limits are  $<9$  m/s minimum/stall speed and 7 kg airplane mass. For such small UAVs, a static thrust to weight ratio of at least 50% is highly recommended. In general, the propulsion unit must be sized to meet the specifications in terms of climb rates, maximum level flight speed and service ceiling. For the highest efficiency, the propulsion unit should be designed such as to provide highest efficiency at the design operating point (subscript r)  $T_r/W = c_{D,r}/c_{L,r}$ . For a hobbyist brushless DC outrunner type motor, the maximum power per motor mass ratio of 3.4 kW/kg can be used for estimation of the propulsion unit weight [26.23] (gearbox and propeller mass not included).

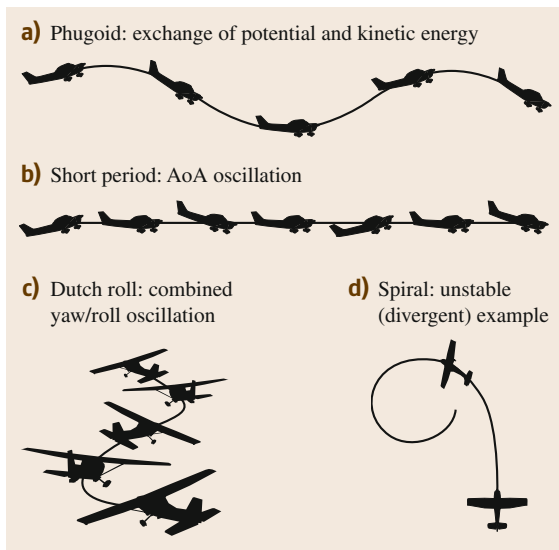


**Fig.26.23a-d** Characteristic trajectories of excited longitudinal modes (a,b) and lateral modes (c,d)



### Handling Qualities

Manned aviation introduced the notion of *handling qualities*, assessing how well an aircraft can be flown by a human pilot as a basis for certification of both civil and military airplanes. Since UAS typically rely on autopilot systems enabling a certain degree of autonomy, these concepts may not be directly applied, but are still extremely relevant. Most importantly, the handling qualities concerning static and dynamic stability, as well as controllability determine the success of a UAS design.

While an autopilot can handle more and faster instabilities than a pilot, it can certainly not compensate for missing actuation authority. As detailed in Sect. 26.7, it is advisable to implement de facto manual operation mode as a testing, backup, or even standard operation mode, in which the airplane is either steered manually or through some stability augmentation system (SAS). Therefore, it is highly advisable that the resulting system complies with the following core requirements (simplified from [26.18]):

- Static longitudinal stability: most aft COG at least 5% of  $\bar{c}$  in front of aerodynamic center (static margin, SM).
- Phugoid damping  $\zeta_{ph} > 0.2$ .
- Short-period oscillation  $\omega_{sh} > 2$ ,  $\zeta_s > 0.5$ .
- Spiral mode may be unstable, if  $\tau_{sp} > 20$  s.
- Roll acceleration at maximum aileron deflection  $|\dot{p}(\delta_{a,max})| > 5$  rad/s<sup>2</sup>, roll subsidence time constant  $\tau_{rs} < 1$  s.
- Dutch roll damping  $\zeta_{dr} > 0.1$ .
- Spins shall not be entered abruptly and must always be recoverable.

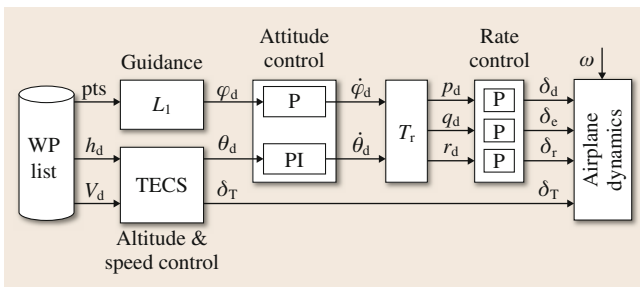


Fig. 26.24 Simple cascaded airplane guidance and control system

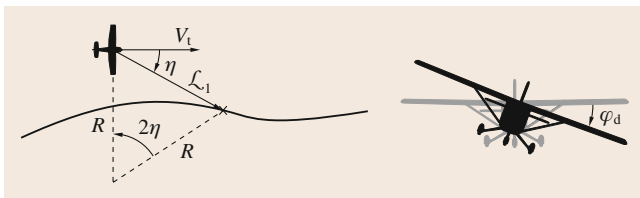


Fig. 26.25 Illustration of  $L_1$  lateral guidance

### 26.4.5 A Simple Autopilot

As shown earlier, airplane dynamics are nonlinear multiple-input-multiple-output (MIMO) systems with a significant amount of cross-coupling, thus they are inherently challenging to control. While a plethora of control strategies have been suggested as autopilots, we will provide a simple yet functional approach here that employs the popular concept of *cascaded* control loops as well as simple linear single-input-single-output (SISO) *PID* controllers acting on subparts of the dynamics. This approach is still widely deployed and well-understood, despite the fact that more advanced controllers, such as model-based linear quadratic regulators (LQR) with gain scheduling or nonlinear dynamic inversion (NDI) may achieve significantly better performance. Reference [26.24] constitutes an excellent reference for in-depth treatment of small UAS guidance and control with cascaded control loops.

#### Cascaded Control Architecture

Figure 26.24 introduces the overall controller architecture. It presents the (typical) separation of per-axis *rate controllers* at the innermost loop, followed by an *attitude* controller and a combined altitude and speed controller TECS (total energy control system), as well as by a lateral  $L_1$  guidance. In general, care must be taken to separate successively closed loops by around a decade in terms of bandwidth.

Assuming little cross-axis sensitivity, the rate controllers may be implemented with simple individual P-controllers, optionally with  $1/V_t^2$  gain scaling. Also the attitude controllers can be as simple as P and PI-controllers for roll and pitch, respectively. Note that the desired roll and pitch angle derivatives need to be transformed in the static block  $T_r$  into angular reference rates: this can be achieved by applying the inverse Jacobian  $J_r$  from (26.42) – where the missing yaw angle time derivative can be computed from the coordinated turn constraint  $\beta = 0$ ,  $\dot{\beta} = 0$  in (26.69)

$$\dot{\psi} = -\frac{g \sin \phi}{V_t \cos \alpha \cos \phi} + \frac{\dot{\theta}_d \sin \phi}{\cos \phi \cos \theta} \quad (26.73)$$

The combined altitude and speed controller (TECS) inspired from [26.25] uses the difference to the reference altitude  $\Delta h = h_d - h$  to compute a desired climb rate of the form  $\dot{h}_d = \dot{h}_{traj} + K_{P,alt} \Delta h$ , with the given trajectory rate of climb  $\dot{h}_{traj}$  and a *P*-gain  $K_{P,alt}$ . Knowing the speed and corresponding angle of attack,  $\dot{h}_d$  can be simply converted into a desired pitch angle  $\theta_d$  – to be saturated according to maximum thrust (climb) and drag (sink). Since climb rate must be provided via

additional thrust, the respective power component is computed as  $\Delta T_{\text{climb}} = mgh_d/V_t$ . Concerning the speed control, the second thrust component is computed with the  $P$ -gain  $K_{P,\text{vel}}$  as  $\Delta T_{\text{acc}} = mK_{P,\text{vel}}\Delta V_t$ .

As a last autopilot component, the  $\mathcal{L}_1$  lateral guidance [26.26] proceeds as follows (illustrated in Fig. 26.25): a reference circular path of radius  $R$  is calculated that intersects the reference path given by the waypoint sequence at look-ahead distance  $L_1$ . In or-

der to track this reference, a centripetal acceleration of  $V_t^2/R$  is needed, which can now be directly translated into a desired roll angle  $\varphi = \arctan(V_t^2/(Rg))$  corresponding to a coordinated (level) turn – saturated with maximum bank angles.

Note that the suggested scheme should be enhanced by stall prevention and recovery (AOA monitoring and control), as well as by preventing sideslip for safer (and more efficient) operation.

## 26.5 Rotorcraft Modeling and Design

Various types of rotorcraft UAS configurations have been developed in the past (some examples are shown in Fig. 26.26), from helicopter-type UAVs such as [26.27, 28], over a vast selection of multicopter configurations such as [26.29, 30] and tail-sitter vehicles such as [26.31, 32] up to completely new types of flight mechanisms [26.33, 34]. The design, modeling, and system analysis process for all these RW-UAS types is essentially very similar and is largely based on the methodologies originally developed within the aerospace community for full-scale rotorcraft design and evaluation [26.15, 35]. In this context, it is important to realize that the rotorcraft design process goes beyond mere efficiency and payload considerations focused on the propulsion components (e.g., using BEMT). Designing an effective RW-UAS should in principle also include flight dynamics assessments of the entire robotic flight platform.

Flight performance assessment is commonly based on one of two types of modeling approaches referred to as *quasi-steady* and *hybrid* [26.36]. The quasi-steady modeling method employs a single rigid body representation of the aircraft affected by the steady-state forces and moments originating from the propulsion subsystem. Hybrid models treat the rotorcraft as a multibody system where the dynamics of the aircraft body are coupled with additional dynamics of the rotor or propeller blades (e.g., blade flapping dynamics). For propeller-based RW-UAS like multicopter and tail-sitter vehicles using the quasi-steady approach to, e.g., model attitude dynamics is most widespread. This may be related to the fact that for these vehicle configurations, properly accounting for motor dynamics may be more relevant than accounting for high-order effects related to structural deformations of the propeller blades. For helicopter-type UAVs the hybrid approach is more common as some dynamic modes of the rotor system are likely to couple with the attitude dynamics of the main rotorcraft body. Note that a proper application of the hybrid approach is considerably more involved than using

quasi-steady models and should only be resorted to if justified.

A detailed treatment of the specific modeling and design procedures for every robotic rotorcraft configuration is beyond the scope of this chapter and thus the presented considerations focus on helicopter-type and multicopter UAVs. Based on the extensive theoretical aerospace-related background available in [26.14, 15, 35] amongst others, models for the most relevant rotor respectively propeller forces and moments are presented and subsequently appended to the rotorcraft body dynamics discussed in Sect. 26.3.6. A simplified

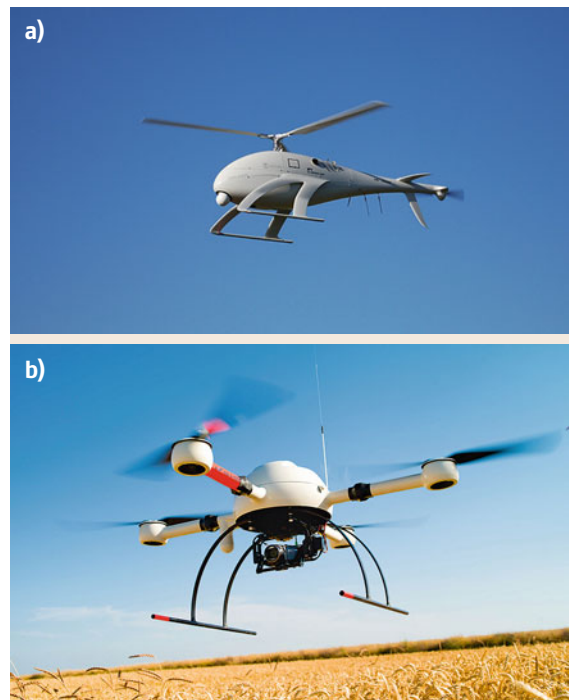


**Fig. 26.26** (a) Conventional helicopter configuration. Swiss UAV Neo S-300. (b) Quadcopter configuration. Microdrones MD4-1000

hybrid modeling approach is introduced and reductions to quasi-steady models are discussed where applicable. Finally, a few metrics meaningful for rotorcraft design and control purposes are discussed and summarized shortly.

### 26.5.1 Mechanical Design of Rotors and Propellers

The main control mechanism for any RW-UAS is its rotors or propellers. Accordingly, to understand the working principles and the dynamics of the rotorcraft type of aircraft, it is worth investigating a few of the main design characteristics found in these flying mechanisms.

The following discussion focuses on the operation principles of helicopter rotors and will be expanded to propellers subsequently. Figure 26.27 visualizes the typical rotor degrees of freedom realized via the *flap*, *lead-lag* and *feathering* (also referred to as *pitch*) hinges. The flap hinge allows the rotor blade to flap due to aerodynamic and inertial loads affecting the blade body during flight. The lead-lag hinge responds to lateral rotor blade moments due to Coriolis forces related to flapping. Where the flap and the lead-lag hinges are usually passive, possibly augmented with spring or damper elements, the pitch hinge is active in order to adjust the blade angle of attack and thus the generated aerodynamic forces.

Three types of rotor hubs are typically found in modern helicopters referred to as *teetering*, *articulated*, and *hingeless* depending on the mechanical realization of the flap hinge (Fig. 26.28). In the case of teetering rotor, a single hub flap hinge is located directly on the rotorshaft axis, rigidly connecting a set of two rotor blades. For the articulated rotor, the blades and the rotor hub are connected via mechanical hinges at a specific offset  $e$  from the rotor shaft axis, thus allowing each blade to flap individually. The hingeless rotor flaps through the deformation of elastic elements

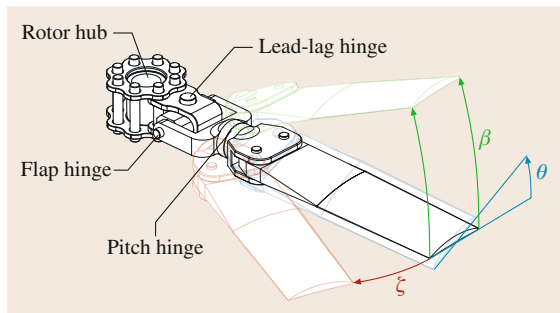


**Fig. 26.27** Typical hinge configuration of an articulated rotor blade

connecting the hub with each individual rotor blade or directly through structural deformation of the blades themselves. In this case, a virtual hinge offset can be defined at the intersection of the rotor hub plane and the tangent to the deflecting blade body at 75% of the rotor radius [26.14]. The specific characteristics of the flap hinge (offset from rotor shaft, stiffness, and damping) are fundamental for rotor blade flapping and in consequence for the rotorcraft pitch and roll dynamics as discussed later.

In the case of most propeller-based rotary-wing (RW) UAVs (e.g., multicopter systems) the feathering and lead-lag degrees of freedom do not exist. Nevertheless, propeller-based RW-UAVs may exert blade flapping by deformation of the propeller blades.

### 26.5.2 Rotorcraft Dynamics

As discussed in Sect. 26.3.6, the main rotorcraft body dynamics can be directly described by the simplified differential (26.45) which for most rotorcraft systems maintain the presented mathematical structure. For helicopter-type and multicopter UAV configurations the dominant set of external forces and moments affecting these dynamics can be summarized as

$$\mathbf{F} = \mathbf{F}_G + \sum_{i=1}^{N_r} \mathbf{F}_T^i + \sum_{i=1}^{N_r} \mathbf{F}_H^i + \mathbf{F}_D, \quad (26.74)$$

$$\boldsymbol{\tau} = \sum_{i=1}^{N_r} \boldsymbol{\tau}_Q^i + \sum_{i=1}^{N_r} \boldsymbol{\tau}_T^i + \sum_{i=1}^{N_r} \boldsymbol{\tau}_H^i + \sum_{i=1}^{N_r} \boldsymbol{\tau}_\beta^i. \quad (26.75)$$

The vector  $\mathbf{F}_G$  represents the weight force and  $\mathbf{F}_T^i$  is the thrust force of the  $i$ -th rotor or propeller out of the total set of  $N_r$  rotors or propellers (Fig. 26.29). These forces are related to the body heave dynamics but due

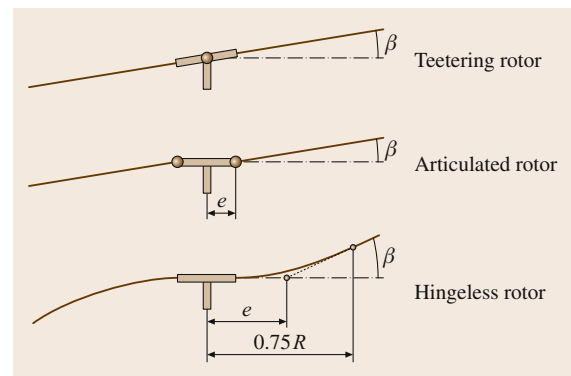


**Fig. 26.28** Rotor hub design concepts of a teetering rotor, an articulated rotor with hinge offset  $e$  and a hingeless rotor with a virtual hinge offset  $e$

to the underactuation of most rotorcraft are also responsible for the lateral rotorcraft acceleration.

The additional in-plane hub forces  $F_H^i$  represent drag-related effects that may be neglected near hover but become more dominant for higher lateral flight velocities [26.15]. The vector  $F_D$  represents the drag force associated with the rotorcraft main body. For simplicity's sake, it is assumed that the center of pressure of the rotorcraft body is collocated with its center of gravity which is not necessarily the case.

The relevant set of external moments is defined by the torques  $\tau_Q^i$  affecting the vehicle yaw dynamics, the thrust-induced moments  $\tau_T^i$ , the moments introduced by the hub forces  $\tau_H^i$  and the flapping moments related to the rotor hub stiffness  $\tau_\beta^i$ .

More explicit expressions for the respective force and moment terms may be found in Tables 26.6 and 26.7, where  $T_i$  is the averaged thrust force magnitude,  $H_x^i$  and  $H_y^i$  are the hub force components along the rotorcraft body frame  $x$ - and  $y$ -axes, and  $Q_i$  is the torque generated by the  $i$ -th propeller or rotor. The aerodynamic drag of the main rotorcraft body, represented by the components  $D_x$ ,  $D_y$ , and  $D_z$ , has been discussed in some detail in Sect. 26.3.5.

The vector  ${}^B r_i$  corresponds to the displacement of the  $i$ -th rotor or propeller hub from the rotorcraft body frame origin and  ${}^B n_i$  is the tip-path plane normal of the  $i$ -th propeller or rotor disk as explained in [26.37].

The coefficients  $\beta_{1c}$  and  $\beta_{1s}$  represent the longitudinal and lateral flapping coefficients [26.15] describing the tilting of the rotor or propeller disk as elaborated in more detail later in this section. Finally, the parameter  $k_b^i$  corresponds to the flapping spring stiffness of the  $i$ -th rotor or propeller hub. In the case of articulated or teetering hubs this torsional spring stiffness represents potential flap hinge springs and in case of hingeless hubs approximates

**Table 26.6** Typical rotorcraft forces

Type of force	Expression
Gravity	${}^B F_G = {}^B R_W \begin{pmatrix} 0 \\ 0 \\ -mg \end{pmatrix}$
Thrust	${}^B F_T^i = {}^B n_i T_i$
Hub forces	${}^B F_H^i = \begin{pmatrix} H_x^i \\ H_y^i \\ 0 \end{pmatrix}$
Rotorcraft body drag	${}^B F_D = \begin{pmatrix} D_x \\ D_y \\ D_z \end{pmatrix}$

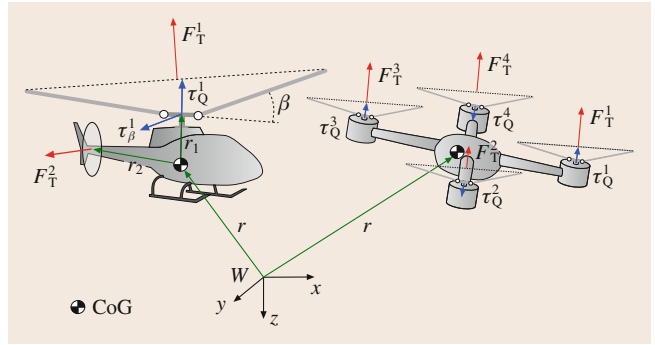


**Fig. 26.29** A conventional helicopter and a quadro-copter platform. Flapping angles have been exaggerated and only the rotor and propeller forces relevant near hover have been visualized

the structural bending stiffness of a particular rotor or propeller.

In the case of a helicopter tail rotor, flapping is usually neglected and the thrust direction is modeled as, e.g.,

$${}^B n_i = \begin{pmatrix} 0 \\ 1 \\ 0 \end{pmatrix}. \quad (26.76)$$

To finalize the models of these external forces and moments, the respective aerodynamic effects as well as the role and characteristics of blade flapping must be discussed next.

### 26.5.3 Simplified Aerodynamics

In order to accurately predict the forces and moments generated by a rotorcraft system, accounting for various ranges of operation conditions, detailed design specifications, aerodynamic interactions between the different rotors or propellers and possibly the rotorcraft body itself, highly sophisticated aerodynamics simula-

**Table 26.7** Typical rotorcraft moments

Type of moment	Expression
Torque	${}^B \tau_Q^i = \begin{pmatrix} 0 \\ 0 \\ Q_i \end{pmatrix}$
Thrust moment	${}^B \tau_T = {}^B r^i \times {}^B f_T^i$
Hub moment	${}^B \tau_H^i = {}^B r^i \times {}^B f_H^i$
Flap moment	${}^B \tau_\beta^i = k_b^i \begin{pmatrix} -\beta_{1s}^i \\ \beta_{1c}^i \\ 0 \end{pmatrix}$

tion tools are required. Such tools are usually not easily accessible to or operated by the roboticist and may hide some of the fundamental flight dynamics characteristics of a particular platform due to the involved complexity. For a repeated evaluation of the general flight properties of a rotorcraft it may thus be preferable to derive approximate, analytical models of the aerodynamic forces and moments. This may provide profound insight into the core working principles of rotorcraft operation.

The general approach to derive such models is the employment of BET as partially presented in Sect. 26.3.4. BET, as opposed to BEMT or MT, maintains the notion of individual rotor or propeller blades. Hence, it may account for changes in the angle of attack  $\alpha$ , the aerodynamic inflow velocities  $U_T$  and  $U_P$  and in consequence of the local lift and drag increments  $dL$  and  $dD$ , not only in function of the radial position  $r$  of the observed airfoil segment but also in dependency of the blade azimuth  $\xi$ . To further the understanding of this dependency in  $\xi$ , one may examine Fig. 26.16 as well as Fig. 26.30 where the hub coordinate frame  $H$  is introduced.

The perpendicular and tangential inflow velocities  $U_P$  and  $U_T$  (and thus also  $\alpha$ ) are strongly related to the rotor angular speed  $\Omega$  and the induced inflow velocity  $v_i$  (as discussed for BEMT). In flight operation beyond hover, these inflow velocities are also affected by the rotorcraft linear and angular velocities  ${}^B v$  and  ${}^B \omega$ , as well as the potential flapping motion of the rotor or propeller blades. From the perspective of a revolving rotor or propeller blade, these additional inflow velocities vary periodically in function of  $\xi$ .

Inspecting Fig. 26.30, one can establish the following relations for the airfoil inflow velocities [26.35]

$$U_T = \Omega(e+r) - v_y + \beta \omega_x r, \quad (26.77)$$

$$U_P = v_i - w + \omega_y(e+r) + \dot{\beta}r - \beta v_x. \quad (26.78)$$

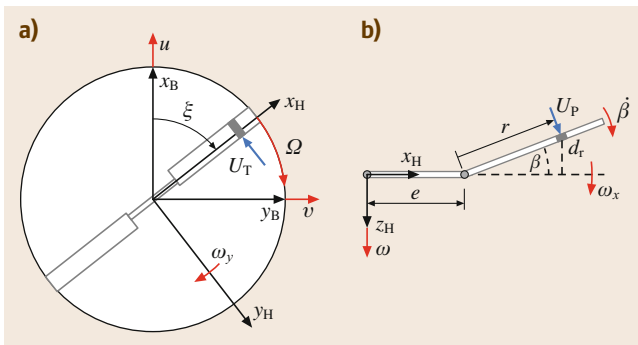


**Fig. 26.30** (a) Top view of revolving rotor/propeller blade and the relevant velocities. (b) Side view of revolving rotor/propeller blade and the relevant velocities

The linear and angular velocities  $v_x$ ,  $v_y$ ,  $\omega_x$ , and  $\omega_y$  correspond to the projections of the vehicle body velocities  $u$ ,  $v$ ,  $p$ , and  $q$  into the hub frame  $H$

$$v_x = u \cos \xi + v \sin \xi, \quad (26.79)$$

$$v_y = v \cos \xi - u \sin \xi, \quad (26.80)$$

$$\omega_x = p \cos \xi + q \sin \xi, \quad (26.81)$$

$$\omega_y = q \cos \xi - p \sin \xi. \quad (26.82)$$

For helicopter-type UAVs the azimuth dependency of  $\alpha$  may also be related to periodic changes in the blade pitch angle  $\theta$ . For helicopter configurations the feathering angle  $\theta$  can usually be controlled collectively for the entire rotor disk or cyclically in dependency of the blade position  $\xi$  using a swashplate mechanism [26.38]

$$\theta = \theta_0 + \theta_{1c} \cos \xi + \theta_{1s} \sin \xi. \quad (26.83)$$

The swashplate mechanism essentially provides the means to adjust the collective pitch angle  $\theta_0$  as well as the cyclic pitch angles  $\theta_{1c}$  and  $\theta_{1s}$  individually. Note that for twisted propeller or rotor blades  $\theta_0$  merely represents the pitch angle at the blade root and an additional term accounting for the radial variation in pitch must be introduced [26.14].

By altering  $\theta_0$ , the swashplate provides some control over the average angle of attack of the entire rotor disk and thus the generated average thrust and torque. Similarly, varying the cyclic components creates a lift imbalance between opposing sides of the rotor disc. This lift imbalance induces a periodic flapping motion of the individual rotor blades (also depending on  $\xi$ ) which affects the pitch and roll moments  $\tau_\beta$  and  $\tau_T$ . For helicopter-type UAVs this is the main control mechanism for the pitch and roll attitude dynamics.

For the majority of multicopter vehicles  $\theta_0$  is usually fixed and the cyclic angles do not exist ( $\theta_{1c} = \theta_{1s} = 0$ ). In this case, attitude control is realized through  $\tau_T$  only by changing the propeller speed  $\Omega_i$  of the individual propellers.

To describe the aforementioned periodic changes in blade flapping the following representation of the flapping angle  $\beta$  is customary when modeling rotorcraft dynamics [26.39]

$$\beta = \beta_0(t) + \beta_{1c}(t) \cos \xi(t) + \beta_{1s}(t) \sin \xi(t). \quad (26.84)$$

The coefficient  $\beta_0(t)$  corresponds to the coning angle of the entire rotor or propeller disc, whereas  $\beta_{1c}(t)$  and  $\beta_{1s}(t)$  are the longitudinal and lateral disk tilting angles.



Unlike the blade pitch coefficients in (26.83), the flap coefficients in (26.84) are assumed to be functions of time  $t$  which is later exploited when modeling flapping dynamics.

Although it is crucial to capture all these periodic dependencies in  $\xi$ , it can be obstructive for the purpose of creating an efficient rotorcraft simulation. Directly simulating the body dynamics (26.45) under the influence of the external forces and moments (26.74) and (26.75) while accounting for all dependencies in  $\xi$ , would require the blade motion to be simulated step by step while moving around the rotor or propeller shaft. This can lead to comparatively stiff differential equations which may be hard to simulate efficiently.

An alternative approach is to derive simplified force and torque models by integrating the lift and drag increments along the rotor or propeller radius, summing over the number of blades  $N_b$  and averaging around the rotor azimuth as

$$T = \frac{N_b}{2\pi} \int_0^{2\pi} \int_0^R dL, \quad (26.85)$$

$$Q = \frac{N_b}{2\pi} \int_0^{2\pi} \int_0^R r \left( dD + \frac{U_P}{U_T} dL \right), \quad (26.86)$$

$$H_x = \frac{N_b}{2\pi} \int_0^{2\pi} \int_0^R \sin \xi \left( dD + \frac{U_P}{U_T} dL \right), \quad (26.87)$$

$$H_y = \frac{N_b}{2\pi} \int_0^{2\pi} \int_0^R \cos \xi \left( dD + \frac{U_P}{U_T} dL \right). \quad (26.88)$$

Combining (26.77) to (26.88) with (26.12), (26.13), (26.27), and (26.33) and assuming simple rotor or propeller blade geometries (e.g., linear blade twist) the above expressions can be evaluated algebraically, e.g., using a symbolic computation program. As opposed to BEMT these averaged aerodynamic formulations are capable of accounting for the effects of the periodic changes of inflow velocities such as, e.g., the *dissymmetry of lift* phenomenon [26.15] as well as for the varying blade feathering and flapping angles.

To gain some appreciation of how these averaged models may be useful in providing insight into the core characteristics of rotorcraft operation, a strongly simplified thrust model directly resulting from (26.85) under the assumption of hover and negligible flapping angles is given as an example

$$T = \left( k_{T1} \theta_0 + k_{T2} \frac{v_0}{\Omega} + k_{T3} \right) \Omega^2. \quad (26.89)$$

The coefficients  $k_{T1}$ ,  $k_{T2}$ , and  $k_{T3}$  essentially depend on aerodynamic and geometric rotor or propeller properties. As one may deduce directly from (26.89), thrust is a linear function of the collective pitch angle  $\theta_0$  and the average induced rotor or propeller inflow velocity  $v_0$  which is further defined in the next section.

### 26.5.4 Nonuniform Inflow

In order to account for the varying induced flow field over the rotor or propeller disk in hover and forward flight, the following approximate induced inflow distribution may be assumed as discussed in [26.14]

$$v_i = v_0 + \frac{r}{R} (v_{1c} \cos \xi + v_{1s} \sin \xi). \quad (26.90)$$

The velocity component  $v_0$  represents the average induced inflow at the center of the modeled rotor respectively propeller disc. It is directly related to the thrust level the rotor or propeller is operating at and may be computed, e.g., based on the iterative method discussed in [26.15]. The inflow coefficients  $v_{1c}$  and  $v_{1s}$  account for changes in the induced flow field due to lateral rotorcraft flight velocities. Various steady-state models for  $v_{1c}$  and  $v_{1s}$  have been proposed in the past with moderate prediction quality only.

Reference [26.40] presents these models in detail and discusses an alternative method which also accounts for transient effects. Accounting for inflow dynamics, the transient response of  $v_0$ ,  $v_{1c}$ , and  $v_{1s}$  to, e.g., sudden blade pitch changes can be captured and the aforementioned iterative computations may be avoided.

### 26.5.5 Flapping Dynamics

The dynamics of rotor or propeller flapping corresponds to a second-order differential equation of the flapping angle  $\beta$  which essentially represents an aerodynamically damped oscillator [26.35]

$$\ddot{\beta} = \check{\beta}(\xi, \Omega, u, v, w, p, q, \dot{p}, \dot{q}, \beta, \dot{\beta}, \theta). \quad (26.91)$$

Reference [26.41] and references therein elaborate the modeling process required to derive the above differential equation from first principles.

As for the simplified aerodynamic forces and moments, the dependency of (26.91) on rotor azimuth is important but problematic for efficient blade flap simulations. Here, the averaging operation discussed in [26.39] has been employed. This essentially leads to the following differential equation of the flapping coef-

ficients  $\beta_0$ ,  $\beta_{1c}$  and  $\beta_{1s}$

$$A_{\ddot{\beta}}\ddot{\beta} + A_{\dot{\beta}}\dot{\beta} + A_{\beta}\beta = A_{\theta}\theta + A_{\omega}\omega + A_{\nu}\nu, \quad (26.92)$$

$$\beta = \begin{pmatrix} \beta_0 \\ \beta_{1c} \\ \beta_{1s} \end{pmatrix}, \quad \nu = \begin{pmatrix} v_0 - w \\ v_{1c} \\ v_{1s} \end{pmatrix},$$

$$\omega = \begin{pmatrix} p \\ q \\ \dot{p} \\ \dot{q} \end{pmatrix}, \quad \theta = \begin{pmatrix} \theta_0 \\ \theta_{1c} \\ \theta_{1s} \end{pmatrix}.$$

The involved matrices from  $A_{\ddot{\beta}}$  to  $A_{\nu}$  depend on an abundance of aerodynamic, geometric, inertial, and structural parameters of the modeled rotor or propeller system as well as on the lateral flight velocity of the rotorcraft. The structure of these matrices is thus strongly related to the type of rotor or propeller hub that is being modeled. From the resulting mathematical relations it is for example possible to conclude that for a teetering rotor without hinge springs, the maximal flapping response  $\beta$  to a cyclic pitch input in  $\theta$  will follow with a  $90^\circ$  phase shift in rotor azimuth [26.15].

Considering the body time constants of most rotorcraft configurations in comparison with the time constants of the above dynamics, one may in general assume that the fast poles in (26.92) are negligible and they mostly represent rotor or propeller vibrations. Accordingly, (26.92) is often reduced to a first-order differential equation by introducing the assumption  $\ddot{\beta} = \mathbf{0}$ . For very rigid rotors or propellers one may even assume  $\dot{\beta} = \mathbf{0}$  and compute the steady-state flapping response only (quasi-steady model). However, this is not the case for all RW-UAS configurations. To what degree higher order effects such as flapping or inflow dynamics have to be accounted for, depends on the level of frequency separation between the body poles versus the poles of the rotor dynamics.

### 26.5.6 Flight Dynamics Assessment

Assembling the dynamics of the rotorcraft body with the forces and moments defined in the previous section, as well as possibly introducing higher order effects such as blade flapping and inflow dynamics, results in a set of nonlinear differential equations representing the flight characteristics of the modeled platform. In order to inspect these flight characteristics one may

implement a flight simulator based on this set of nonlinear differential equations and analyze the simulated flight responses. The linearization process presented in Sect. 26.3.6 may provide additional conclusions and is often followed by a separation into subsystems analyzed individually.

One of the most crucial rotorcraft subsystems corresponds to the pitch and roll attitude dynamics as it is this subsystem which ultimately defines how agile, stable, or accurate a rotorcraft may be able to fly in the horizontal plane of motion. Assuming near hover operation and neglecting higher order dynamics, the linearized open-loop roll dynamics for example, can usually be reduced to a first-order transfer function

$$G(s) = \frac{P(s)}{U(s)} = \frac{K_p}{s - D_p}. \quad (26.93)$$

The frequency function  $P(s)$  represents the Laplace transform of the rotorcraft roll rate  $p$  and  $U(s)$  the Laplace transform of a control input affecting the roll subsystem. For a helicopter, this control input commonly corresponds to a cyclic swashplate command and for a quadro-copter to the differential speed between two propellers on opposing sides of its airframe. The abstracted system parameter  $K_p$  corresponds to the so-called *roll control derivative* and  $D_p$  to the so-called *roll damping* [26.37]. The control sensitivity  $K_p$  defines how strong the initial rotorcraft roll acceleration  $\dot{p}$  will respond to a control input represented by  $U(s)$ . The parameter  $D_p$  defines how well the system's dynamic response will be damped in the following. For hybrid rotorcraft models the corresponding transfer functions are generally of higher order but are equally useful when analyzed with the well-known tools of linear system theory [26.15, 35].

In general, these transfer functions and the resulting metrics such as, e.g.,  $K_p$  and  $D_p$  can be derived in dependency of a specific subset of physical rotorcraft parameters. Using these simple metrics and including the knowledge that may be gathered from the nonlinear flight simulator, flight performance trends can be assessed depending on the parameters of the UAV configuration under investigation. Such parameters may for example include the body pitch and roll inertia, the location of the body center of gravity or the location of the rotors or propellers. The fundamental understanding gained in this evaluation process is crucial for the development of effective robotic flight systems and the required control laws.

## 26.6 Flapping Wing Modeling and Design

A variety of animals, from insects to birds, are capable of flight maneuvers which are presently impossible in micro aerial vehicles, such as flying in turbulence or cluttered airspace. Additionally, animals are more maneuverable and can fly longer distances. People have made many attempts at building flapping robots or ornithopters. While several are successful, many either never take off or fly only for a short duration due to their higher complexity or poor design. Until recently, ornithopters represented a niche of flying vehicles. The development of lithium polymer batteries produced a light-weight high-power energy resource to power ornithopters. Among the first successful electric ornithopters were the Caltech and Aerovironment microbats in 1998 [26.42, 43]. Many designs still fail to fly despite the rapidly increasing population building electric ornithopters. A major problem in most designs is an inability to generate enough lift to take off in the first place. This precludes additional flight research, such as maneuverability, flight distance or time. Engineers have believed that flapping wings are essential to further development of micro aerial vehicles since the first electric ornithopters took off and biologists started to understand the aerodynamics of flapping insect wings. The main reason behind this focus is the idea that they are aerodynamically more efficient at the small Reynolds number of insects (10–10 000) when viscosity effects start to dominate airflow.

### 26.6.1 Aerodynamic Mechanisms

Our understanding of insect aerodynamics provides us with the most detailed model of the aerodynamic function of a flapping wing [26.45]. There is some evidence that wing flexibility can improve aerodynamic performance of a flapping wing by roughly 10% [26.46] if the angle of attack is not optimized for a stiff wing. However, a parametric study using a robot model of an insect wing suggests that wing flexibility does not improve performance if we can optimize angle of attack independently of wing stiffness [26.47]. Ignoring aeroelastic effects that change angle of attack distribution, the key known aerodynamic mechanisms of a flapping wing are [26.45]:

1. A stable leading edge vortex (LEV) that enables the wing to operate at high angles of attack without stall during the quasi-steady mid-stroke phase (Fig. 26.31). During stroke reversal the aerodynamics is not quasi steady. In this phase, five additional effects are thought to be important:

2. *Added mass* effects due to fluid acceleration in response to the reversal.
3. The Wagner effect explaining that changes in vortex strength need time to build-up over a few chord lengths of travel.
4. Rotational lift due to the timing of changes in angle of attack during stroke reversal and its effect on vortex lift through the *Kramer effect*.
5. Wake capture when the wing reverses direction and interacts with the momentum jet of its shed wake.
6. Clap and fling when the wings become close enough to (nearly) touch and air is forced out of the cavity formed by the two wings and sucked back in, which can increase lift [26.48].

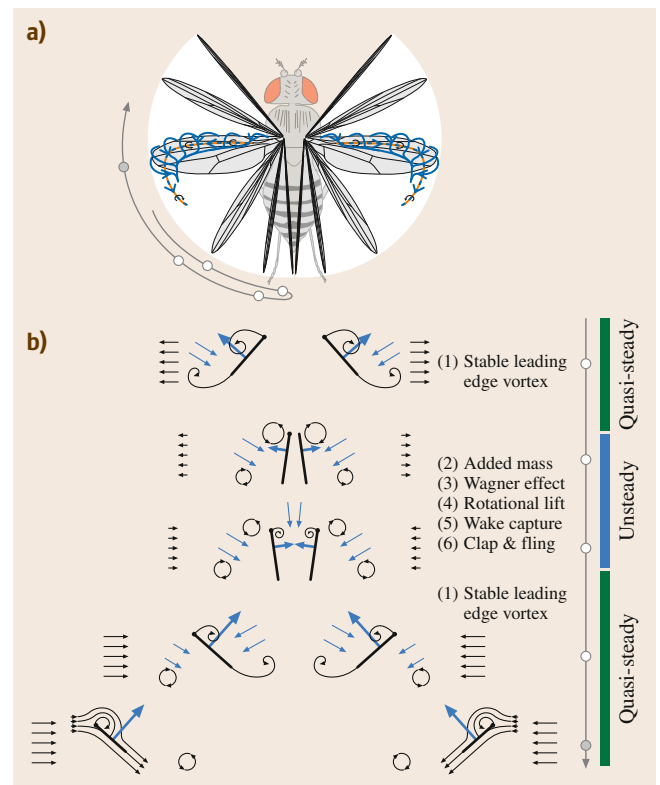


**Fig. 26.31a,b** Flapping insect wing aerodynamics can be understood through the interaction of a myriad of complex aerodynamic mechanisms. **(a)** The key high-lift mechanism insects employ, is a stable leading edge vortex (LEV) generated during the up and downstroke. **(b)** A flapping cycle consists of a quasi-steady part during which the wing accelerates little. During this phase, the stable LEV is the key high-lift mechanism (1). During stroke reversal there is evidence that up to five effects (2)–(6) could be important (after [26.44])

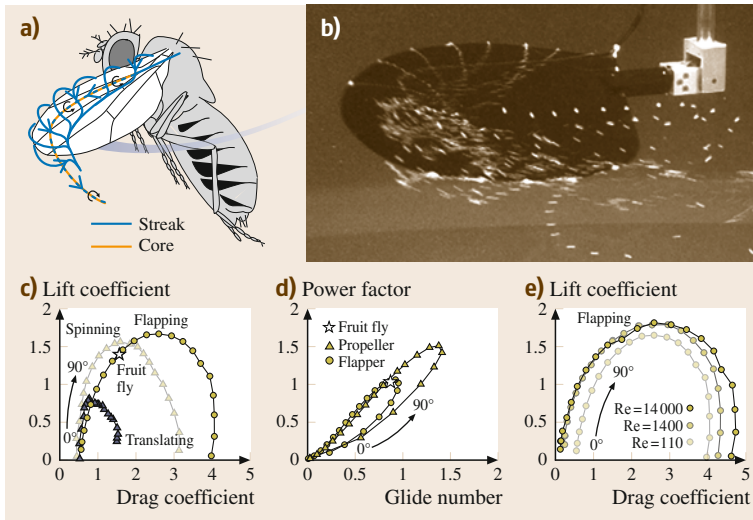


**Fig.26.32a–e** The aerodynamics of a flapping (insect) wing scale from insect to bird scale. **(a)** A stable LEV enables flapping wings to operate at high angles of attack without stall. **(b)** The key parameter explaining LEV stability is the wing's swing, its spinning motion, as demonstrated by this spinning model of a fly wing which generates a stable LEV and similarly elevated forces as in flapping wings. **(c)** At insect scale fixed (translating) wings underperform, whereas flapping and spinning wings generate similarly high lift. Spinning wings generate less drag which makes them more efficient. **(d)** The power factor of a spinning wing is higher than for a flapping wing, higher indicating that less power is needed to support body weight. **(e)** The dimensionless lift and drag averaged over a full flapping cycle is independent of scale to within good approximation (Reynolds number 110: fruit fly; 1400; house fly; 14 000; hummingbird). This makes flapping wing aerodynamics scalable enabling the use of dimensional analysis [26.49]

There exist, however no quantitative experimental studies or theories that fully dissect these effects and quantify their relative importance for aerodynamic lift and power. While flapping wing aerodynamics is complex and not fully understood, it is simple from a robot design perspective, because it is scalable from insect to bird size (Fig. 26.32). This enables prototyping at larger, more cost effective, scales and enables scaling the design down as technology advances, and smaller components and fabrication methods become

available [26.49]. Flapping wings generate more lift than translating wings because they generate a stable LEV. To generate a stable vortex over the whole wing, the aspect ratio with respect to the center of rotation needs to be equal to or smaller than about 4 [26.53]. Flapping wings with an aspect ratio larger than 4 can stall outboard [26.53]; whereas more stubby flapping wings cannot. This can explain why the majority of insect, bird, and bat wings have an aspect ratio of around 2–4 with respect to the *shoulder* joint [26.53]. The

	<b>a)</b>	<b>b)</b>	<b>c)</b>
Wingspan (cm)	28	16	3
Mass (g)	16	19	0.06
$m/m_0$	1.26	1.37	N/A (tethered)
Flight time	15 min.	11 min.	N/A (tethered)
Frequency (Hz)	14	30	110
Mechanism	Gearbox and 4-bar	Gearbox and string rollers	Piezo-electric Elastic 4-bar like
Scale (mm)	$10^2$ – $10^0$	$10^2$ – $10^0$	$10^2$ – $10^{-1}$
Power	1.4 W	3.27 W	N/A (tethered)
Current	380 mA	880 mA	N/A (tethered)

**Fig.26.33a–c** Examples of three different types of successful flappers. **(a)** Jaap Oldenkamp, Delfly II (after [26.49, 50]), **(b)** Nano Hummingbird (after [26.51]), **(c)** RoboBee (after [26.52])

main advantage of stubby wings is that they do not stall at high angles of attack enabling animals to take-off and land vertically by increasing angle of attack instead of flapping frequency [26.53] using LEVs [26.54]. Insects [26.55], bats, hummingbirds [26.56], and other birds [26.57], but also auto rotating seeds generate stable LEVs. This shows that stable LEVs are a convergent evolutionary solution for high lift at high angle of attack in nature [26.53].

Comparison of flapping versus spinning (propeller-like) insect wings shows spinning insect wings generate similar elevated lift forces by generating a LEV at lower drag. Helicopters with stubby rotors are, therefore, aerodynamically more efficient than stubby flapping wings, because they need less power to fly, as qualitatively presented in Fig. 26.32d [26.49]. This is confirmed experimentally for the most advanced hovering ornithopter at present, the Nano Hummingbird [26.51]. Comparing its flapping wing with a spinning wing showed for various forward speeds that flapping wings require more power for the same lift, in part due to aerodynamics [26.49, 53], and in part due to inertia losses [26.49, 51]. The key advantage of flapping wings seems to be the potential for extreme maneuverability and robustness. For instance, flapping wings may fare better in turbulence, close to the ground, near vertical surfaces and through clutter, when helicopters can become unstable due to stall and complex rotor-wake interactions [26.58].

## 26.6.2 Sizing New Flappers

An improved understanding of the detailed aerodynamics is scientifically invaluable, but perhaps not critical for designing successful ornithopters at a time when most struggle to take-off. Instead, sizing an ornithopter in terms of gross design parameters such as wing span, weight, and flapping frequency is more critical for take-off. The design methodology introduced here explains how one can transform successful designs to meet other mission perspectives. These designs can then enable flight studies that can advance our understanding of ornithopters versus Ro-UAS and FW-UAS to better appreciate their unique advantages.

Amongst successful flappers, there are three main archetypes as shown in Fig. 26.33. Historically, most flappers have relied on variants of a four-bar mechanism to generate the flapping motion which generates lift. One example of this is the Delfly family of ornithopters, which are capable of both fast forward flying and hover using this approach (VIDEO 493). A recent design which demonstrates both prolonged hovering flight and maneuverability, although lacks the ability to fly fast forward, is the Aerovirement

Nano-Hummingbird [26.51]. The Nano-Hummingbird uses a flapping mechanism composed of rollers and strings, while still using a geared down motor to provide power at the right frequency. Additionally, the wings provide control, rather than traditional tail control surfaces. Another more modern development is centimeter scale ornithopters which use piezoelectric actuators to generate flapping motion and control such as the Harvard Robobee [26.52] and the Berkeley Micromechanical Flying Insect. These are capable of tethered flight only, because no batteries exist that can supply high enough power in an enough lightweight package.

Despite the differences in design, these flappers share common trends in parameters, as shown in Fig. 26.34. To design a functional ornithopter, we start with a desired mission such as surveillance, search and rescue, or military applications. The mission determines an appropriate wingspan, and also determines a minimum time for task completion. Figure 26.34 shows that empty weight (mass without battery) follows an exponential pattern with wingspan, especially over the mid-range of wingspans. The main observation is that the power defining scale is not 3, but approximately 1.5. This may be because significant portions of the mass of smaller ornithopters comes from electronics, gearboxes and actuators, whose masses are not dependent on wingspan. Additionally, required flapping frequency decreases with wingspan, enabling an approximation of required flapping frequency based on wingspan that works well for all sizes of ornithopters, as expected using scaling relations.

Using initial design parameters from a successful ornithopter, we can design another ornithopter that is also capable of flapping flight using scaling relationships of geometry, fluid mechanics, and battery physics [26.27]. We need to decide on design parameters for the new flapper, including the wingspan  $b$ , weight  $W$ , aspect ratio  $\Lambda$ , and battery weight  $W_{\text{batt}}$ . Here, the aspect ratio is wingspan divided by chord length, as these are both easily measured design parameters. Example of initial parameters for the Delfly II are:  $b_1 = 28$  cm,  $m_1 = 16$  g ( $W = \text{mg}$ ),  $\Lambda_1 = 3.5$ ,  $f_1 = 14$  Hz,  $P_1 = 1.4$  W,  $W_{\text{batt},1} = 2.7$  g,  $t_1 = 15$  min. Initial design parameters are denoted with subscript 1; while new design parameters are denoted with subscript 2. Using the curve fitted through successful ornithopters as shown in Fig. 26.34, one can make an initial approximation of empty weight. First, we can calculate the wing area,  $A_{\text{fl}}$ , of the new flapper and the old flapper using the same equation for each

$$A \propto \frac{b^2}{\Lambda}. \quad (26.94)$$



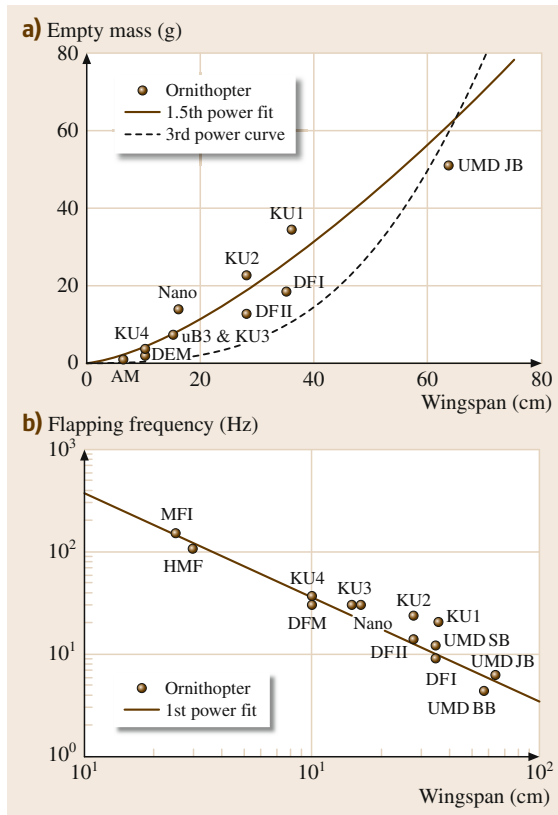


**Fig.26.34a,b** Current ornithopter trends of empty mass and flapping frequency with changes in wingspan. **(a)** The empty mass of successful ornithopters does not scale with wingspan cubed, but with wingspan to the power 1.5 ( $R^2 = 0.79$ ). The power law predicts the approximate masses effectively in the 10–50 cm wingspan range, while it overestimates the mass for those with wingspans below 10 cm. The curve to the third power consistently underestimates the unloaded masses of current ornithopters. **(b)** To support the weight of the ornithopter, flapping frequency needs to increase inverse to wingspan for smaller wingspans. Ornithopters in **(a)** fly freely and have a flight time of at least one minute. The Micromechanical Flying Insect and Harvard Robobee follow the same trend line for flapping frequency as larger ornithopters; even though they fly tethered (they would need to flap faster with batteries onboard). The relationship here fits a power curve with the exponent equal to  $-1.01$  with  $R^2 = 0.96$ . Abbreviations are as follows: MFI – Berkeley Micromechanical Flying Insect; HMF – Harvard Robobee; KU1,2,3,4 – Konkuk University ornithopters; DFI,II,M-Delfly I,II and Micro; Nano – Aerovironment Nano-Hummingbird; UMD SB, JB, BB – University of Maryland Small Bird, Big Bird, Jumbo Bird; AM – Brian’s Ornithopter; uB3 – NiCad powered Caltech Microbat

In hovering or steady forward flight, it is reasonable to assume that weight is proportional to lift

$$W \propto \frac{1}{2} c_L \rho V_t^2 A_{fl} \quad (26.95)$$

We assume that  $c_L$  (lift coefficient),  $\rho$  (density,) and  $g$  (gravitational acceleration) are constant [26.49], which is reasonable for flights on earth at low altitudes. Then, rearranging produces the following relationship between forward velocities,  $V_t$

$$V_{t,2} = V_{t,1} \sqrt{\frac{W_2 A_{fl,1}}{W_1 A_{fl,2}}} \quad (26.96)$$

We can then assume that the advance ratio  $J$  is constant for both vehicles, which is a reasonable approximation for ornithopters with similar wing kinematics, shape, and deformation. The advance ratio  $J$  is the ratio of maximum forward speed to wingtip speed

$$J = \frac{V_t}{4f\Phi R} \quad (26.97)$$

Since wingspan is twice the radius, and we can use the assumption that  $J$  is constant to obtain the following relationship for flapping frequencies

$$f_2 = \frac{V_{t,2}}{V_{t,1}} \frac{b_1}{b_2} \frac{\Phi_1}{\Phi_2} f_1 \quad (26.98)$$

Then, assuming that flapping amplitude,  $\Phi$  is constant between the two designs (reasonable for designs that follow the same parameters and keep the same gear-boxes) we can simplify the relationship for flapping frequencies

$$f_2 = \frac{V_{t,2}}{V_{t,1}} \frac{b_1}{b_2} f_1 \quad (26.99)$$

The required power to fly is proportional to the weight and flight speed

$$P \propto mgV_t = WV_t \quad (26.100)$$

Thus, we can calculate the power required of the new flapper relative to that of the old flapper

$$P_2 = P_1 \frac{V_{t,2}}{V_{t,1}} \frac{W_2}{W_1} \quad (26.101)$$

Using the power calculated above, the flight time can be estimated as

$$t = \frac{C_{LiPo} U_{LiPo}}{P} m \quad (26.102)$$

in which  $U_{\text{LiPo}} = 3.7 \text{ V}$  for a LiPo battery, and where, as in Fig. 26.35, the capacity can be approximated as

$$C_{\text{LiPo}} = m_{\text{batt}} k_{\text{batt}}. \quad (26.103)$$

From the scaling equations (particularly (26.101) and (26.102)), we can produce a set of graphs as in Fig. 26.36, allowing us to use the wingspan and flight time to design a scaled ornithopter. Beginning with the approximate wingspan and flight time desired, we use Fig. 26.36a to choose the appropriate battery mass. An increase in wingspan creates the option for heavier batteries and an increase in flight time as does an increase in battery mass. The wingspan and battery mass specify the required flapping frequency. This allows us to choose a motor and gear ratio. If this turns out to be impractical with available components, we can adjust parameters and iterate between the equations shown in Fig. 26.36. In general, for an ornithopter with equal mass, increasing the wingspan decreases the necessary flapping frequency. Alternatively, increasing the battery mass to improve flight time also requires increasing flapping frequency, electric power, and current to carry the extra payload. This explains why increasing battery mass beyond empty weight causes little increase in flight time, because the airframe needs to become much stronger at the cost of weight. A penalty in the flight time scaling equation needs to be implemented to correct for the increase in structural weight. The required flapping frequency and battery mass ratio

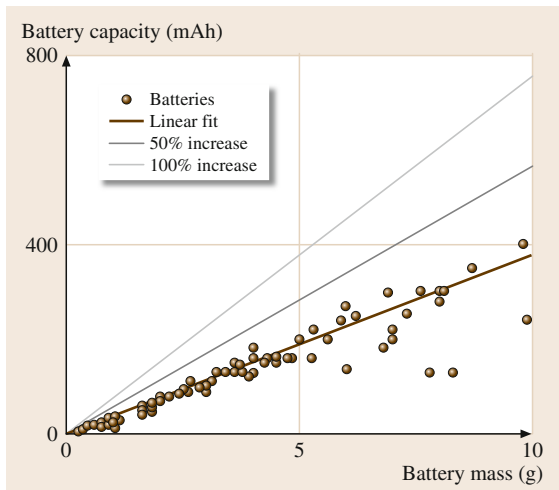


**Fig. 26.35** Battery capacity as a function of mass for many small lithium polymer (LiPo) batteries in the size range ( $< 10 \text{ g}$ ) which would be used for ornithopters with 10–50 cm wingspan. The graph shows the technology is linearly scalable. The approximate capacity density of small LiPo cells (3.7 V) is 37 mAh/g

specify the required power. Power increases significantly with wingspan. Additionally, power increases with added battery mass due to the increase in flapping frequency required to lift the larger mass. Finally, we can determine the current the battery needs to supply, which is proportional to the power assuming we use the same kind of battery and efficiency of motor. Iterating between these steps enables finding solutions that best meet the mission specifications. We note that many ornithopters could fly significantly longer by doubling their current battery mass (Fig. 26.36a) at the expense of control response (inertia) and airframe loading.

If flight time needs to increase for a wingspan-constrained ornithopter design, and battery mass and chemistry is already optimized, we should reduce air-

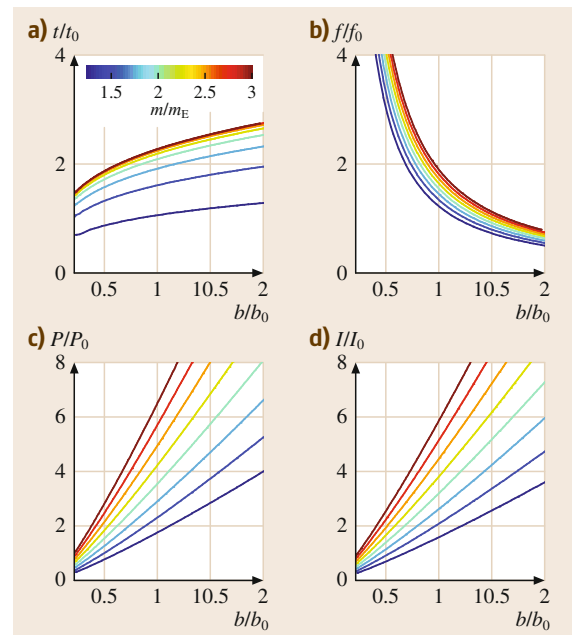


**Fig. 26.36a–d** These four figures show the effects of changing wingspan and adding battery mass to an ornithopter on the flight time, power consumption, current requirement, and flapping frequency requirement. The value of the empty mass,  $m_e$ , is determined using the fitted curve in Fig. 26.34a for each wingspan. The figures are then scaled from the initial reference (Delfly II) whose position is at (1, 1) in each figure. **(a)** Increasing the battery mass ratio increases the flight time up until the ratio becomes equal to 3. This ignores additional airframe mass needed to carry these batteries. **(b)** However, increasing the battery mass also increases the required flapping frequency. **(c, d)** Increasing the frequency also increases the necessary power ( $P$ ) and current ( $I$ ). Using these parameters, we can iterate back and forth between the plots until a feasible design is found

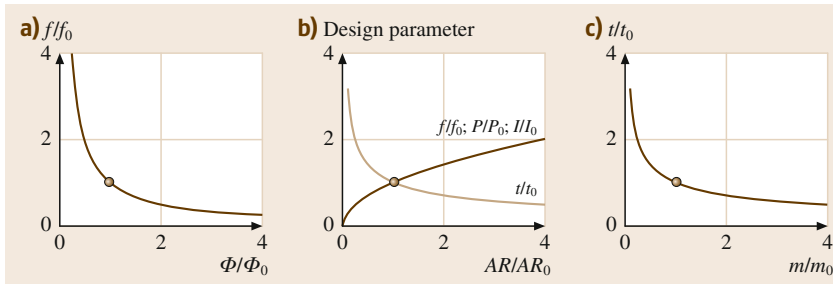


**Fig. 26.37a–c** Changing additional parameters can modify performance of a scaled vehicle. (a) Adjusting the flapping amplitude allows the user to change the required flapping frequency to use available motor/gearbox combinations. Generally, larger flapping angles result in increased lift coefficient and decreased drag (after [26.59]). Thus, increasing the amplitude to match it with the motor and gear train can decrease the required power to fly. (b) As the aspect ratio increases at a constant wingspan, the wing area decreases, and therefore the flight time decreases while the required flapping frequency (and hence the power and current) increases. (c) Flight time decreases with additional payload (weight)

frame mass (Fig. 26.37) and increase wing area [26.49]. Mass can be further decreased by airframe optimization using underutilized aerospace optimization strategies, and by critically reevaluating the payload. Wing area can be increased by decreasing aspect ratio and selecting a biplane instead of a monoplane configuration. Whereas such wing design changes reduce aerodynamic efficiency of the wing, they increase the overall vehicle energy efficiency, and therefore increase flight time. Ornithopters that fly long enough to complete missions are often controlled by low-weight underpowered actuators that sacrifice maneuverability.

To control the ornithopter's flight and to utilize its maneuverability, we need to generate enough control torques with lightweight actuators. Designs optimized for flight time, such as the Delfly, use control surfaces added to the tail in the style of a traditional rudder or elevator. More maneuverable designs use the flapping wings as control surfaces, by changing their angle of attack (Nano-Hummingbird [26.51]) or left versus right wing relative flapping motions (Robobee [26.52]). The two dominant off the shelf actuators are standard servos and magnetic actuators. Standard servos have small electric motors and potentiometers and move to specified positions; while magnetic actuators have a small magnet inside a small coil of wire and apply specified amounts of torque. Magnetic actuators are available at lower masses than servos, which proves critical in optimizing performance of smaller ornithopters. This shows that selecting appropriate actuators involves a tradeoff between flight duration and maneuverability. Ornithopters that are more maneuverable require more powerful and precise servo actuators. The required servo torque of a scaled ornithopter can be estimated assuming isometric scaling: Torque should be proportional to total weight times wingspan, because aerodynamic force is proportional to weight, and arm

length to wingspan. Knowing the required torque, we need to find a servo that can provide it. To reduce trial and error we have plotted current servo data to determine how torque correlates with mass to budget for its weight. The data in Fig. 26.38 shows that torque is proportional to mass squared for current servo technology,

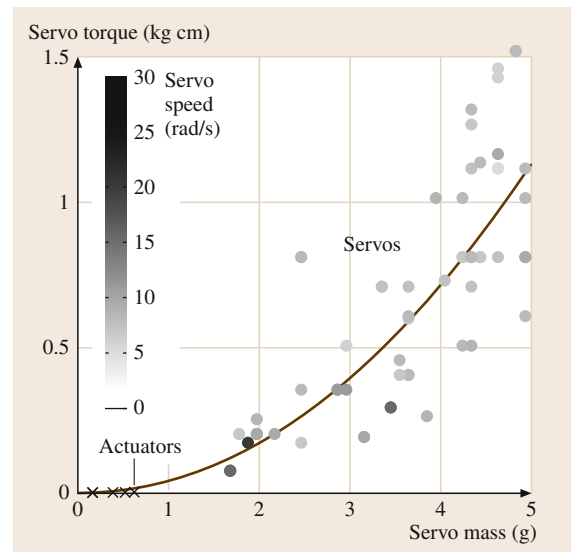


**Fig. 26.38** Servo (dots) and actuator (crosses) torques increases with mass. The intensity of dots represents the servo speed, with darker dots representing faster servos (the magnetic actuators do not have speeds shown, as they apply a force rather than specify a position). The servo speed does not correlate strongly with mass, as it is dependent on the motors, gears, and other internal hardware of the servo, as well as the supply voltage. There are magnetic actuators available in the range of 0.8–1.8 g, they are not included here due to lack of data available from manufacturers

while empty ornithopter mass scales with wingspan to the power of 1.5 (Fig. 26.34), so as wingspan increases the actuator mass can become proportionally smaller.

We have demonstrated current design strategies based off scaling successful designs that ensure ornithopters fly. These upgraded *rules of thumb* are powerful because current aerospace design analysis and

optimization techniques for ornithopters lack predictive power and are therefore less informative than estimates based on scaled flying designs. If current designers base their first iteration of new ornithopters on current state-of-the-art ornithopters, the field can progress at a faster pace through successful flight testing of new concepts that meet novel mission criteria.

## 26.7 System Integration and Realization

Enabling autonomous flights with UAS incorporates solving many challenges. This requires an interdisciplinary approach, bringing together expertise from many different fields. As shown in Fig. 26.39, knowledge in the field of aircraft design, as detailed in this chapter, is required, as well as in many fields of engineering and robotics.

### 26.7.1 Challenges for Autonomous UAS

Given the agility of UAS and their strict limitations on weight and power consumption, the choice of sensors, processors, and algorithms impose great technical and scientific challenges. Also, major differences exist between ground vehicles and UAS – sensors and algorithms that work well on ground vehicles cannot simply be applied on UAS due to inherent challenges.

#### Limited Payload and Power Supply

Weight and size restrictions require that lightweight sensors have to be used, usually at the cost of having noisier and less accurate data. These limitations also restrict the choice of onboard computers being used to

process information from the sensors. Thus, algorithms need to cope with such data to achieve robust estimates, while having limited computational power. As a reference, the take-off weight of a commonly used small multirotor UAS (e.g., shown in Fig. 26.40) is 1.5 kg, including 0.5 kg of payload, while the flight autonomy is approximately 15 min. For this class of UAS, approximately 100 mW are required per 1 g additional take-off weight for hovering – a fact that has to be considered even for mounting small additional payload. Detailed studies of take-off weight, payload, and flight time of such systems can be found in [26.60].

#### Degrees of Freedom

Compared to typical ground vehicles, there are two additional degrees of freedom (DOF) for the vehicle's attitude (pitch and roll angle) as well as one additional degree of freedom for the altitude, that need to be estimated and controlled. This requires state estimation, control, and planning to be performed in full 6-D space, and without simplifying assumptions.

#### Under-Actuated Systems

The types of UAS studied here are usually under-actuated, as there are less control inputs available than DOF. As a result, the attitude has to be changed for many maneuvers. This in return changes the field of view of onboard sensors interacting with the UAS' environment like cameras, or distance sensors.

#### Constant Motion and Inherent Instability

UAS cannot simply stop to acquire sensor readings, when state estimation is delayed or contains high uncertainty. While waiting for measurements or re-evaluation of uncertain state estimates, the vehicle continues moving and further falsifies these estimates.

### 26.7.2 Levels of Autonomy

We classify levels of autonomy and interaction with the pilot or operator into three categories: Manual flight, semiautonomous and autonomous. Industry and the re-

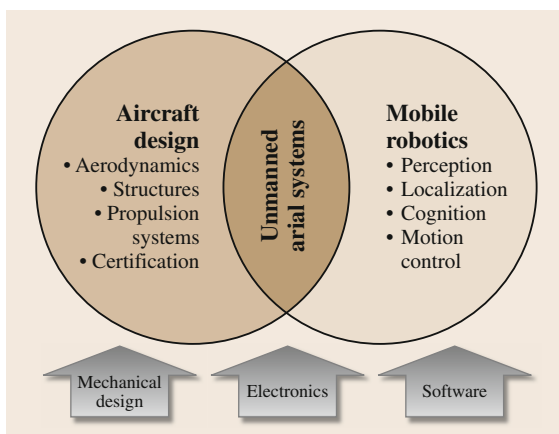


**Fig. 26.39** UAS design and research is interdisciplinary as challenges from both aircraft design and mobile robotics are combined

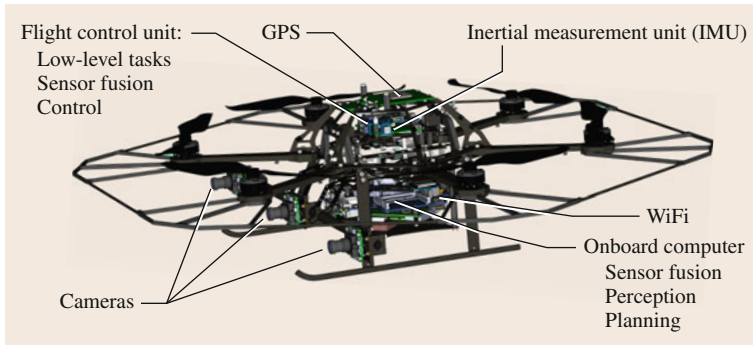


**Fig. 26.40** Multi-rotor UAS and its main components (after [26.60])

search community have made great progress toward semiautonomous flights, while there are still many open questions and research topics for truly autonomous operation.

### Manual Flight

We refer to this mode when operation of the UAS requires pilot skills. A remote-pilot has to handle attitude dynamics and throttle/thrust in a way such that the UAS remains in a stable state. That is, the pilot cannot leave the hands off the remote control. This also means that line-of-sight has to be maintained up to a distance where the pilot can observe the state of the UAS properly. Piloting may be aided by a stability augmentation system (SAS), like rate stabilization commonly used on fixed wing aircraft, or attitude control commonly used on multirotor UAS.

### Semiautonomous (Automatic)

This flight mode does not require piloting skills anymore, which is why we refer to a pilot rather than an operator. Onboard sensors and algorithms are in charge of stabilizing the UAS, such that the operator can leave the hands off the remote control and the UAS remains in a stable state, waiting for input such as waypoints or desired velocities. However, it is still the full responsibility of the operator to find feasible paths, safely navigate around obstacles and to interact with other air traffic. This requires line of sight to be maintained, however, first-person view could be thought of,

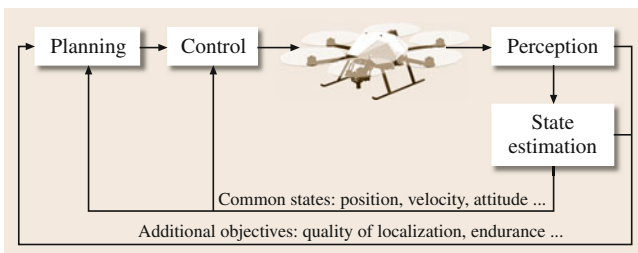


**Fig. 26.41** Components for an autonomous UAS

as long as legal requirements are fulfilled. Examples for such modes are off-the-shelf multirotor UAS [26.61] equipped with GPS sensors or small fixed-wing aircraft [26.62] used for surveying.

### Autonomous

Full autonomous mode relaxes the constraints from semiautonomous or automatic mode. Only mission goals are set, or high-level task allocation is handled by the operator, while the UAS navigates through the environment safely by itself. This includes global path planning, collision avoidance with both static and dynamic objects and replanning where necessary. The main idea is that the UAS can be *left alone* while performing the task at hand, and, in case, warns the operator ahead of time if intervention becomes necessary.

## 26.7.3 UAS Components

Autonomous UAS require numerous components from various fields, which need to be carefully designed in order to address the challenges detailed above. We highlight important design considerations of building blocks first, and show implementation aspects for real systems. Figure 26.40 shows the components for a commonly used multirotor UAS.

### Components for Autonomous Flights

The levels of autonomy defined in Sect. 26.7.2 require several components to be designed and to work with each other. These components are shown in Fig. 26.41 and are described in the following:

**Perception and State Estimation.** Perception for autonomous UAS mainly involves both localization of the UAS and sensing of its environment. For localization, commonly used satellite-based localization systems such as GPS (GLONASS or GALILEO in the future) may not be accurate enough, especially during tasks that involve operation in close proximity to (man-made) structure, and certainly not indoors. Di-



rect view to satellites is obstructed in these cases, compromising localization accuracy. Also, it may be considered whether sole reliance on these services is acceptable, as authorities may deteriorate the accuracy on purpose (*selected availability*). Thus, additional sensors such as cameras or laser-rangefinders should be used onboard UAS in combination with simultaneous localization and mapping (SLAM), or visual or laser odometry algorithms, yielding additional localization information [26.63–67].

Another important requirement to enable autonomous flights on the levels defined above, is sensing or reconstruction of the environment in order to navigate around obstacles, and for sense-and-avoid maneuvers with other air traffic. Obstacle sensing is especially important when navigating close to terrain at low altitude. Satellite-based navigation in combination with terrain maps may not be accurate enough, outdated, and cannot handle dynamic obstacles. Again, onboard sensors such as cameras, laser-rangefinders, or even radar, in combination with appropriate algorithms need to be used to overcome the limitations mentioned before [26.68, 69].

Having information from a multitude of sensors, from IMU over cameras to satellite-based, intelligent sensor fusion methods are required, taking all information into account and yielding a best estimate of the state of the UAS and its environment. As such, perception and state estimation are building blocks, providing essential information to the components described in the following.

**Control.** As UAS typically present highly dynamic uncertain flight behavior, appropriate and robust control techniques are required across all levels of autonomy. This ranges from SAS used for supporting the pilot during manual operation, to higher level control such as waypoint following, and more advanced techniques such as trajectory tracking, and may include handling of failure situations. Cascaded control structures are commonly used for this task [26.70]: inner- or low-level control loops stabilize attitude dynamics (these may be cascaded already), while outer- or high-level control loops stabilize translational dynamics (velocity or position). Employed control approaches range from simple P(I)D structures to more advanced techniques like model predictive control (MPC) [26.3]. During waypoint following, specified waypoints have to be reached and via-points have to be passed, while the velocity and attitude profile is left to the controller to optimize. For trajectory tracking in contrast, a tracking controller [26.71] has to follow specific profiles for position and attitude dynamics. These profiles are usually planned with approaches presented below,

and yield more smooth paths than simple waypoint following.

**Planning.** Planning in the context of UAS depicts the process of planning appropriate waypoints or dynamic trajectories for a UAS depending on the mission at hand. This involves the latter two levels of autonomy described in the previous section. Requirements range from (dynamic) obstacle avoidance, taking obstacles and the dynamics of the UAS into account, to more sophisticated complete mission plans [26.72]. While taking into account vehicle dynamics is a straightforward choice, additional constraints such as quality of state estimation along a path, or battery endurance may have to be considered as well. Furthermore, there may be additional objectives like area covered or, for instance, energy optimizations for solar airplanes in order to stay airborne 24 h or longer.

While analytic approaches [26.73] can be used for simple planning tasks, random sampling-based planners [26.74–76] dominate the literature in the area of path planning for UAS, due to their ability to cope with nonlinear vehicle dynamics and high-dimensional state spaces. Based on these planners, a number of successful approaches exist for UAS, even taking into account localization uncertainty [26.4, 77–79].

**Communication.** Communication can be thought of the *glue* between the components mentioned above. While components have to communicate onboard across multiple computation devices, there is also the need of communication with a ground station, or with the operator remote control device, via radio-links. Here, the requirements in terms of range, delay, and transmission rate (commonly referred to as *bandwidth*) can vary greatly and should be tailored to the application: computationally heavy tasks, being offloaded to a ground station require high-bandwidth connections, where either WiFi (IEEE 802.11n or IEEE draft 802.11ac) or ultra wide band (UWB) techniques can be applied. However, a reasonable maximum range is in the order of 100 m. More autonomy means also less dependence on radio-links and realtime constraints. Missions involving larger distances have to rely on longer range radio-links, even up to satellite links, but at the expense of bandwidth and delay or significant weight and power requirements. That radio-links should never be used inside any (real-time) critical control loops, goes without saying.

#### Integration Onboard UAS

The components identified above have different requirements in terms of real-time constraints and computational complexity. Instead of real time, it is more

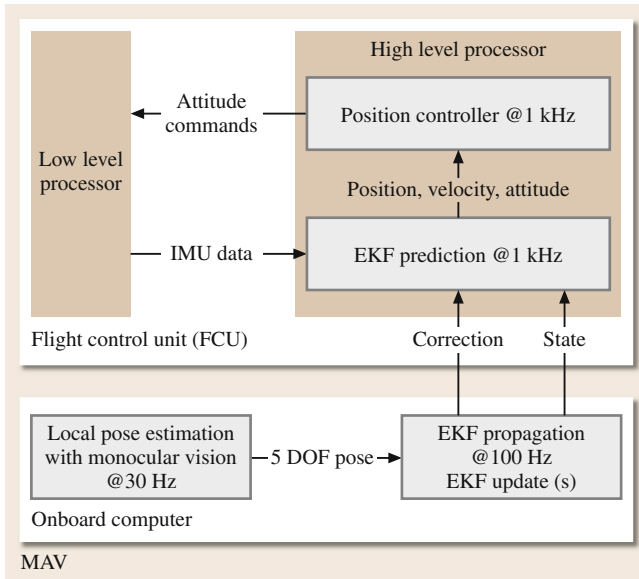


**Fig. 26.42** Example implementation of flight-relevant components onboard a multirotor UAS. All time-critical tasks such as control and the prediction part of an extended Kalman filter (EKF) are performed on real-time microcontroller hardware, while computationally more demanding, but less time-critical, tasks (visual localization, EKF update) are processed on the onboard computer using a standard operating system

appropriate to consider that a task has to be completed *in time*. As an example, vehicle *control* tasks have to be computed within a few milliseconds, but these tasks are

## 26.8 Applications of Aerial Robots

From an application perspective, one may distinguish between UAS that mostly operate as remote controlled or semiautonomous systems (typically referred to as drones) and intelligent systems, robots that present advanced levels of autonomy. Drones are essentially tele-operated aircraft or systems capable of tracking predefined trajectories while they further integrate onboard sensors to provide situational awareness. Most often such situational awareness is visual (using optics) but can also include meteorological and environmental tasks like hurricane-monitoring and chemical plume detection. As such, most drones fly high with a predetermined and structured flight plan and mission profile. Drones will continue to be valuable assets and as featured in daily media headlines world-wide, positively impact both civilian and military missions.

Nowadays, a constant trend is to develop aerial robots of advanced intelligence. Machine cognition,

computationally less complex. *Path planning* in contrast is fairly complex, but it is usually perfectly fine if a path is computed within seconds, since planning horizons span much longer time. *Perception* and parts of *state estimation* lie in-between and need computation times in the order of tens of milliseconds. This defines how, and on which computation devices these components should be implemented. An example for a multirotor UAS is shown in Fig. 26.42. The microcontrollers on the flight-control-unit (FCU) are closest to inertial sensors and actuators, but least powerful. Control loops and the prediction parts of the state estimator are implemented here, running at guaranteed rates on a real-time operating system, or even without. This relaxes real-time constraints on the onboard computer, which can compute demanding tasks such as visual localization and update steps for state estimation. Local planning tasks are computed here as well, while less critical parts can be offloaded to a ground station.

### Application Related Payload

While there is a set of sensors required to enable autonomous navigation, which are referred to as navigation sensors, additional sensors, or payload in general, need to be considered in the design phase. Not only in terms of payload, i.e., weight, but also such that the UAS is kept balanced. Furthermore, it has to be guaranteed that the additional payload does not interfere (electromagnetically) with components in the critical stabilization loop. Applications and their required sensors are detailed in the next section.

perception and vehicle control algorithms work in concert to perform applications that go beyond just situational awareness. Reaching new levels of autonomy, these robots are designed to handle unforeseen events, interact with their environment, and adapt to a broad range of scenarios. In essence, drones were in their vast majority *passive*, providing *eyes* on scene whereas modern aerial robots tend to become *active*, allowing their users to *engage* the scene, act *autonomously* and possibly *interact* with surroundings. Figure 26.43 presents indicative examples of current and emerging applications.

### 26.8.1 Demonstrated Applications of UAS

The Handbook's first edition listed eight categories of *possible* applications. Since then, all these applications have been realized, albeit with various levels of ma-

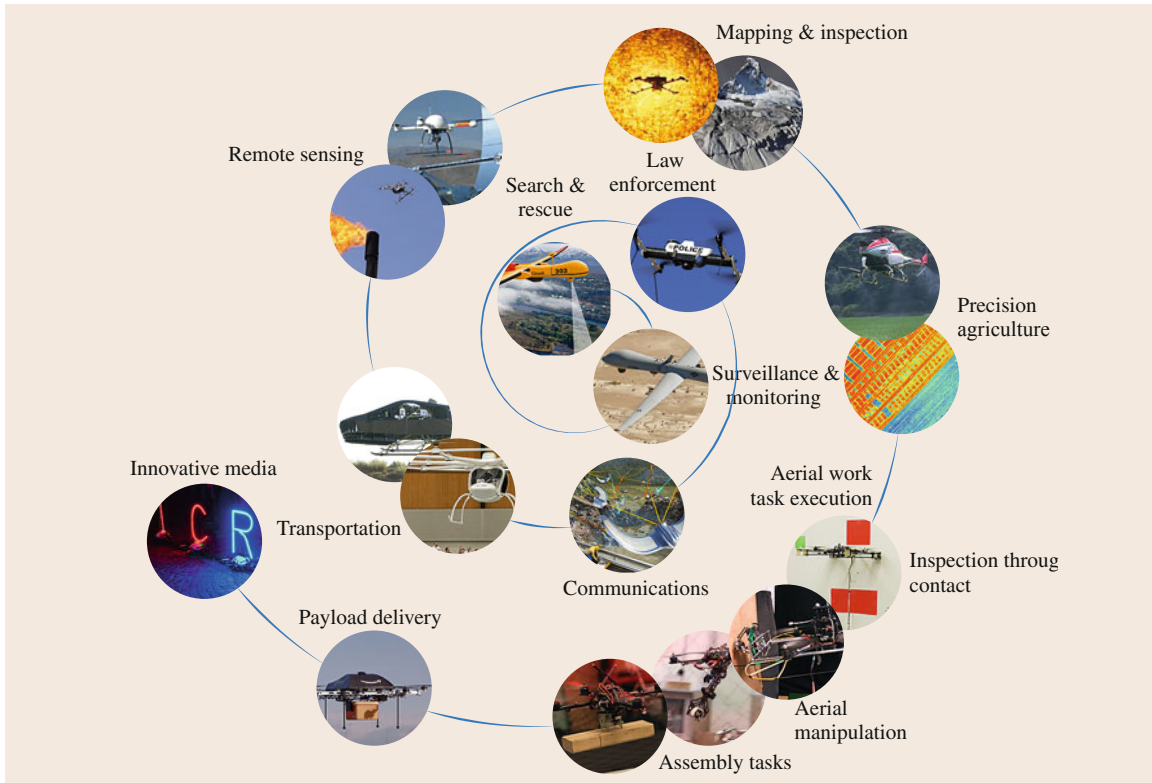


**Fig. 26.43** Indicative demonstrated and emerging applications of aerial robotics

turity. UAS (both drones and aerial robots) have been deployed in:

1. Remote sensing
2. Disaster response
3. Surveillance
4. Search and rescue
5. Image acquisition
6. Communications
7. Transportation
8. And payload delivery.

The first five categories broadly fall into the area of reconnaissance, surveillance, and target acquisition (RSTA). Drones have continued to successfully perform RSTA-based tasks like volcanic sampling, damage assessment, border patrol, and cinematography. In contrast, the latter three categories are being realized with advanced aerial robots. Equipped with computational intelligence aerial robots can flock. Aerial robots can also airlift, maneuver and interact in near-Earth environments like in-and-around buildings, forests, caves and tunnels. As such current trends in aerial robotics push the application envelope beyond RSTA. The eight categories are now revisited with context on the ex-

pected breakthroughs to come while the topic of visual inspection for industrial purposes is separately discussed:

- *Remote sensing*: Drones are already used for pipeline spotting, power line monitoring, volcanic sampling, mapping, meteorology, geology, agriculture and unexploded mine detection. Advanced aerial robots will be able to conduct pipeline risk assessment and repair, power line maintenance, real-time mapping, crop care and mine defusing.
- *Disaster response*: Drones are also used for chemical sensing, flood monitoring, and wildfire management. Advanced aerial robots will be able to conduct infrastructure repair, flood mitigation, and wildfire fighting.
- *Surveillance*: Drones are employed for law enforcement, traffic monitoring, coastal and maritime patrol, and border patrols. Advanced aerial robots will be able to accomplish tasks like crowd control, traffic redirection, and inspection of maritime and trucking containers.
- *Search and rescue*: The vision of using drones for search and rescue operations within low-density or hard-to-reach areas has already become a reality.

Advanced aerial robots will be able to go beyond casualty extraction by assessing care and delivering first-aid support.

- **Visual inspection:** For quite some time, drones are utilized to provide direct visual feeds to ground operators inspection industrial and civil structures. Future aerial robots will be able to act as a new high fidelity autonomous inspection tools that could also be capable of conducting maintenance work tasks.
- **Transportation:** Drones are already used for small- and large-cargo transport, and possibly passenger transport. Advanced aerial robots will be able to conduct in-flight refueling of other aircraft, pick-up and drop-off of cargo as well as loading and extraction of casualties.
- **Communications:** The use of drones as permanent or ad hoc communication relays for voice and data transmission, as well as broadcast units for television or radio is currently a reality. Advanced aerial robots will be able to conduct perch-and-stare to serve as *bug on the wall* listening devices, perch-and-stare to harvest energy from power lines, flocking to establish networks especially in areas with degraded communications.
- **Payload delivery:** Drones are already employed for firefighting or crop dusting. Advanced aerial robots will be able to accomplish dexterous manipulation of payloads like tools for repairing structures, delivering, and insertion of logistics as well as handling crops.
- **Image acquisition:** Cinematography or real-time entertainment is another relatively established use-case of drones. Advanced aerial robots will be able to conduct acting as *pixels* and operate in formation flight to serve as physical displays in the air.

### 26.8.2 Current Applications and Missions

Since the Handbook's first edition, media headlines continue to document UAS and their impact in all the aforementioned application categories. No longer are such applications notional but are rather considered as routine. The following provides recent state-of-the-art examples in each category to underscore this message.

Drone usage for RSTA-based military operations is routine. Tracking targets and, in growing instances, destroying them, is commonly performed. But also non-military missions in remote sensing, disaster response, and surveillance are becoming routine. Beyond image acquisition, drones are routinely used to gather meteorological data. NASA and NOAA regularly deploy drones for real-time monitoring of hurricanes. On-board sulfur dioxide sensors gather airborne samples from volcanic plumes. Drones are frequently deployed

after disasters: in Fukushima (2011) and Hurricane Sandy (2012) aerial images were gathered to assess building damage. Monitoring of maritime piracy and cartel drug-trafficking also underscore the usefulness of drones to persistently survey using high-definition cameras and night vision systems.

Currently, drones are deployed to open and/or restricted areas where airborne collision risk is reduced. The need for situational awareness will however continue to be fulfilled by UAS. The demand for more data will push the development of newer drones. As such, well-known and cutting-edge aerodynamic design principles will be applied so that UAS fly longer and farther and incorporate different flight modalities like vertical take-off and landing (VTOL). Sensor suites will also grow in sophistication to collect higher-resolution and/or multispectral data. Propulsion technologies will also be engineered to enable UAS to carry more sensors. The net effect is that as missions become more routine and frequent, the variations of drones and their performance will grow to keep up with expanding RSTA-based needs.

### 26.8.3 Aerial Robots: Emerging Categories

The road ahead is full of challenging emerging applications that will benefit from the utilization of aerial robotic technologies. This is especially the case when one considers near-Earth environments like in-and-around buildings, through forests and down tunnels and caves. Beyond RSTA, such environments provide opportunities for aerial robots to dexterously interact with objects. Today's drones release retardants over wildfires but tomorrow's aerial robots would attach hoses and breach walls for firefighting. Interaction demands advances in areas like aircraft design (flight modalities, payload capability), algorithms (perception, control, motion planning, and grasping) and manipulators (arms and end-effectors). The latter two areas overlap with the greater domain of robotics research. As deeper understanding and realizations develop, the application space, demand and impact of aerial robots will grow even greater. In the following, a brief overview of exciting emerging applications will be listed.

#### Assembly Work Task Execution

One notional concept employs aerial robots to assembly physical structures. Such assembly pushes the boundaries of the categories of transportation and payload delivery. Labs like those of University of Pennsylvania [26.80], Switzerland (ETH Zurich [26.81]) have used gripper-mounted quadrotors to illustrate proof-of-concept. Demonstrations include the pickup and drop-off of workpieces to defined locations. These

workpieces self-connect using magnets or premachined joints but illustrate capabilities to coordinate multiple aircraft, mitigate disturbances like ground effect, sense and map, and execute agile maneuvers. Groups at Drexel, Twente, Seville, and Yale are equipping rotorcraft robots with manipulators to illustrate more dexterous tasks like inserting, screwing, and removing workpieces. Assembly and in general physical work-task execution will find applications in categories like disaster response (repairing structures) and remote sensing (inserting sensors).

### Inspection Through Contact

Inspecting containers at docks, ships, and border crossings is a daunting task. Sensor technology is advancing to look inside such containers. However, dexterous aerial robots that can open hatches and trunks could also yield many applications. Inspection as an emerging category can employ aerial robots to physically interact with structures. Aerial robots can physically probe bridges, pipelines, and power lines to repair and replace parts. Interactive inspection could emerge to applications like crop handling and mine defusing. Labs like those of ETH Zurich [26.82] and the University of Bologna [26.83] have presented relevant results in the topic.

### Innovative Media

Both the number of vendors and affordability of rotorcraft robots have increased since the Handbook's first edition. In mid-2000, it was not surprising to see a commercial quadrotor costing 40 000 USD. Today, there are dozens of companies providing robotic rotorcraft ranging in price (hundreds to under 10 000 USD), size (from pucks to bike wheels) and configurations (mono, co-axial, and multirotor). Such range will likely yield innovative and entrepreneurial applications.

The Firefly project at the MIT SENSEable Lab perhaps best illustrates the notion of coordinating multiple aerial robots to display images. Each aerial robot acts as flying *pixel* and maneuver into position to form 2 or 3-D images. Beyond visual and dynamic art, such capabilities could yield airborne displays for tasks like crowd control, traffic redirection and SOS signals. Airborne displays could also expand creative expression to enhance concerts, advertise at stadiums, and inform audiences.

### Autonomous Structural Inspection and 3-D Reconstruction

From the perspective of the role of aerial robotics in accelerating growth, mapping of areas, structural inspection of buildings and infrastructure as well as recognition of objects or areas of interest is among the most important application fields. Aerial robots have

achieved great milestones in such scenarios. Among others, recently researchers managed to extract a high-fidelity 3-D model of the Swiss mountain top Matterhorn utilizing a small FW-UAS and sophisticated robotic vision techniques [26.84], other efforts led to the inspection of a real power plant boiler using a multirotor vehicle and tightly integrated visual-inertial algorithms [26.85], while in terms of industrial adoption aerial robots have provenly minimized the inspection times of power infrastructure [26.86] and are often used in combination with geographic information system (GIS) data [26.84]. It is worth noting that some of the largest asset owners and service providers in the field of civil infrastructure and civil engineering works have shown interest and participate in large consortia that aim to make such aerial robotic technologies an integral and game-changing factor of how things are done (see e.g., Petrobot Project [26.87], ARCAS: Aerial Robotics Cooperative Assembly System [26.88], EuroC: European Robotics Challenges [26.89], ARGOS Challenge [26.90].).

### Precision Agriculture

Precision agriculture is considered to be among the fields where the use of aerial robots may become a key factor boosting growth and improving the production quality. The Japanese farming sector has historically been in a position to lead the relevant research efforts with successful designs like the Yamaha RMAX being extensively used for monitoring as well as spraying operations [26.5]. Already in December 2002, 1687 aerial robots were used in Japan to conduct precision agriculture operations. However, current research contributions and pioneering technology early adopters have opened an even more promising channel for the widest possible utilization of aerial robotic technologies for the benefit of agriculture production. Mainly through the use of miniaturized aerial robotics at farms of smaller scale and via the integration of advanced multispectral perception sensors (i.e., NDVI) [26.91], accurate mapping and analysis regarding the quality of the field, the level of plant growth and existence of diseases becomes possible. Such technologies are expected to become a critical tool to optimize and enhance agricultural services. Furthermore, manipulators-equipped aerial robots will be able to autonomously physically act based on their perception of the field and minimize the time and effort required for several agriculture services and tasks.

### 26.8.4 Open Issues

Emerging categories underscore both the distinction between more traditional drones and emerging aerial



robotic technologies as well as how much further the state-of-the-art has to be pushed. Clearly, today's UAS have limited payloads but adding manipulators goes beyond lift issues. When interacting with objects, aerial robots must handle reaction forces and torques. Understanding such reactions remains an open issue. However, both space and underwater roboticists have looked at dexterous manipulators for tasks like satellite repair and turning valves on ocean-based oil rigs. As research clarifies this issue and as lift capacities increase, dexterous aerial robots will be realized.

Airspace access is an often cited issue that may limit aerial robot development and vast utilization. A US congressional bill was passed in 2012 that sets requirements for UAS to fly in the national airspace by 2015. This has also sparked competition among a dozen or

so states to establish UAS flight testing sites. In Europe, similar events have happened and there are UAS test sites in places like Finland (Kemijarvi), Sweden (NEAT), and Wales (Parc Aberporth).












Lastly, somewhat ironic is that today's unmanned drones require a crew of highly skilled operators. In the case of some Predator missions, crew sizes can be up to a dozen people. Also ironic is that human error is the most cited cause for drone accidents. As the number of UAS in the national airspace increases, the need for even more operators will also grow. This has the potential to raise the risk of UAS-related accidents. The issues of effective UAV pilot training, certifying operators, handling emergency landings, and sharing airports with manned aircraft will also emerge as pressing ones.



## 26.9 Conclusions and Further Reading

Design of aerial robots requires background knowledge in a multitude of subjects, from aerodynamics to dynamics, control, and system integration: we have overviewed the relevant basics along with analytical tools and guidelines to go through the stages of designing, modeling, and setting up operation of various types of unmanned aerial systems (UAS). An emphasis was given on custom tailoring a system to a specific application, in order to

optimally meet related requirements in terms of endurance, range, agility, size, complexity, as well as from a system integration point of view. The compilation at hand shall serve as a starting point, further motivating the reader to study the various fields with their related literature, ranging from aircraft and system design to the classical autonomous robotics challenges involving perception, cognition and motion control.

### Video-References

-  VIDEO 493 Delfly II in hover  
available from <http://handbookofrobotics.org/view-chapter/26/videodetails/493>
-  VIDEO 602 AtlantikSolar field-trials  
available from <http://handbookofrobotics.org/view-chapter/26/videodetails/602>
-  VIDEO 603 senseSoar UAV Avionics testing  
available from <http://handbookofrobotics.org/view-chapter/26/videodetails/603>
-  VIDEO 604 Structural inspection path planning via iterative viewpoint resampling with application to aerial robotics  
available from <http://handbookofrobotics.org/view-chapter/26/videodetails/604>
-  VIDEO 688 sFly: Visual-inertial SLAM for a small helicopter in large outdoor environments  
available from <http://handbookofrobotics.org/view-chapter/26/videodetails/688>
-  VIDEO 689 UAV stabilization, mapping & obstacle avoidance using VI-sensor  
available from <http://handbookofrobotics.org/view-chapter/26/videodetails/689>
-  VIDEO 690 Project Skye – autonomous blimp  
available from <http://handbookofrobotics.org/view-chapter/26/videodetails/690>
-  VIDEO 693 Flight stability in aerial redundant manipulators  
available from <http://handbookofrobotics.org/view-chapter/26/videodetails/693>
-  VIDEO 694 The astounding athletic power of quadcopters  
available from <http://handbookofrobotics.org/view-chapter/26/videodetails/694>
-  VIDEO 695 Robots that fly ... and cooperate  
available from <http://handbookofrobotics.org/view-chapter/26/videodetails/695>
-  VIDEO 696 A robot that flies like a bird  
available from <http://handbookofrobotics.org/view-chapter/26/videodetails/696>

-  VIDEO 697 Robotic insects make first controlled flight available from <http://handbookofrobotics.org/view-chapter/26/videodetails/697>
-  VIDEO 719 Towards valve turning using a dual-arm aerial manipulator available from <http://handbookofrobotics.org/view-chapter/26/videodetails/719>

## References

- 26.1 S. Leutenegger, M. Chli, R.Y. Siegwart: Brisk: Binary robust invariant scalable keypoints, Proc. IEEE Int. Conf. Comput. Vis. (ICCV) (2011) pp. 2548–2555
- 26.2 D. Scaramuzza, M.C. Achtelik, L. Doitsidis, F. Fraundorfer, E.B. Kosmatopoulos, A. Martinelli, M.W. Achtelik, M. Chli, S.A. Chatzichristofis, L. Kneip, G.H. Lee, S. Lynen, L. Meier, M. Pollefeys, A. Renzaglia, R. Siegwart, J.C. Stumpf, P. Tanskanen, C. Troiani, S. Weiss: Vision-controlled micro flying robots: From system design to autonomous navigation and mapping in GPS-denied environments, IEEE Robotics Autom. Mag. **2014**(9), 1–10 (2014)
- 26.3 K. Alexis, G. Nikolakopoulos, A. Tzes: Model predictive quadrotor control: Attitude, altitude and position experimental studies, IET Control Theory Appl. **6**(12), 1812–1827 (2012)
- 26.4 M.W. Achtelik, S. Lynen, S. Weiss, M. Chli, R. Siegwart: Motion and uncertainty aware path planning for micro aerial vehicles, J. Field Robotics **31**(4), 676–698 (2014)
- 26.5 K. Nonami: *Autonomous Flying Robots: Unmanned Aerial Vehicles and Micro Aerial Vehicles* (Springer, Berlin, Heidelberg 2010)
- 26.6 H. Tenenkes: *The Simple Science of Flight: From Insects to Jumbo Jets* (MIT, Cambridge 2009)
- 26.7 W.J. Pisano, D.A. Lawrence: Control limitations of small unmanned aerial vehicles in turbulent environments, Proc. AIAA Guid. Navig. Control Conf. (2009)
- 26.8 B. Mettler, C. Dever, E. Feron: Scaling effects and dynamic characteristics of miniature rotorcraft, J. Guid. Control Dyn. **27**(3), 466–478 (2004)
- 26.9 ICAO: *Manual of the ICAO Standard Atmosphere: Extended to 80 Kilometres (262 500 feet)* (Int. Civil Aviation Organization (ICAO), Montréal 1993)
- 26.10 M. Hepparle: JavaFoil – Analysis of java airfoils, <http://www.mh-aerotoools.de/airfoils/javafoil.htm> (2007)
- 26.11 M. Drela: XFoil – Subsonic airfoil development system, <http://www.web.mit.edu/drela/Public/web/xfoil> (2000)
- 26.12 Techwinder: xLfr5, <http://www.xlfr5.com> (2000)
- 26.13 B.W. McCormick: *Aerodynamics, Aeronautics, and Flight Mechanics* (Wiley, New York 1979)
- 26.14 G.J. Leishman: *Principles of Helicopter Aerodynamics* (Cambridge Univ. Press, Cambridge 2006)
- 26.15 G.D. Padfield: *Helicopter Flight Dynamics* (Blackwell, New York 2007)
- 26.16 L. Zaccarian: *Dc Motors: Dynamic Model and Control Techniques* (Lecture Notes Univ. Rome, Rome 2012)
- 26.17 M. Drela: AVL (Software for aerodynamic and flight-dynamic analysis), <http://web.mit.edu/drela/Public/web/avl> (2004)
- 26.18 B. Etkin: *Dynamics of Atmospheric Flight* (Wiley, New York 1972)
- 26.19 G.J.J. Ducard: *Fault-Tolerant Flight Control and Guidance Systems: Practical Methods for Small Unmanned Aerial Vehicles*, Advanced in Industrial Control (Springer, Berlin, Heidelberg 2009)
- 26.20 M.C.Y. Niu: *Airframe Structural Design* (Conmilit, Hong Kong 1988)
- 26.21 R. Randolph: *R/C Airplane Building Techniques*, R/C Encyclopedia (Air Age, Wilton 1991)
- 26.22 D.P. Raymer: *Aircraft Design: A Conceptual Approach* (AIAA, Washington 1989)
- 26.23 A. Noth: Design of Solar Powered Airplanes for Continuous Flight, Ph.D. Thesis (Ecole Polytechnique Fédérale de Lausanne, Lausanne 2008)
- 26.24 R.W. Beard, T.W. McLain: *Small Unmanned Aircraft: Theory and Practice* (Princeton Univ. Press, Princeton 2012)
- 26.25 A.A. Lambregts: *Vertical flight path and speed control autopilot design using total energy principles*, AIAA Paper (AIAA, Washington 1983)
- 26.26 S. Park, J. Deyst, J.P. How: A new nonlinear guidance logic for trajectory tracking, Proc. AIAA Guid. Navig. Control Conf. (2004) pp. 16–19
- 26.27 S. Bouabdallah, C. Bernes, S. Grzonka, C. Gimkiewicz, A. Brenzikofer, R. Hahn, D. Schafroth, G. Grisett, W. Burgard, R. Siegwart: Towards palm-size autonomous helicopters, Proc. Int. Conf. Exhib. Unmanned Aer. Veh. (2010)
- 26.28 P.I.E. Pounds, D.R. Bersak, A.M. Dollar: Grasping from the air: Hovering capture and load stability, Proc. IEEE Conf. Robotics Autom. (ICRA) (2011)
- 26.29 D. Gurdan, J. Stumpf, M. Achtelik, K.-M. Doth, G. Hirzinger, D. Rus: Energy-efficient autonomous four-rotor flying robot controlled at 1 khz, Proc. IEEE Int. Conf. Robotics Auton. Syst. (2007)
- 26.30 G.M. Hoffmann, H. Huang, S.L. Waslander, C.J. Tomlin: Quadrotor helicopter flight dynamics and control: Theory and experiment, Proc. AIAA Guid. Navig. Control Conf. (2007)
- 26.31 A. Ko, O.J. Ohnaian, P. Gelhausen: Ducted fan uav modeling and simulation in preliminary design, Proc. AIAA Model. Simul. Technol. Conf. Exhibit. (2007)
- 26.32 R. Naldi, F. Forte, L. Marconi: A class of modular aerial robots, Proc. 50th IEEE Conf. Decis. Control Eur. Control Conf. (2011)
- 26.33 E.R. Ulrich, J.S. Humbert, D.J. Pines: Pitch and heave control of robotic samara micro air vehicles, J. Aircr. **47**, 1290–1299 (2010)

- 26.34 C.Y. Yun, I. Park, H.Y. Lee, J.S. Jung, I.S. Hwang, S.J. Kim: A new vtol uav cyclocopter with cycloidal blades system, Proc. 60th AHS Annu. Forum Amer. Helicopter Soc. (2004)
- 26.35 R.W. Prouty: *Helicopter Performance, Stability and Control* (Krieger, New York 2005)
- 26.36 M.B. Tischler, R.K. Remple: *Aircraft and Rotorcraft System Identification: Engineering Methods with Flight-Test Examples* (AIAA, Washington 2006)
- 26.37 B. Mettler: *Identification, Modeling and Characteristics of Miniature Rotorcraft* (Kluwer, Boston 2002)
- 26.38 A.R.S. Bramwell, G. Done, D. Balmford: *Bramwell's Helicopter Dynamics* (Butterworth-Heinemann, London 2001)
- 26.39 R.T.N. Chen: *Effects of primary rotor parameters on flapping dynamics*, Tech. Rep. (National Aeronautics and Space Administration, Washington 1980)
- 26.40 R.T.N. Chen: *A survey of nonuniform inflow models of rotorcraft flight dynamics and control applications*, Tech. Rep. (National Aeronautics and Space Administration, Washington 1989)
- 26.41 R. Cunha: *Advanced Motion Control for Autonomous Air Vehicles*, Ph.D. Thesis (Instituto Superior Tecnico, Universidade Tecnica de Lisbon, Lisbon 2007)
- 26.42 T.N. Pornsin-Sirirak, S.W. Lee, H. Nassef, J. Grasmeyer, Y.C. Tai, C.M. Ho, M. Keennon: MEMs wing technology for a battery powered ornithopter, Proc. 13th IEEE Annu. Int. Conf. MEMS (2000) pp. 799–804
- 26.43 T.N. Pornsin-Sirirak, Y.C. Tai, C.M. Ho, M. Keennon: Microbat: A palm-sized electrically powered ornithopter, Proc. NASA/SPL Workshop Biomorph Robotics (2001) pp. 14–17
- 26.44 S.P. Sane: The aerodynamics of insect flight, J. Exp. Biol. **206**(23), 4191–4208 (2003)
- 26.45 M.H. Dickinson, F.O. Lehmann, S.P. Sane: Wing rotation and the aerodynamic basis of insect flight, Science **284**(5422), 1954–1960 (1999)
- 26.46 J. Young, S.M. Walker, R.J. Bomphrey, G.K. Taylor, A.L.R. Thomas: Details of insect wing design and deformation enhance aerodynamic function and flight efficiency, Science **325**(5947), 1549–1552 (2009)
- 26.47 L. Zhao, Q. Huang, X. Deng, S.P. Sane: Aerodynamic effects of flexibility in flapping wings, J. R. Soc. Interface **7**(44), 485–497 (2010)
- 26.48 F.O. Lehmann, S.P. Sane, M. Dickinson: The aerodynamic effects of wing-wing interaction in flapping insect wings, J. Exp. Biol. **208**(16), 3075–3092 (2005)
- 26.49 D. Lentink, S.R. Jongerius, N.L. Bradshaw: *Flying Insects and Robots* (Springer, Berlin, Heidelberg 2009)
- 26.50 G.C.H.E. de Croon, M.A. Groen, C. De Wagter, B. Remes, R. Ruijsink, B.W. van Oudheusden: Design, aerodynamics, and autonomy of the DelFly, Bioinspiration Biomim. **7**(2), 025003 (2012)
- 26.51 M. Keennon, K. Klingebiel, H. Won, A. Andriukov: Tailless flapping wing propulsion and control development for the nano hummingbird micro air vehicle, Proc. Am. Helicopter Soc. Futur. Vert. Lift Aircr. Des. Conf. (2012)
- 26.52 K.Y. Ma, P. Chirarattananon, S.B. Fuller, R.J. Wood: Controlled flight of a biologically inspired, insect-scale robot, Science **340**(6132), 603–607 (2013)
- 26.53 D. Lentink, M.H. Dickinson: Rotational accelerations stabilize leading edge vortices on revolving fly wings, J. Exp. Biol. **212**(16), 2705–2719 (2009)
- 26.54 W. Shyy, H. Aono, C.-K. Kang, H. Liu: *An Introduction to Flapping Wing Aerodynamics* (Cambridge Univ. Press, Cambridge 2013)
- 26.55 C.P. Ellington, C. van den Berg, A.P. Willmott, A.L.R. Thomas: Leading-edge vortices in insect flight, Nature **384**, 626–630 (1996)
- 26.56 D.R. Warrick, B.W. Tobalske, D. Powers: Lift production in the hovering hummingbird, Proc. R. Soc. Biol. Sci. (2009) pp. 3747–3752
- 26.57 F.T. Muijres, L.C. Johansson, A. Hedenstrom: Leading edge vortex in a slow-flying passerine, Biol. Lett. **8**(4), 554–557 (2012)
- 26.58 J. Koo, T. Oka: *Experimental Study on the Ground Effect of a Model Helicopter Rotor in Hovering*, Tech. Rep. (NASA, Washington 1966)
- 26.59 S.P. Sane, M.H. Dickinson: The control of flight force by a applying wing: Lift and drag production, J. Exp. Biol. **204**(15), 2607–2626 (2001)
- 26.60 M.C. Achteelik, K.-M. Doth, D. Gurdan, J. Stumpf: Design of a multi rotor MAV with regard to efficiency, dynamics and redundancy, Proc. AIAA Guid. Navig. Control Conf. (2012)
- 26.61 Ascending Technologies Ltd.: <http://www.asctec.de> (2015)
- 26.62 Sensefly (Parrot Company): <http://www.sensefly.com> (2000)
- 26.63 M.W. Achteelik: *Advanced Closed Loop Visual Navigation for Micro Aerial Vehicles*, Ph.D. Thesis (ETH Zurich, Zurich 2014)
- 26.64 A. Bachrach, S. Prentice, R. He, N. Roy: RANGE – Robust autonomous navigation in GPS-denied environments, J. Field Robotics **28**, 644–666 (2011)
- 26.65 S. Leutenegger, P. Furgale, V. Rabaud, M. Chli, K. Konolige, R. Siegwart: Keyframe-based visual-inertial slam using nonlinear optimization, Proc. Robotics Sci. Syst. (RSS) (2013)
- 26.66 S. Weiss: *Vision Based Navigation for Micro Helicopters*, Ph.D. Thesis (ETH Zurich, Zurich 2012)
- 26.67 A.I. Mourikis, S.I. Roumeliotis, J.W. Burdick: SC-KF mobile robot localization: A stochastic cloning kalman filter for processing relative-state measurements, IEEE Trans. Robotics **23**(4), 717–730 (2007)
- 26.68 A. Bachrach, S. Prentice, R. He, P. Henry, A.S. Huang, M. Krainin, D. Maturana, D. Fox, N. Roy: Estimation, planning, and mapping for autonomous flight using an RGB-D camera in GPS-denied environments, Int. J. Robotics Res. **31**, 1320–1343 (2012)
- 26.69 T. Tomic, K. Schmid, P. Lutz, A. Domel, M. Kassecker, E. Mair, I. Grix, F. Ruess, M. Suppa, D. Burschka: Toward a fully autonomous UAV: Research platform for indoor and outdoor urban search and rescue, IEEE Robotics Autom. Mag. **19**(3), 46–56 (2012)
- 26.70 S. Bouabdallah: *Design and Control of Quadrotors with Application to Autonomous Flying*, Ph.D. Thesis (STI School of Engineering, EPFL, Lausann 2007)

- 26.71 T. Lee, M. Leoky, N.H. McClamroch: Geometric tracking control of a quadrotor UAV on  $SE(3)$ , Proc. 49th IEEE Conf. Dec. Control (CDC) (2010) pp. 5420–5425
- 26.72 P. Doherty, J. Kvarnström, F. Heintz: A temporal logic-based planning and execution monitoring framework for unmanned aircraft systems, *Auton. Agents Multi-Agent Syst.* **19**(3), 332–377 (2009)
- 26.73 P.E. Hart, N.J. Nilsson, B. Raphael: A formal basis for the heuristic determination of minimum cost paths, *Trans. Syst. Sci. Cybern.* **4**(2), 100–107 (1968)
- 26.74 S. Karaman, E. Frazzoli: Incremental sampling-based algorithms for optimal motion planning, Proc. Robotics Sci. Syst. (RSS), Zaragoza (2010)
- 26.75 L.E. Kavraki, P. Švestka, J.-C. Latombe, M.H. Overmars: Probabilistic roadmaps for path planning in high-dimensional configuration spaces, *IEEE Trans. Robotics Autom.* **12**(4), 566–580 (1996)
- 26.76 S.M. LaValle, J.J. Kuffner: Randomized kinodynamic planning, *Int. J. Robotics Res.* **20**(5), 378–400 (2001)
- 26.77 A. Bry, N. Roy: Rapidly-exploring random belief trees for motion planning under uncertainty, Proc. IEEE Int. Conf. Robotics Autom. (ICRA) (2011) pp. 723–730
- 26.78 H. Cover, S. Choudhury, S. Scherer, S. Singh: Sparse tangential network (SPARTAN): Motion planning for micro aerial vehicles, *IEEE Proc. Int. Conf. Robotics Autom. (ICRA)* (2013)
- 26.79 R. He, S. Prentice, N. Roy: Planning in information space for a quadrotor helicopter in a gps-denied environments, *IEEE Proc. Int. Conf. Robotics Autom. (ICRA)* (2008) pp. 1814–1820
- 26.80 Q. Lindsey, D. Mellinger, V. Kumar: Construction with quadrotor teams, *Auton. Robots* **33**(3), 323–336 (2012)
- 26.81 J. Willmann, F. Augugliaro, T. Cadalbert, R. D’Andrea, F. Gramazio, M. Kohler: Aerial robotic construction towards a new field of architectural research, *Int. J. Archt. Comput.* **10**(3), 439–460 (2012)
- 26.82 G. Darivianakis, K. Alexis, M. Burri, R. Siegwart: Hybrid predictive control for aerial robotic physical interaction towards inspection operations, Proc. IEEE Int. Conf. Robotics Autom. (ICRA) (2014)
- 26.83 L. Marconi, R. Naldi, L. Gentili: Modelling and control of a flying robot interacting with the environment, *Automatica* **47**(12), 2571–2583 (2011)
- 26.84 Z. Lin: UAV for mapping – low altitude photogrammetric survey, Proc. 21st ISPRS Congr. Techn. Commis. I, Beijing (2008) pp. 1183–1186
- 26.85 J. Nikolic, M. Burri, J. Rehder, S. Leutenegger, C. Huerzeler, R. Siegwart: A UAV system for inspection of industrial facilities, Proc. IEEE Aerosp. Conf. (2013) pp. 1–8
- 26.86 Cyberhawk: Aerial Inspection and Suervying Specialists, <http://www.thecyberhawk.com> (2015)
- 26.87 Petrobot Project: <http://www.petrobotproject.eu/>
- 26.88 ARCAS: Aerial Robotics Cooperative Assembly System, <http://www.arcas-project.eu/>
- 26.89 EuRoC: European Robotics Challenges, <http://www.euroc-project.eu/>
- 26.90 ARGOS Challenge: <http://www.argos-challenge.com/>
- 26.91 E.R. Hunt Jr., W.D. Hively, S.J. Fujikawa, D.S. Linden, C.S.T. Daughtry, G.W. McCarty: Acquisition of nir-green-blue digital photographs from unmanned aircraft for crop monitoring, *Remote Sens.* **2**, 290–305 (2010)